

CARNEGIE MELLON UNIVERSITY

Multi-scale Modeling and Optimization
of Polymer Electrolyte Fuel Cells

A DISSERTATION

SUBMITTED TO THE GRADUATE SCHOOL

IN PARTIAL FULFILLMENT

OF THE REQUIREMENTS

for the degree of

DOCTOR OF PHILOSOPHY

in

CHEMICAL ENGINEERING

by

PARAG JAIN

Pittsburgh, Pennsylvania

September 8, 2009

Abstract

For achieving stringent design & performance objectives in energy systems, it becomes necessary to develop holistic integrated models as well as, ascertain the level of details required within each sub-system, for accurate physical description and system optimization. This requires multi-scale modeling, which involves description of atomistic, molecular, mesoscopic, continuum, device, and plant levels as well as transmitting information sequentially at each level to produce synergistic knowledge-bases. This dissertation focuses on constructing a generalized framework for integration, as well as examination of sensitivity of sub-system models to fulfill overall design & performance objectives by selecting hydrogen polymer electrolyte fuel cell (PEFC) as a benchmark case study. The hydrogen PEFC is an alternative power producing device for stationary and automotive applications, with advantages of high efficiency, operation on renewable fuels with near-zero green house gas emissions.

We begin by developing an integrated modeling and optimization framework that includes detailed computational fluid dynamics based models. As an illustration, a multi-dimensional, multi-physics PEFC model is constructed

that accounts for major transport processes in the gas channel and the membrane electrode assembly, with a phenomenological description within the catalyst layer (CL) sub-component. The resulting system of highly nonlinear partial differential-algebraic equations is fully discretized using a finite volume method, and the resulting large-scale nonlinear program is linked to a state-of-the-art interior point optimization algorithm. The framework is used for solving challenging parameter estimation problems resulting from incorporation of multiple experimental data points. Also, parametric studies are performed on detailed water transport mechanisms and distribution characteristics, and on overall system performance.

We then replace the phenomenological CL description with a state-of-the-art continuum description which is closer to realistic scenario and provides control over actual physical parameters. For achieving this, we adopt the agglomerate CL model, and recast it into a compact form for optimization of PEFC cathodes. This reformulation captures the transport processes within gas diffusion layer (GDL) and CL, and transport/reaction processes within an individual agglomerate particle. From the platinum (Pt) minimizations we obtain relationships between optimal Pt mass and current density at different operating voltages. For current density maximization we investigate the optimal distribution of material parameters along the CL width.

For examining CL micro-structural sensitivity to PEFC performance, we further expand the agglomerate model. We first investigate the shape sensitivity of agglomerates on intra- and inter-agglomerate transport processes

via effectiveness factors and effective transport models. We also examine the agglomerate size sensitivity by generating self-similar CL structures and poly-disperse systems, possessing mixture of particle sizes. Furthermore, via examining multi-zone agglomerate, we introduce non-uniformly distributed sites for electrochemical reaction, called the triple phase boundaries. Our results demonstrate large sensitivity in simulation and optimization results for different CL structures.

We further investigate the particle level descriptions within GDL and polymer electrolyte membrane (PEM) sub-systems, moving one level down in the multi-scale hierarchy. For describing non-homogenous porous GDL, we introduce the lattice Boltzmann methods for estimating effective transport properties within composite porous media structures. For understanding relationship between PEM structures, water uptake and proton motion, we construct a coarse-grained bead spring molecular model for PEM, and perform molecular dynamics simulations. Finally, we present a novel multi-scale system integration strategy for systems described via different time and length scale phenomena, based on reduced order methods.

Acknowledgements

I have been extremely fortunate to have worked with Professors Biegler and Jhon as my thesis advisors. Their incessant enthusiasm towards research, vast knowledge, and complementing expertise especially for my project have truly made graduate school a tremendously enjoyable learning experience for me. Thank you bosses!

I would like to thank my committee members Prof. Erik Ydstie and Prof. Shlomo Ta'asan for their valuable feedback and suggestions during the course of thesis work. I would also like to thank my group members, faculty and staff of Chemical Engineering department at Carnegie Mellon, for their support and assistance with several things during the past four years.

I cannot express enough my gratitude towards my mother, Dr. (Mrs.) Sunita Jain, for her unconditional love, support, and sacrifices made to shape me as what I am. My brother, Mr. Pankaj Jain, has been my go-to-guy for almost anything, and his encouragement and support in all my endeavors, including graduate school, has always made me progress in life.

I would also like to thank several friends here at CMU and back in India,

who not only have been an excellent distraction during graduate school, but have taught me enormously on numerous things in life.

Contents

Abstract	iii
Acknowledgements	vi
List of Figures	xi
List of Tables	xvi
1 Introduction	1
1.1 Introduction to PEFCs	2
1.2 Multi-scale modeling and optimization in PEFCs	3
1.3 Research objectives	6
1.4 Outline of dissertation	7
2 Parametric Study and Estimation in CFD-based PEM Fuel	
Cell Models	10
2.1 Introduction	10
2.2 Physical modeling of H ₂ PEFC	15
2.3 Parameter estimation	23

2.3.1	Problem formulation	23
2.3.2	Numerical procedure	26
2.3.3	Application to PEFC system	28
2.4	Parametric studies	32
2.4.1	Flow arrangement	33
2.4.2	Inlet humidity	36
2.4.3	PEM thickness	38
2.5	Summary	40
3	Optimization of Polymer Electrolyte Fuel Cell Cathodes	47
3.1	Introduction	47
3.2	Physical modeling of PEFC cathode and its surroundings	50
3.3	Numerical procedure	54
3.4	Results and discussion	56
3.4.1	Pt minimization	57
3.4.2	Maximization of Current Density	58
3.5	Generalization to three dimensional system	61
3.6	Summary	66
4	Sensitivity of PEFC Models with Cathode Layer Micro - Structures	71
4.1	Introduction	71
4.2	Effect of agglomerate shapes	74
4.2.1	Effectiveness factors	74

4.2.2	Transport properties	78
4.3	Effect of agglomerate size	81
4.3.1	Polydispersity	83
4.4	Spherical shell agglomerate	86
4.5	Summary	97
5	Multi-scale Modeling and System Integration	101
5.1	Introduction	101
5.2	Mesoscale methods for estimating effective transport in non-homogenous media	103
5.2.1	Lattice Boltzmann method	104
5.3	Molecular simulations for PEM	109
5.3.1	Molecular dynamics (MD) simulation	110
5.4	System integration	116
5.4.1	Proposed ROM integration strategy	120
5.4.2	ROM methodology when integrated system solution is available	123
5.5	Summary	126
6	Conclusions	130
6.1	Thesis conclusions and contributions	130
6.2	Recommendations for future work	136
6.2.1	Model sophistication (Continuum)	137
6.2.2	Multi-scale modeling and system integration	138

List of Figures

1.1	Schematic of basic mechanism of an H_2 PEFC.	3
1.2	A multi-component schematic of PEFC.	4
1.3	PEFC multi-scale modeling scheme.. . . .	5
2.1	A schematic of the H_2 PEFC , and the anode and cathode half cell reactions	16
2.2	A schematic of the H_2 PEFC model	17
2.3	The fitted $I - V$ curve for the 11-point case.	31
2.4	Water concentration (mol/m^3) profiles in (a) anode and cathode regions and (b) PEM water profiles (λ), for co-flow (left) and counter-flow (right) cases.	33
2.5	Variation of PEM water transport coefficients along the anode GDL-PEM interface for (a) co-flow and (b) counter-flow cases.	34
2.6	Polarization curves for counter-flow and co-flow cases.	35
2.7	PEM water concentration profile for RH = 80/80.	36
2.8	Polarization curves for different inlet humidity cases.	37

2.9	Variation of α and ζ_{elec} along the anode GDL-PEM interface for RH = 80/80.	37
2.10	Variation of PEM water transport coefficients along the anode GDL-PEM interface for (a) Nafion TM 117 and (b) Nafion TM 111 PEMs.	39
2.11	PEM water concentration profiles for (a) co-flow and (b) counter-flow cases.	39
2.12	I-V characteristic curves for Nafion TM 117 and Nafion TM 111 PEFCs.	40
3.1	A schematic of an agglomerate particle. r_{agg} is the inner cluster radius, and δ is the thickness of the electrolyte film encapsulating the inner cluster. Minute Pt particles are sprinkled over each of the carbon particle forming $Pt - C$ particulate.	50
3.2	A schematic of the 2D modeling domains. L_{cl} and L_{gdl} represent the width of the CL and the GDL regions.	51
3.3	(a) Pt minimization results at various current densities and voltages, and (b) fitted curves to logarithmic plots of m_{Pt}^* vs. I at different voltages.	57
3.4	$I - V$ characteristics curve for base and optimized designs for verification with Secanell et al. [2007]	59
3.5	Optimal catalyst distribution (a) histogram and (b) fitted curve across normalized CL width at voltage of 0.876 V.	60
3.6	A 3-D schematic of CL-GDL system with surrounding sub-components.	62

3.7	A 3-D schematic of CL-GDL system with uniform boundaries $x_{O_2}^B$ and ϕ_m^B	63
3.8	Volumetric current density profiles within (a) first & (b) third quadrant planes, and (c) 2-D case.	64
3.9	Volumetric current density profiles within (a) first & (b) third quadrant planes, and (c) \bar{j} with non-uniform boundary $x_{O_2}^B$. . .	65
3.10	Volumetric current density profiles within (a) first & (b) third quadrant planes, and (c) \bar{j} with non-uniform boundary ϕ_m^B . . .	66
3.11	Variation in I with broken symmetry parameter α	66
4.1	CL structures with (a) plate-like (1-D), (b) cylindrical (2-D), and (c) spherical (3-D) agglomerates.	73
4.2	Self-similar CL structures with different-sized agglomerates. . .	73
4.3	(a) $\langle \eta^{(d)} \rangle$, and (b) $\langle \xi_L^{(d)} \rangle$ curves for spherical, cylindrical, and plate- like shaped agglomerate particles.	76
4.4	I-V characteristics curves for spherical, cylindrical, and plate-like agglomerate particle shapes.	77
4.5	$I - V$ curves for different transport models.	80
4.6	(a) Space averaged Thiele's modulus and (b) effectiveness factor for different agglomerate sizes	82
4.7	(a)Space averaged Tafel current density and (b) cell output current density	82
4.8	I-V characteristic curves for two component mixtures	84

4.9	Current density for two component mixtures	86
4.10	A schematic of Cases I & II spherical shell agglomerates.	87
4.11	A schematic for derivation for effectiveness factor in Cases I & II.	87
4.12	Effectiveness of spherical shell with its thickness for different <i>Bi</i> . η and η_{sph} denote the effectiveness for a shell and sphere, respectively.	90
4.13	I-V characteristic curves for the pseudo homogenous, spherical shell agglomerate and sphere agglomerate models.	91
4.14	Effectiveness of two-zone agglomerate for varying thickness of zone 2.	94
4.15	Current density for different k_1/k_2 ratios for two-zone agglom- erate system	95
4.16	I-V characteristics curves with different zone 2 thicknesses	96
5.1	Our PEFC research milestone presented in this work.	102
5.2	A schematic of non-homogenous porous media	105
5.3	A schematic of discrete velocity vectors	106
5.4	Porous structures for (a) series, (b) parallel, (c) diagonal, and (d) random configurations.	108
5.5	PEM (a) molecular structure, and (b) model used in our simu- lation.	110
5.6	(a) PEM density and (b) radius of gyration for different water uptakes. $\sigma = 0.2 \text{ nm}$ is the reference length.	113

5.7	PCFs for (a)Na ⁺ -H ₂ O, (b) Na ⁺ -S, and (c) Na ⁺ -CF ₂	114
5.8	Water density distributions in a cross section of the simulation cell	115
5.9	MSD of counterions	116
5.10	Schematic of the proposed ROM methodology.	117
5.11	A schematic of two interacting systems A and B.	120
5.12	A schematic of linkages in Cases I, II, and III, and the resulting equation systems.	122

List of Tables

2.1	Parameter estimates for different number of I-V data point cases. . .	30
2.2	Computational details for each of multiple data point cases	31
2.3	Parameter definitions and values	46
3.1	Parameter values for base and optimized designs	59
3.2	Optimization for 2^N zones with total Pt mass constrained to 0.0001 g/cm^2 . $Pt/C = 0.280$, $\epsilon_{agg} = 0.5$, and $\epsilon_v^{gd} = 0.5$	60
3.3	Optimization results for uniform and non-uniform boundary cases.	67
4.1	Optimization results for spherical, cylindrical, and plate-like ag- glomerate particle shapes.	78
4.2	Optimization results for two different transport models.	81
4.3	Optimization results for mixture systems.	85
4.4	Optimization results for different shell thicknesses for Case I. . .	92
4.5	Optimization results for different shell thicknesses for Case II.	96
5.1	Validation results for series and parallel composite non-homogenous media	107

5.2	Effective conductivities for different porosities and structural arrangements. K_{rand} denotes effective conductivity for random structure.	109
5.3	Optimization results comparing proposed ROM and full GDL-CL model.	125

Chapter 1

Introduction

Design of new energy systems involves discovery of new materials, device assembly design, optimal operation at device and plant levels, as well as satisfying the environment, health, and safety regulations. With an extremely large number of trial and error cases involved in this process, systematic modeling and optimization strategies provide guidelines for experimental design. Energy systems comprise of multi-physical phenomena at different time and length scales, described through a hierarchy of scale-specific physical models. Hence, it becomes necessary to use holistic multi-scale models, which ensure that knowledge generated at one scale is transmitted to the other producing synergistic knowledge-base that fulfills stringent performance requirements.

Our work focuses on constructing a generalized framework for multi-phenomena, multi-scale integration, for systematic design and analysis of energy systems for achieving desired performance objectives. Owing to its complex physical phenomena at different time and length scales, hydrogen polymer electrolyte

fuel cell (PEFC) is an excellent benchmark candidate for examination of our multi-scale modeling and optimization approaches, and is the focus of this dissertation. In the following, we present a brief introduction to hydrogen PEFCs, followed by sub-component and system level descriptions that require multi-scale modeling and optimization. We then present the research objectives of this work, followed by the outline of the dissertation.

1.1 Introduction to PEFCs

In the past decade, research and development activities for commercialization of fuel cell systems as a potential power source for stationary, portable and automotive systems have increased rapidly. PEFCs have especially received attention owing to their higher power densities over the other types of fuel cells. Compared to conventional battery systems, the advantages of these systems are high operating efficiency, near-zero greenhouse emissions, operation on renewable fuels, reliable operation, and nearly instantaneous recharge capabilities [Mench et al., 2001].

A PEFC comprises of anode and cathode regions, and a central electrolyte, which is a polymer membrane. An H_2 PEFC converts the chemical energy of the cell reaction shown in Fig. 1.1 to electrical energy. The basic mechanism of an H_2 PEFC can be explained as following: Humidified hydrogen is fed to the anode, which decomposes to protons and electrons. These protons are transferred from anode to the cathode via the polymer electrolyte membrane

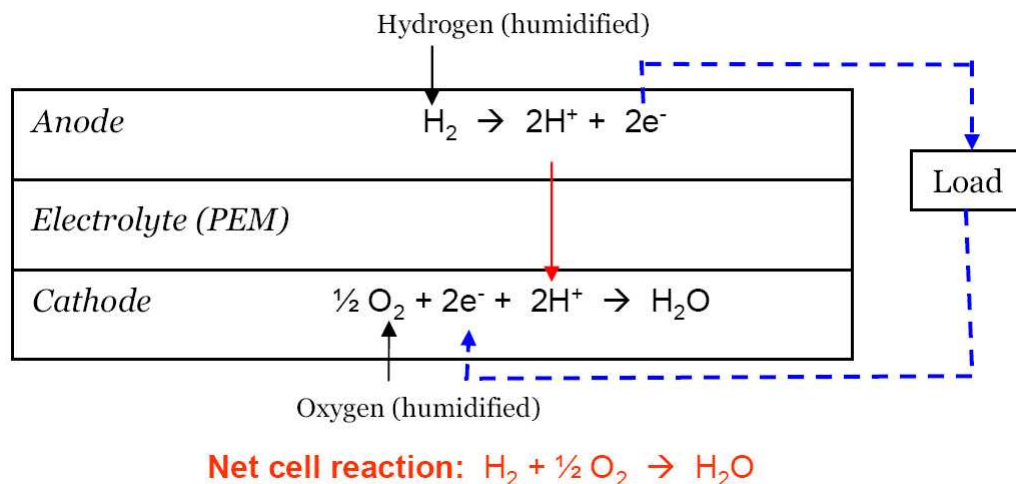


Figure 1.1: Schematic of basic mechanism of an H_2 PEFC.

(PEM), and electrons via an external circuit. At the cathode protons and electrons react with feed O_2 to form water product.

1.2 Multi-scale modeling and optimization in PEFCs

In spite of the above mentioned advantages in the PEFC technology, there are several cost, performance, and durability issues which need to be overcome before commercialization can be achieved. In order to motivate the discussion for modeling and optimization strategies which address these issues, we present here the PEFC sub-components in more details (Fig. 1.2). A single PEFC assembly comprises of seven key components: two gas channels (GCs), two gas diffusion layers (GDLs), two catalyst layers (CLs), and a PEM. The GCs are graphite bi-polar plates, which comprise of open channels for inlet and outlet of reactants and products. An issue in GC sub-components is to design

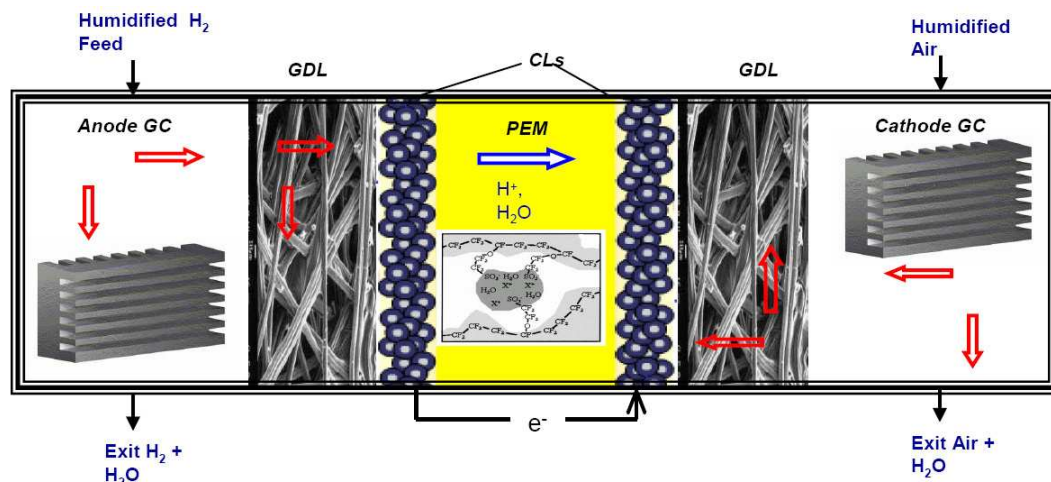


Figure 1.2: A multi-component schematic of PEFC.

the flow channels which maximize the cell performance. This flow phenomena is generally described via continuum level models.

The GDLs are porous carbon paper or interwoven cloth materials. The function of GDLs is to uniformly distribute reactants from GC to the CL, support the CL materials, and act as a passage for water removal. One of the key issues with this sub-component is blockage of pores by water due to water vapor condensation, which leads to additional mass transfer resistances to the reactant gases, especially on the cathode side. The problem boils down to designing the GDL structures (porosity and hydrophobicity), which may be addressed via meso-scale descriptions of two phase flows within porous media.

The CL comprises of platinum (Pt) particles supported on carbon, where the electrochemical reactions occur. The main issue with this sub-component is finding alternative catalyst materials, or CL structures, which lead to higher reaction kinetics, and are less expensive. This issue can be addressed by developing atomistic/molecular models.

Finally, the PEM sub-component maintains the potential difference between the anode and cathode regions, as well as conducts protons from anode to cathode. This proton conduction process is critical to PEFC performance as it may lead to significant ohmic losses in the cell. Alternative less expensive PEMs or PEM structures need to be designed possessing equal or higher conductivity than the state-of-the-art NafionTM and GoreTM PEMs. This issue may be addressed via molecular / supra-molecular level descriptions.

Figure 1.3 illustrates the PEFC multi-scale modeling scheme on time and length scales, where each subcomponent is placed at its most desirable modeling hierarchy.

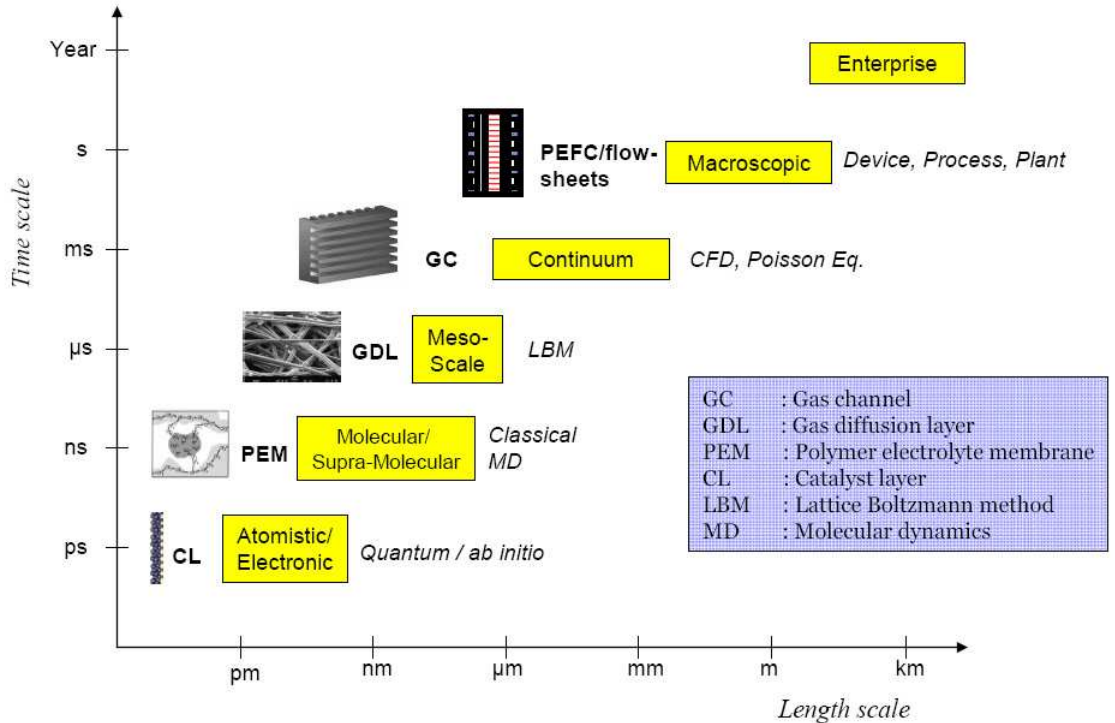


Figure 1.3: PEFC multi-scale modeling scheme.

The above mentioned component level issues need to be addressed based on

entire integrated system performance at the device / enterprise level. Hence, for addressing the PEFC technological issues, one attractive methodology will be to construct a 'holistic' integrated PEFC model in an efficient optimization framework, comprising of subcomponent descriptions at these different time and length scales. This would entail developing strategies for integrating these separated time and length models accurately, as well as within permissible computational expenses.

1.3 Research objectives

With PEFC as the benchmark case study for energy systems, we aim to construct model integration strategies for the following:

- Multiphysical phenomena comprising mass, momentum & energy transfer, including electrochemical reaction phenomena.
- Multiscale phenomena comprising the macroscopic and continuum levels within the standard engineering domains, and further extending into scientific domains to include mesoscopic and molecular level descriptions.
- Multi-component systems, *e.g.*, integrating GC, GDL, CL, and PEM sub-components in PEFCs.

We further aim to apply optimization as a model integration and design tool.

1.4 Outline of dissertation

Although we aimed at developing entire holistic multi-scale models in an integrated optimization framework, we partially achieved this goal, by starting with simplified integrated descriptions and systematically adding physics within each sub-system, initiating subsequent rounds of optimization.

This dissertation is organized in to six Chapters.

In Chapter 2, we introduce an integrated modeling and optimization framework for detailed computational fluid dynamics (CFD) based models for energy systems. We construct a multi-dimensional, multi-physics PEFC model accounting for major transport processes within GC, GDL, and PEM sub-components, with a phenomenological description within the CL sub-component, where parameter estimation is employed as a tool complementary to modeling. Also, parametric studies are performed, investigating the effect of flow arrangements, inlet humidity, and PEM thickness on detailed water transport and distribution characteristics, and on overall system performance. Incorporation of CFD based models in an efficient optimization framework is a key step towards holistic integrated modeling in energy systems.

In Chapter 3, we introduce a state-of-the-art continuum description for CL, the agglomerate model, for optimization of PEFC cathodes. The governing equations are discretized using a finite difference method and resulting optimization problem is linked to our inhouse state-of-the-art nonlinear programming algorithm. We perform platinum (Pt) minimization studies to obtain

relationships between optimal Pt mass and current density of operation. We further introduce non-homogeneity in CL, by systematically sub-dividing the CL in 2^N zones, each possessing different material compositions. We perform current density maximization for obtaining optimal Pt distributions along the CL width.

In Chapter 4, we further extend the agglomerate model description for including micro-structural information within our existing optimization framework, to examine the sensitivity of different CL structures to cell performance. Here we investigate the shape and size sensitivities of agglomerates on intra- and inter-agglomerate transport processes. We also examine polydisperse agglomerate systems, for several particle mixtures. Further, via introducing a spherical shell model, we explore non-uniform distribution in triple phase boundaries for electrochemical reaction.

In Chapter 5, we briefly explore the mesoscopic/molecular level descriptions within the GDL and PEM sub-components, by moving from field- to particle-level descriptions. Via lattice Boltzmann methods for GDL, we explore effective transport mechanisms within composite porous media structures, and through a molecular description for PEM, we explore the proton transport mechanisms, and dependence on PEM structure & water uptake. We further present, for multi-scale systems in which integrating methodologies are not available, an integration strategy based on reduced order methods.

In Chapter 6, we conclude the dissertation, as well as highlight the key contributions and accomplishments to the field of integrated multi-scale mod-

eling in energy systems, especially in PEFCs. Some directions for future work are also given.

Chapter 2

Parametric Study and

Estimation in CFD-based PEM

Fuel Cell Models

2.1 Introduction

In the past two decades, research and development activities for commercialization of polymer electrolyte fuel cell (PEFC) systems have increased rapidly as a potential power source for portable electronic devices, automotive systems, and power plant applications. Compared to conventional battery systems, the advantages of these systems are high operating efficiency, near-zero greenhouse emissions, operation on renewable fuels, reliable operation, and nearly instantaneous rechargeable capabilities. Also, there is tremendous interest in the technology due to recent ‘quantum jumps’ in the membrane electrode assem-

bly (MEA), the region most critical to PEFC performance [Costamagna and Srinivasan, 2001]. In spite of these developments, several design and operation related challenges need to be overcome before the commercial entry of PEFCs. These issues can be addressed through an optimization problem with an objective of maximizing the power density and minimizing the cost, for a given durability. Solving this problem requires repeated experiments that may be expensive and time consuming as there are numerous degrees of freedom in the system. With a plethora of parameters to be optimized and conditions to be satisfied, theoretical modeling is bound to play a pivotal role in achieving the objective.

Theoretical modeling in PEFC systems is a complex task as the system is an integrated assembly of several interacting physical components, each comprising of multi-dimensional, multi-physical transport and/or reaction processes. There have been numerous PEFC system modeling efforts beginning from the early 1990s [Springer et al., 1991, Bernardi and Verbrugge, 1991]. The model in Springer et al. [1991] assumed a perfectly mixed gas channel (GC), 1-D transport processes through gas diffusion layer (GDL), catalyst layer (CL) as a thin interface between GDL and polymer electrolyte membrane (PEM), and 1-D water transport within the PEM, thus accounting for non-uniform conductivity in the PEM. The model in Bernardi and Verbrugge [1991] incorporated a porous electrode model for the CL assuming however, a fully hydrated PEM. Although these models have limited applicability for large-scale FCs with high fuel utilization and wider operating ranges, they provided a funda-

mental basis for the forthcoming models. Gurau et al. [1998] presented a 2-D transport model for a PEFC and illustrated the utility of the model in examining multi-dimensional water and reactant distributions inside FC. Um & co-workers [Um et al., 2000, Um and Wang, 2004] applied computational fluid dynamics (CFD) approach to develop 2-D/3-D transport models. There have been numerous water management studies emphasizing on auto or low humidity operations [Hogarth and Benziger, 2006, Um and Wang, 2006]. In addition, various flow field patterns for bipolar plate design have been analyzed [Hyun et al., 2006]. The state-of-the-art models are complex to the extent that they account for multi-dimensional mass, momenta, energy, species, and charge transport phenomena in different regions of a FC. Using available software architectures there have been attempts of hybrid 3-D dynamic modeling in PEFC systems [Pantelides, 2004]. Modeling of GCs using FluentTM and MEA using gPROMSTM softwares has been illustrated for a 3-D temperature analysis [Matzopoulos, 2007]. Other complex phenomena including two-phase flow with non-isothermal effects, have received considerable attention as well [He et al., 2004, Wang et al., 2001, You and Liu, 2002, Nam and Kaviany, 2003, Ju et al., 2005, Wang and Wang, 2006]. However, many such transport and reaction processes in the system are not fully understood, and are often modeled using semi-empirical models containing unknown parameters. On the other hand, while more detailed and complex models claim to describe the physics more accurately, they generate more uncertain parameters. Hence, a rigorous methodology for parameter estimation for validating models with experimental

data is a very useful tool for PEFC systems. Moreover, an integrated systems model of PEFC can be thought as a combination of interacting sub-models of its various components. Hence parameter estimation is especially attractive for two reasons: (i) From model reduction and simplification point of view, a particular sub-component model may be modeled through a fitting function whereas more physics may be concentrated in other desired components and (ii) stand-alone measured properties of a sub-component may differ when the component is integrated with the entire system under operation.

In spite of numerous modeling studies [Wang, 2004], there have been only a few parameter estimation studies in PEFCs. Soares and Hoo [2000] estimated model parameters based on the model by Nguyen and White [1993], who accounted for heat transfer between solid and liquid phases and latent heat associated with evaporation and condensation of water. The pseudo 2-D problem (1-D for GC, and 1-D PEM) was solved by discretizing the differential algebraic equation (DAE) model using an orthogonal collocation method, and by solving the associated nonlinear program (NLP) by the successive quadratic programming (SQP) approach. Applying a 1-D model, Berg et al. [2004] fitted the voltage data for a specified current, from their experiments and estimated PEM conductivity, cathode exchange current density, PEM water transfer coefficient, and GDL oxygen mass transfer coefficient. Using 1-D charge and species balance in quiescent flow in GDL, CL, and PEM, Carnes and Djilali [2005] estimated PEM conductivity, GDL oxygen mass transfer coefficient, and exchange current densities by applying an algorithm for parameter estimation

with PDE constraints based on a nonlinear least squares approach.

All the above parameter estimation studies however, employ simpler PEFC models with fewer individual component models, less detailed treatment of transport processes, and have been limited to zero or one-dimension. In particular, none of these studies have dealt with detailed water transport models in all the PEFC components. These models are generally valid for a narrow range of operating conditions. As a result the parameters obtained lead to uncertainty in model predictions for large FC applications, particularly with high fuel utilization and wide range of operation.

The reasons for these limitations in PEFC parameter estimation studies is that the rigorous PEFC models are multi-dimensional and possess multi-physical phenomena that involve a large coupled system of partial differential algebraic equations (PDAEs). These models have been generally solved using commercial CFD codes that are unequipped to deal with large-scale PDAE-constrained optimization problems associated with the corresponding parameter estimation problems.

In this study, we present an integrated modeling and optimization framework for multi-dimensional, multi-physical PEFC models. We develop detailed transport models for GCs, GDLs, and PEM, along with a fitting function for the CL region, and formulate the parameter estimation problem as a PDAE-constrained optimization problem, with objective function that minimizes the model and experimental error between both input and output variables in the system. The problem is discretized in space leading to a large-scale NLP,

which is solved using a robust and efficient state-of-the-art interior point optimization solver, IPOPT [Wächter and Biegler, 2006]. The problem is solved with multiple experimental data points, which cover a wide range of operating conditions, yielding parameters that lead to accurate model predictions. We further employ this framework to perform parametric studies on water transport mechanisms and distribution within the PEFC system. We especially focus on parametric behavior of individual water transport processes within the PEM.

The remainder of this chapter is organized into the following components: physical modeling, parameter estimation, and parametric studies on water management in H₂ PEFCs.

2.2 Physical modeling of H₂ PEFC

A schematic of a H₂ PEFC and anode and cathode half cell reactions are shown in Fig. 2.1. A H₂ PEFC comprises of two GCs, two GDLs, two CLs each on the anode and cathode sides, as well as a central PEM. The GCs are bipolar plates, that are hollow chambers for fluid inlet and outlet. They also serve as a connection between adjacent cells. The GDLs are porous materials (typically carbon paper or carbon cloth) which support the catalyst/support particles, provide uniform distribution of gases, and act as a medium for electron transport from the CL to the external current collectors. The CLs are the usually platinum alloy particles supported on carbon, where the electrochem-

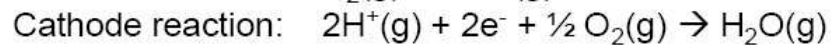
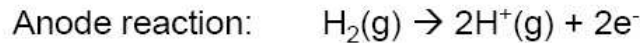
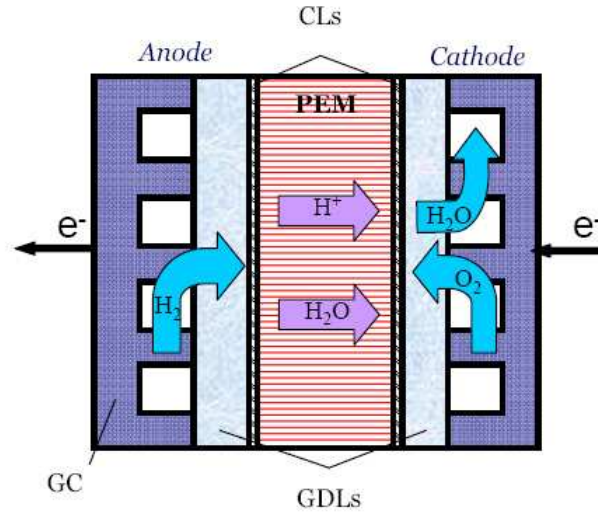
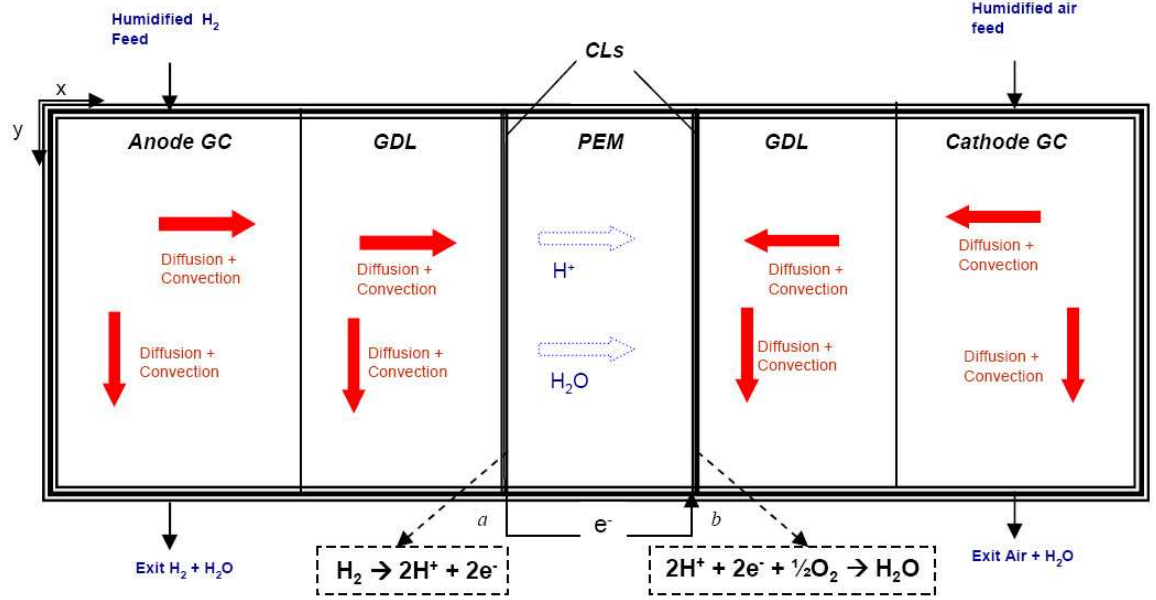


Figure 2.1: A schematic of the H₂ PEFC , and the anode and cathode half cell reactions

ical reactions take place. PEM is generally polytetrafluoroethylene chains with perfluorosulfonate side groups. The PEM acts as a proton transport passage from anode to the cathode, and this conductivity of the PEM is a strong function of its water uptake. We will construct a 2-D macroscopic model illustrated in Fig. 2.2. There are five chambers in the model, the GCs and the GDLs both on anode and the cathode sides, and a central PEM region. The humidified fuel and air are fed in the anode and cathode inlets, respectively. The species undergo a 2-D diffusion-convection process in both the GCs and the porous GDLs, after which they reach the PEM-GDL interface. On reaching the interface, hydrogen and oxygen undergo electrochemical reactions, and the water molecules are transported across the PEM from anode to the cathode. The protons released in the oxidation reaction at the anode are transported across

Figure 2.2: A schematic of the H₂ PEFC model

the PEM, and electrons released reach the cathode via an external circuit. The protons and electrons on reaching the cathode combine with the oxygen in the reduction reaction to give water as the product.

The following assumptions are made in our model: (i) 2-D steady state model; (ii) isothermal condition is imposed in the entire modeling domain; (iii) both GDLs and PEM have isotropic porous media; (iv) the CLs are treated as thin interfaces between the GDLs and the PEM; (v) water remains in the vapor phase, and single phase flow takes place; (vi) cell current density remains constant; and (vii) anode overpotential is negligible in comparison to cathode overpotential and is neglected in the cell voltage calculation. In addition, the standard simplifications including laminar and incompressible flow, as well as negligible entrance effects have been imposed and numerically verified. In view of the assumptions made, we would stress here that the pur-

pose of our work here is to build an integrated modeling and optimization framework for distributed CFD-based PEFC models, and the model presented here is for illustrative purposes. Hence, there are many significant physical features lacking in the model, such as the charge and energy balance equations, which are important in determining the potential, current density, and temperature distributions, and may have significant effect on cell performance at high current densities of operation.

The governing equations for each of the modeling regions, the interface and boundary conditions, and the empirical correlations adopted, are summarized in the list of Eqs. (2.1)-(2.19). A description of the variables can be found in the Notation section, whereas the model parameters and their values are listed in Table 2.3, at the end of this Chapter. The gas diffusion coefficients listed are computed via the Fuller-Schettler-Giddings equation for binary gas pairs (pg. 5-51, Green and Perry [2008]), where as the gas viscosities are computed using Wilke's expression [Wilke, 1950].

Equations (2.1) and (2.2) are continuity and isothermal Navier-Stokes (N-S) equations descriptive for the fluid flow within the GCs. The species mass transport (for H_2 , H_2O and O_2) is described by the diffusion-convection equation, Eq. (2.3). In modeling the GDL, the porosity (ϵ) of media is assumed to be constant *i.e.*, there are no dilation and expansion effects. The total mass balance is described by Eq. (2.4). The N-S equation is modified by an

additional Darcy's drag term ($\propto \mathbf{v}$) - Eq. (2.5).

GC equations

$$\text{Total mass balance: } \nabla \cdot \mathbf{v} = 0 \quad (2.1)$$

$$\text{Momentum balance: } \mathbf{M}(\mathbf{v}, p) \equiv \nabla \cdot (\mathbf{v}\mathbf{v}) - \nabla \cdot (\nu^{eff} \nabla \mathbf{v}) + \frac{1}{\rho} \nabla p = 0 \quad (2.2)$$

$$\text{Species mass balance: } S_i(C_i, D_i) \equiv \nabla \cdot (\mathbf{v}C_i) - \nabla \cdot (D_i \nabla C_i) = 0 \quad (2.3)$$

GDL equations

$$\text{Total mass balance: } \nabla \cdot (\epsilon \mathbf{v}) = 0 \quad (2.4)$$

$$\text{Momentum balance: } \mathbf{M}(\epsilon \mathbf{v}, p) - \frac{\rho \nu^{eff}}{K} (\epsilon^2 \mathbf{v}) = 0 \quad (2.5)$$

$$\text{Species mass balance: } S_i(C_i, \epsilon^{0.5} D_i) = 0 \quad (2.6)$$

Water transport in PEM

$$\left[1 - 8.8 \frac{F \rho_m k_m}{I M_m \mu_m} \frac{\partial p_w}{\partial x} \right] \frac{\partial \lambda}{\partial x} - 8.8 \frac{F D_{w,m} \rho_m}{I M_m} \left[\frac{\partial^2 \lambda}{\partial x^2} + \frac{\partial^2 \lambda}{\partial y^2} \right] = 0 \quad (2.7)$$

Boundary conditions

Interface conditions between PEM and GDL

$$\text{H}_2 \text{ consumption: } S_{H_2} = -\frac{M_{H_2}}{2F} I \quad (2.8)$$

$$\text{H}_2\text{O transfer: } S_{H_2O} = -\alpha(x = a, y) \frac{M_{H_2O}}{2F} I \quad (2.9)$$

$$\text{O}_2 \text{ consumption: } S_{O_2} = -\frac{M_{O_2}}{4F} I \quad (2.10)$$

$$\text{H}_2\text{O generation: } S_{H_2O} = (1 + \alpha(x = b, y)) \frac{M_{H_2O}}{2F} I \quad (2.11)$$

Inlet velocity conditions

$$\text{At anode: } v_{0,a} = \xi_a \frac{A_m}{A_{ch}} \frac{I}{2FC_{H_2,0}} \quad (2.12)$$

$$\text{At cathode: } v_{0,c} = \xi_c \frac{A_m}{A_{ch}} \frac{I}{4FC_{O_2,0}} \quad (2.13)$$

Cell voltage equations

$$\text{Output cell voltage: } V_{cell} = V_{OC} - \eta_c - \eta_{ohm} \quad (2.14)$$

$$\text{Open circuit voltage: } V_{OC} = 1.23 - 0.9 \times 10^{-3}(T - 298.15) + \frac{RT}{4F} \ln(a_{H_2}^2 a_{O_2}) \quad (2.15)$$

$$\text{Cathode overpotential: } \eta_c = \beta_1 \ln I + \beta_2 \quad (2.16)$$

$$\text{Ohmic overpotential: } \eta_{ohm} = I \frac{L_m}{\sigma_{avg}} \quad (2.17)$$

Empirical correlations

$$\text{PEM conductivity: } \sigma = (0.005139\lambda - 0.00326) \exp \left[\frac{1}{303} - \frac{1}{T} \right] \quad (2.18)$$

$$\lambda \text{ vs. vapor activity: } \lambda = \begin{cases} 0.04 + 17.81a_w - 39.85a_w^2 + 36a_w^3 & \text{for } 0 < a_w \leq 1, \\ 14 + 1.4(a_w - 1) & \text{for } 1 \leq a_w \leq 3. \end{cases} \quad (2.19)$$

The species mass transport Eq. (2.6), is modified from the GC by multiplying D_i by a factor $\epsilon^{0.5}$ to account for the porosity, as given by the Bruggman's relation [Um et al., 2000]. Notice that $\epsilon = 1$ recovers the GC species mass transport equation, Eq. (2.3).

The PEM is considered impermeable to all species except the protons and water. To describe the water transport in PEM, a quantity λ is introduced, which is the ratio of the water molecules to the number of sulphonate ion groups ($SO_3^- H^+$). It is related to PEM water concentration ($C_{w,m}$) by

$$\lambda = \frac{M_m C_{w,m}}{\rho_m} \quad (2.20)$$

The total flux (\mathbf{N}_{Tot}) of water in the PEM comprises of three parts; electro-osmotic drag (\mathbf{N}_{elec}), diffusion (\mathbf{N}_{diff}), and hydraulic permeation (\mathbf{N}_{hyd}) [Yi

and Nguyen, 1998]. The electro-osmotic drag originates from the flux due to drag on water molecules by proton molecules from anode to the cathode side. It is given by [Springer et al., 1991]:

$$\mathbf{N}_{\text{elec}} = \frac{2.5}{22} \frac{\lambda}{F} \mathbf{I} \quad (2.21)$$

The diffusion is caused by the concentration gradient due to non-uniform water distribution within the PEM, and is given by [Springer et al., 1991]:

$$\mathbf{N}_{\text{diff}} = \frac{D_{w,m} \rho_m}{M_m} \nabla \lambda \quad (2.22)$$

The hydraulic permeation is generated due to the pressure gradient between the anode and cathode sides. It is given by [Yi and Nguyen, 1998]:

$$\mathbf{N}_{\text{hyd}} = \frac{\rho_m k_m \lambda}{M_m \mu_m} \nabla p_w \quad (2.23)$$

After summing up these three flux terms, we imposed a differential water mass balance in the PEM. By assuming a steady state, we have

$$\nabla \cdot (\mathbf{N}_{\text{elec}} + \mathbf{N}_{\text{diff}} + \mathbf{N}_{\text{hyd}}) = 0, \quad (2.24)$$

which can be expressed as Eq. (2.7) in 2-D. Equations (2.8) and (2.10) represent the rate of consumption for H₂ and O₂ (mass per unit time) due to electro-chemical reactions at anode and cathode CLs, respectively. In Eq. (2.9), S_{H_2O}

is the mass transfer rate of H_2O across the PEM from anode to the cathode, and α is the moles of water molecules transported in x -direction from anode to the cathode side per mole of proton transported. It is given by the following equation,

$$\alpha = \frac{\mathbf{N}_{\text{Tot}} \cdot \mathbf{i}}{I/F} = 2.5 \frac{\lambda}{22} - \frac{D_{w,m} \rho_m F}{M_m I} \frac{\partial \lambda}{\partial x} - \frac{\rho_m F k_m \lambda}{M_m I \mu_m} \frac{\partial p_w}{\partial x} \quad (2.25)$$

In Eq. (2.25), the three terms in the right hand side represent the electro-osmotic drag coefficient (ζ_{elec}), the back-diffusion coefficient (ζ_{diff}), and the hydraulic permeation coefficient (ζ_{hyd}) respectively. In Eq. (2.11), S_{H_2O} is the sum of the transfer rates of water molecules from anode to the cathode by electro-osmotic drag and water generation due to electrochemical reaction at cathode. Equations (2.12) and (2.13) represent the inlet velocity conditions at anode and cathode for specified stoichiometric ratios and current density. At the outlets of the GCs the velocity and concentration profiles are assumed to be fully developed.

The output cell voltage is calculated from Eq. (2.14). The open circuit cell voltage V_{OC} depends on the system temperature and pressure as shown in Eq. (2.15) [Bernardi and Verbrugge, 1991]. From Tafel kinetics, the cathode overpotential is modeled as a linear function of $\ln I$ with β_1 and β_2 as two fitting parameters (Eq. (2.16)). The parameters β_1 and β_2 represent the electrode properties that influence the FC performance. The ohmic overpotential is given by Eq. (2.17). The PEM conductivity (σ) is correlated to water concentration

(Eq. (2.18)) as reported in Springer et al. [1991]. Finally Eq. (2.19) provides relationship between λ and water vapor activity ($a_w = C_{H_2O}RT / P_{sat}$) at the GDL-PEM interface [Springer et al., 1991].

The boundary conditions for the model are as follows: (i) At anode and cathode inlets, velocity and concentration values are specified; (ii) At anode and cathode exits, the flow is assumed to be fully developed and pressure is specified; (iii) At walls, no slip condition and zero normal species flux are employed; (iv) At GDL-PEM interface, no slip condition and interfacial species consumption eqs. (2.8)-(2.11) are employed.

2.3 Parameter estimation

Once the PEFC model is constructed, we link the model to IPOPT, and perform parameter estimation. Here we first present the parameter estimation problem formulation, followed by the details of numerical procedure, and application to PEFC system.

2.3.1 Problem formulation

The model equations (2.1) - (2.19) form a set of PDAEs which is cast in the following compact form:

$$\begin{aligned}
 \mathbf{g} \left[\frac{\partial \mathbf{z}}{\partial x}, \frac{\partial \mathbf{z}}{\partial y}, \frac{\partial^2 \mathbf{z}}{\partial x^2}, \frac{\partial^2 \mathbf{z}}{\partial y^2}, \mathbf{z}(X), \mathbf{w}(X), X, \mathbf{p} \right] &= 0 \\
 \mathbf{h} [\mathbf{z}(X), \mathbf{w}(X), X, \mathbf{p}] &= 0 \\
 \mathbf{B} [\mathbf{z}(0), \mathbf{z}(1), \dot{\mathbf{z}}(0), \dot{\mathbf{z}}(1)] &= 0
 \end{aligned} \tag{2.26}$$

Here, \mathbf{z} denotes the differential state variables. The symbol \mathbf{w} represents the algebraic variables, and \mathbf{p} , the parameters. The symbol X represents the set $\{x, y\}$ of independent variables. The partial differential equations comprising of momentum, species mass, and total mass balance equations are denoted by $\mathbf{g}[\cdot]$, the algebraic equations including the cell voltage calculation equations and empirical correlations by $\mathbf{h}[\cdot]$, and the boundary conditions by $\mathbf{B}[\cdot]$. In (2.26), the bold symbol represents a vector.

For parameter estimation problem formulation an appropriate objective function needs to be chosen. Standard least-squares formulation approach leads to parameter estimates that minimize the error between model and experimental output variables, and therefore account only for errors due to model inadequacy and random errors in measurement of output variables. If the input variables have measurement errors as well, this approach however, is well known to give biased parameters [Moran, 1971]. For this, we employ the errors-in-variables-measured (EVM) formulation approach, that takes into account the errors of all measured variables, both inputs and outputs to the system. The corresponding parameter estimation problem is formulated as

the following optimization problem:

$$\begin{aligned}
 \min_{\mathbf{p}} \sum_{i=1}^N & [(\mathbf{w}_{i,O} - \mathbf{w}_{i,O}^M)^T \mathbf{V}_{\mathbf{w},\mathbf{O}}^{-1} (\mathbf{w}_{i,O} - \mathbf{w}_{i,O}^M) + (\mathbf{w}_{i,I} - \mathbf{w}_{i,I}^M)^T \mathbf{V}_{\mathbf{w},\mathbf{I}}^{-1} (\mathbf{w}_{i,I} - \mathbf{w}_{i,I}^M)] \\
 \text{s.t. } \mathbf{g}_i & \left[\frac{\partial \mathbf{z}_i}{\partial x}, \frac{\partial \mathbf{z}_i}{\partial y}, \frac{\partial^2 \mathbf{z}_i}{\partial x^2}, \frac{\partial^2 \mathbf{z}_i}{\partial y^2}, \mathbf{z}_i(X), \mathbf{w}_i(X), X, \mathbf{p} \right] = 0 \\
 & \mathbf{h}_i [\mathbf{z}_i(X), \mathbf{w}_i(X), X, \mathbf{p}] = 0 \\
 & \mathbf{w}_{i,O} - f_i [\mathbf{z}_i(X), X, \mathbf{p}, \mathbf{w}_{i,I}] = 0 \\
 & \mathbf{B}_i [\mathbf{z}_i(0), \mathbf{z}_i(1), \dot{\mathbf{z}}_i(0), \dot{\mathbf{z}}_i(1)] = 0 \\
 & i \in \{1, \dots, N\} \tag{2.27}
 \end{aligned}$$

where, N is the number of experimental data sets and index i is used to replicate the model equations and variables for each of these data sets. The first summation term in the objective represents the least squares error between the model and experimental output variables, $\mathbf{w}_{i,O}$ and $\mathbf{w}_{i,O}^M$ respectively, whereas the second term represents the error between the input variables $\mathbf{w}_{i,I}$ and $\mathbf{w}_{i,I}^M$. $\mathbf{V}_{\mathbf{w},\mathbf{O}}^{-1}$ and $\mathbf{V}_{\mathbf{w},\mathbf{I}}^{-1}$ denote the weighting matrices for output and input variables respectively, and represent the inverse of the corresponding covariance matrices. Superscript T represents the matrix transpose operator. The EVM formulation however, leads to an increase in the number of degrees of freedom in the optimization problem (2.27) by the number of data sets used in the problem, often posing additional computational challenges in optimization. The EVM variables are the current density, I (input), and cell voltage, V (output)

in this study.

2.3.2 Numerical procedure

The transport equations within the GC, GDL, and PEM compartments are discretized using a finite volume method (FVM). The entire modeling domain was sub-divided into finite volumes. We employed the staggered grid approach, where the velocity field components are defined at a staggered location on the grid with respect to the concentration and pressure variables. We have adopted the discretization procedure given in Patankar [1980].

Discretized equations of the PDAE system can be formulated as a generalized NLP of the following form,

$$\begin{aligned}
 \min \quad & f(x) \\
 \text{s.t.} \quad & c(x) = 0 \\
 & x_L \leq x \leq x_U
 \end{aligned} \tag{2.28}$$

The NLP algorithm employed in our study is IPOPT [Wächter and Biegler, 2006]. This algorithm is based on a barrier approach in which the variable bounds are treated by adding a logarithmic barrier term to the objective func-

tion, which casts the problem in (2.28) into the following form,

$$\begin{aligned} \min \varphi(x) &= f(x) - \hat{\mu} \sum_{i=1}^n \ln(x^{(i)} - x_L^{(i)}) \\ &\quad - \hat{\mu} \sum_{i=1}^n \ln(x_U^{(i)} - x^{(i)}) \\ \text{s.t.} \quad &c(x) = 0 \end{aligned} \tag{2.29}$$

with a barrier parameter $\hat{\mu} > 0$. Here, $x^{(i)}$ denotes the i^{th} component of the vector x . The degree of influence of the barrier is determined by the size of $\hat{\mu}$, and under mild conditions $x_*(\hat{\mu})$ converges to a local solution x_* of the original problem (2.28) as $\hat{\mu} \rightarrow 0$ [Fiacco and McCormick, 1990]. Consequently, a strategy for solving the original NLP is to solve a sequence of barrier problems (2.29) for decreasing barrier parameters $\hat{\mu}_l$, where l is the counter for the sequence of subproblems.

IPOPT follows a primal-dual approach and applies a Newton method to the optimality conditions of (2.29), leading to solution of the following linear system at each iteration k :

$$\begin{bmatrix} H_k + \Sigma_k & A_k^T \\ A_k & 0 \end{bmatrix} \begin{bmatrix} \Delta x \\ \Delta \Lambda \end{bmatrix} = - \begin{bmatrix} \nabla \varphi(x_k) + \nabla c(x_k)^T \Lambda_k \\ c(x_k) \end{bmatrix} \tag{2.30}$$

where we use the convention, $X = \text{diag}(x)$, etc., H_k is the Hessian of the Lagrangian function $f(x_k) + c(x_k)^T \Lambda_k$, $A_k = \nabla c(x_k)$ and $\Sigma_k = (X_k - X_L)^{-1}(V_a^k) + (X_U - X_k)^{-1}(V_b^k)$ is the barrier term. Global convergence of the Newton method is promoted by a novel filter line search strategy; detailed analysis

shows both global convergence and fast local convergence properties. More information on IPOPT can be found in Wächter and Biegler [2006] and on the following website: <https://projects.coin-or.org/Ipopt>.

The discretization of the NLP using FVM was performed manually for all the equations and physical modeling domains. This CFD implementation was carefully verified with the commercial CFD softwares (FluentTM and FEMLABTM), however no automated CFD software was employed to build this model. Instead for all calculations the discretized equations were programmed in the modeling environment AMPL [Fourer et al., 1992], which was linked to the IPOPT solver.

2.3.3 Application to PEFC system

We now illustrate the above methodology for parameter estimation in PEFC models using the current-voltage ($I-V$) data from Ticianelli et al. [1988] (from Fig.2.5, 20 wt.% Pt/C in supported electrocatalyst plus 50 nm sputtered film of Pt, 0.45 mg/cm^2 of Pt. Case 353 K, 3/5 atm), with output variable as V , and input variable as I . The goal here is to find parameter plus model combination which validates the experimental data for a wide range of operating conditions, which is achieved by using multiple $I-V$ data points in the parameter estimation problem. The model equations are replicated depending on the number of $I-V$ points chosen. The EVM approach minimizes the slanted distance between model and experimental points on the global $I-V$

curve.

Model parameters

We choose to estimate the following parameters in the PEFC system:

- **PEM water diffusion coefficient:** The significance in estimating this property lies in the accurate prediction of water holdup and transport characteristics within the PEM, which in turn is critical to the water management issue. However, the PEM diffusion coefficient depends upon the PEM structure, the pretreatment method used for a PEM type, its water uptake, and the counter-ions in the system, thus increasing the number of cases for which experiments need to be performed [Suresh et al., 2006]. The experimental studies performed [Springer et al., 1991, Motupally et al., 2000] have been limited mainly to NafionTM stand-alone PEMs, and there is scarcity of data for other PEMs, especially with *in situ* measurements. Our work, for the first time provides a systematic framework for estimating diffusion coefficients using a multi-dimensional, multi-physics modeling and optimization framework.
- **Parameters β_1 and β_2 in CL:** The focus of current study is water management and hence detailed physics is incorporated within the PEM. Within the CL region, we employ a Tafel type equation for cathode overpotential (Eq. (2.16)), with β_1 and β_2 representing the electrode properties.

Results

The EVM problem was solved for 3, 4, 7, and 11 $I - V$ data points and the estimated parameter values are summarized in Table 2.1.

Table 2.1: Parameter estimates for different number of I-V data point cases.

$I - V$ points	$10^9 D_{w,m} (m^2/s)$	β_1	β_2
3	1.77	0.054	0.423
4	1.64	0.047	0.416
7	1.60	0.045	0.412
11	1.72	0.047	0.418

The values of $D_{w,m}$ are within the range of values reported by other semi-empirical and experimental data sources [Motupally et al., 2000, Fuller and Newman, 1993]. On comparison of Eq. (2.16) with Tafel overpotential expression [Larminie and Dicks, 2002], the values of β_1 and β_2 from the 11-point case correspond to an electrode charge transfer coefficient value of 0.32 and a exchange current density value of $1.37 \times 10^{-4} A/cm^2$ which are well within their respective physical ranges. The fitted I-V curve for the 11-point case is illustrated in Fig. 2.3.

Table 2.2 illustrates the computational details of the associated NLPs for different data point cases. NZJ and NZH denote the number of nonzero entries in the Jacobian and Hessian matrices, respectively.

The problems were solved on a 3.4 GHz processor, 4 Gb RAM, Pentium IV machine. The problems in each case were initialized by the solution of square problem simulation cases. The value of the objective (residual) for

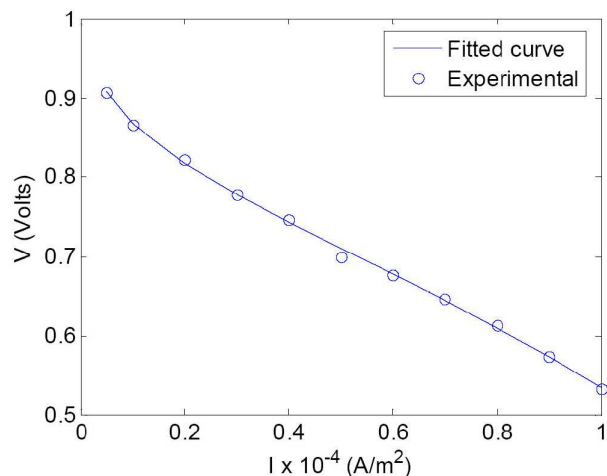
Figure 2.3: The fitted $I - V$ curve for the 11-point case.

Table 2.2: Computational details for each of multiple data point cases

$I - V$ points	Residual	Variables	Constraints	Iters.	CPUs	NZJ	NZH
3	6.97×10^{-13}	19 944	19 938	17	49.06	115 815	34 599
4	3.58×10^{-05}	26 591	26 584	17	55.59	154 420	46 132
7	6.27×10^{-05}	46 532	46 522	25	143.19	270 235	80 731
11	3.48×10^{-04}	73 120	73 106	23	259.54	424 655	126 863

the 3-point case, which corresponds to same number of parameters as the number of data points, comes out to be nearly zero. Also the residual values increase with number of data points, as expected. The CPU times scale linearly with problem size. The 11-point case corresponds to a large-scale NLP of 73 120 variables which is solved in little over four minutes. Hence, the current optimization framework seems to be reliable and computationally efficient in dealing with larger parameter estimation and optimization problems in PEFC systems. Moreover, the reduced Hessian matrix at the solution of each of the problems is positive definite, which corresponds to the fact that the parameters

estimated are unique.

2.4 Parametric studies

In this section we present parametric study results which focus on the water management issue in PEFCs. Water management refers to the act of ensuring sufficient hydration of PEM to avoid ohmic losses, and to avoid liquid water flooding (thus, ensuring efficient product water removal) that blocks the active CL sites and GDL pores, thus hindering the gas transport from the GC inlet to the CL. The problem boils down to designing the GDL (porosity and hydrophobicity), the CL (thickness, composition, and particle size distribution) and determining optimal operating and design conditions (*e.g.*, optimal flow characteristics, inlet humidity, geometric parameters, temperature, pressure, and current density), that achieve the above goal.

Numerous water management studies in the PEFC literature elucidate water transport characteristics with various design and operating parameters in the system [Wang, 2004]. Hence the goal of current work is two-fold; to validate our modeling and optimization framework by reproducing similar parametric behaviors as reported in previous studies and then, to examine in more detail the parametric behavior of individual water transport processes especially within the PEM. In this section, using the parameters estimated from previous section, we perform parametric studies to see the effect of flow arrangement (co-flow or counter-flow with respect to anode and cathode inlet locations),

inlet gas humidity, and PEM thickness on water transport mechanisms and distribution in the system, and overall cell performance.

2.4.1 Flow arrangement

We first examine the effect of changing inlet gas flow directions in anode and cathode GCs on the cell water distribution and on overall performance. As observed from Fig. 2.4(a) (left), in the co-flow arrangement, water concentration

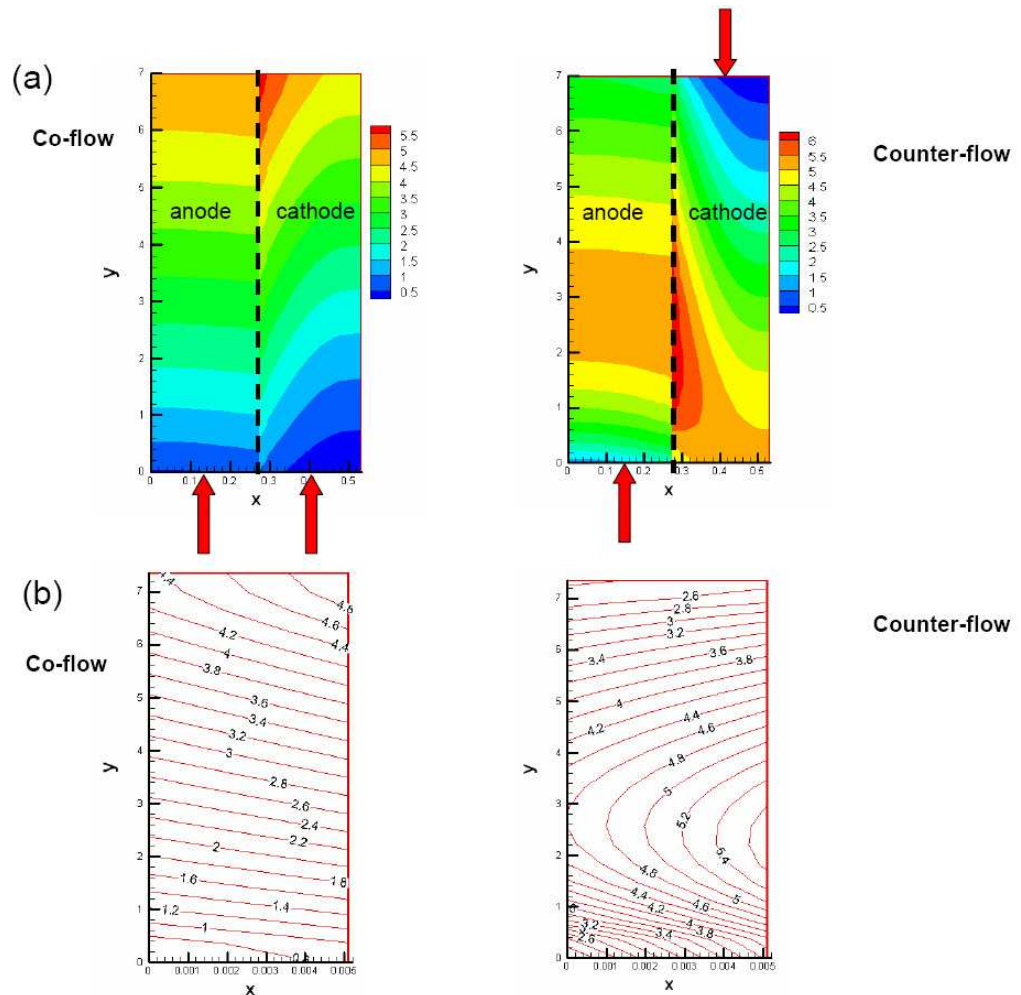


Figure 2.4: Water concentration (mol/m^3) profiles in (a) anode and cathode regions and (b) PEM water profiles (λ), for co-flow (left) and counter-flow (right) cases.

increases monotonically from the inlet to the outlet of the GCs, both within the anode and the cathode regions. Also, the PEM water concentration (Fig. 2.4(b) (left)) follows a monotonically decreasing trend from cathode to the anode side. On the other hand, in the counter-flow arrangement (right sides of Figs. 2.4(a) & (b)), there exists a maxima of water concentration in the middle region in both anode and cathode sides, and in the PEM region. Also, the gradient of water concentration in the PEM becomes multi-directional.

More detailed water transport characteristics can be observed from Figs. 2.5(a) & (b), which show the variation of individual water transport coefficients

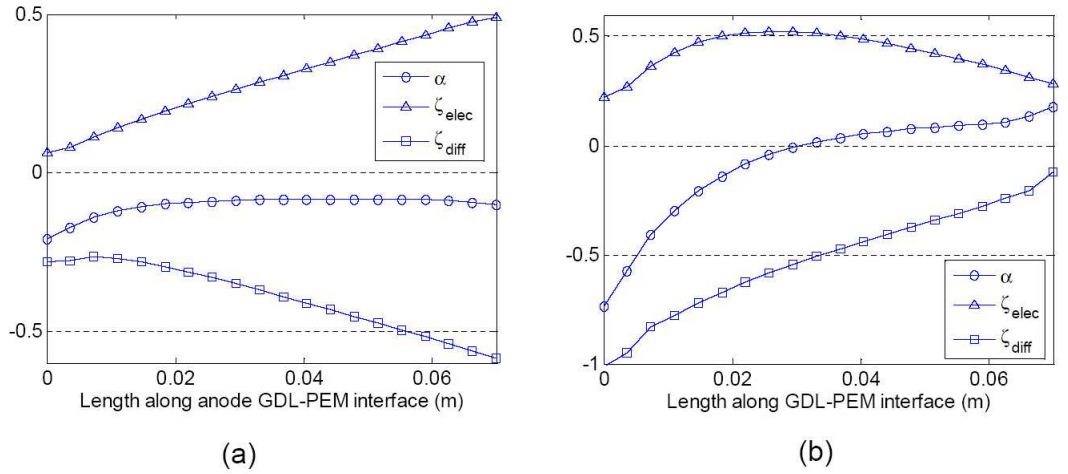


Figure 2.5: Variation of PEM water transport coefficients along the anode GDL-PEM interface for (a) co-flow and (b) counter-flow cases.

coefficients, defined earlier in Eq. (2.25), along the anode GDL-PEM interface for the co-flow and the counter-flow arrangements. For the co-flow arrangement (Fig. 2.5(a)), the electro-osmotic drag effect, which is directly proportional to λ , increases monotonically, but the diffusion effect acting in the opposite direction also increases at a similar rate. Since, the anode and cathode pressures

have been taken equal in these parametric studies, ζ_{hyd} remains zero throughout the length along the interface. The overall water transport coefficient α is therefore simply a summation of ζ_{elec} and ζ_{diff} , and remains constant and negative, as the diffusion effect dominates over the electro-osmotic drag effect.

For the counter-flow case (Fig. 2.5(b)) however, electro-osmotic drag coefficient possesses a maximum because of a maximum in water concentration along the GDL-PEM interface, whereas the back-diffusion coefficient decreases sharply. The sign of α changes in between from negative to positive, which indicates the presence of an internal water re-circulation in the counter-flow arrangement. This recirculation mechanism causes the PEM to hold higher amount of water and therefore, leads to a better performance via enhanced conductivity. The improved performance of the counter-flow case can be seen in Fig. 2.6 which compares the $I - V$ characteristic curves for the two flow arrangements. The disparity in the performances is especially visible for dry

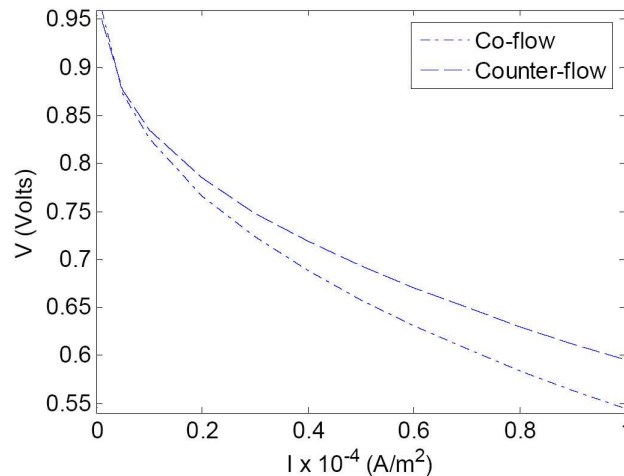


Figure 2.6: Polarization curves for counter-flow and co-flow cases.

to low humidities, and for lower pressures of operation. However, for higher

humidification conditions, the flow arrangement does not seem to affect the cell performance.

2.4.2 Inlet humidity

As inlet gas humidities increase, the overall water uptake in the system increases, which increases the ionic conductivity of the PEM and enhances the overall system performance. Figures 2.4(b, left) & 2.7 compare the PEM water

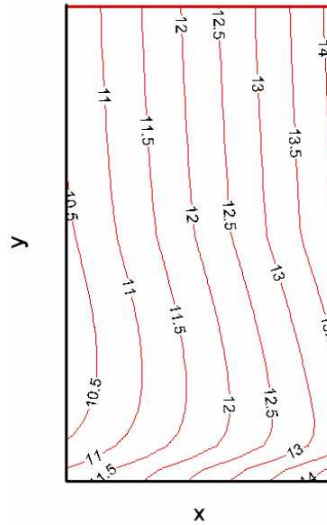


Figure 2.7: PEM water concentration profile for $RH = 80/80$.

uptakes of a totally dry inlet gas stream and the case where inlet humidities are set equal to 80/80 (xx/xx denotes relative humidity (RH) values at the anode and the cathode sides, respectively) in a co-flow arrangement. The average PEM water uptake increases by approximately four times in the latter case.

As seen from Fig. 2.8, the cell performance improves significantly from dry conditions to low humidity conditions (25 % RH in each anode and cathode

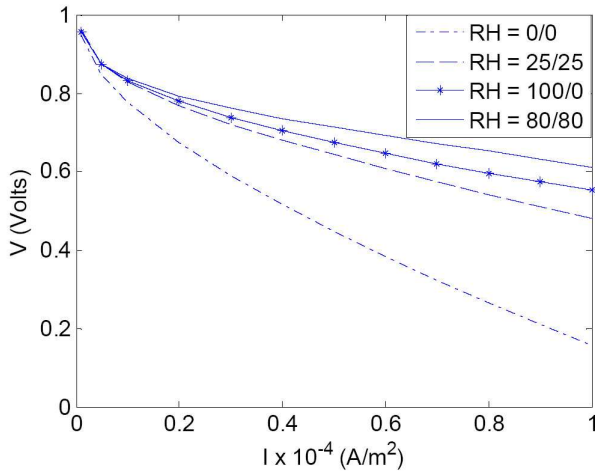


Figure 2.8: Polarization curves for different inlet humidity cases.

side), and the performance further improves in the cases of inlet humidities set equal to 100/0 and 80/80.

Figures 2.9(a) & (b) display the α and ζ_{elec} curves for a co-flow arrangement

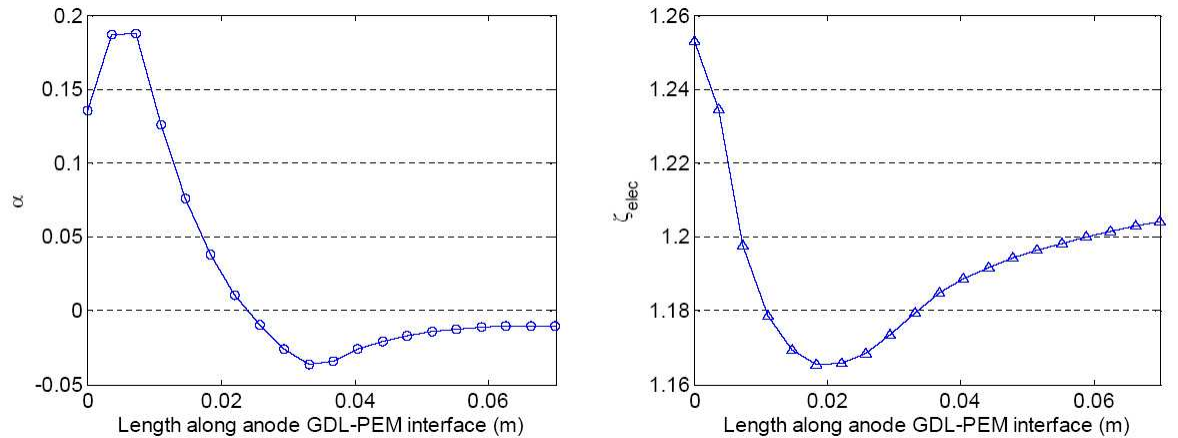


Figure 2.9: Variation of α and ζ_{elec} along the anode GDL-PEM interface for RH = 80/80.

with inlet humidities set as 80/80. In contrast to totally dry inlet humidity case where there is a unidirectional water flux from cathode to the anode side, the water transport in high inlet humidity case takes place from anode to the cathode side until a certain distance along the length, after which the water

transport direction reverses, as indicated by the switching in the sign of α in between. This may be explained in the following manner: for higher inlet humidity case, due to high water concentration near inlet, the electro-osmotic drag effect dominates over the diffusion effect and there is net transport of water from anode to the cathode side. However further down the channel, due to this loss of water from anode, and due to water production in the electrochemical reaction at the cathode, a sufficiently high water concentration gradient sets up in the opposite direction, and diffusion effect dominates over the electro-osmotic drag effect.

2.4.3 PEM thickness

PEM thickness affects the PEM conductivity in two main ways: (i) an increase or decrease in the proton transport path and (ii) through water distribution characteristics.

Figures 2.10(a) & (b) compare the water transport coefficients of NafionTM 117 (thickness 178 μm) and NafionTM 111 (thickness 25.4 μm) PEMs. Although there is only a slight modification in the overall transport coefficient α which becomes more negative for NafionTM 111, ζ_{elec} and ζ_{diff} increase significantly in magnitude, indicating increased water transport in NafionTM 111 as compared to NafionTM 117 in either the right or the left directions. This causes the water concentration to be more uniform in the x -direction for a thinner PEM as compared to a thicker PEM (Figs. 2.11 (a) & (b)). Hence, there exist

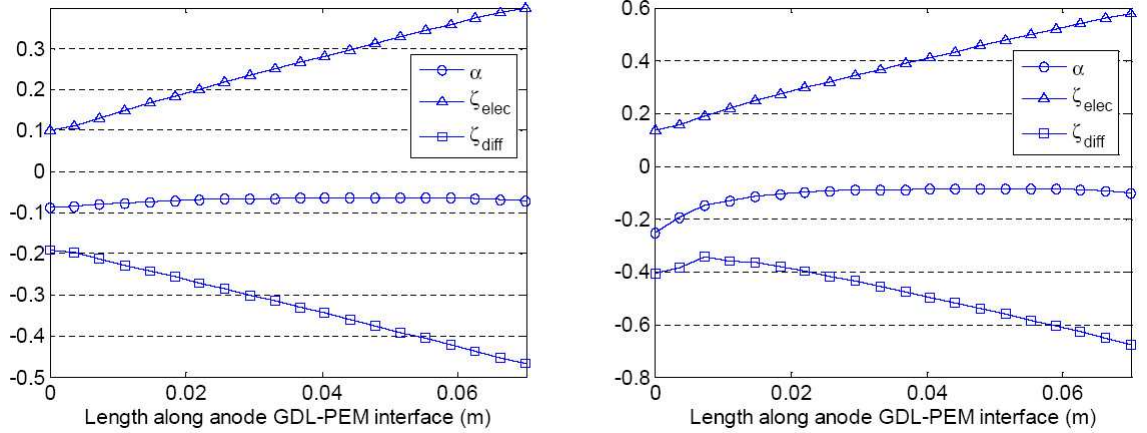


Figure 2.10: Variation of PEM water transport coefficients along the anode GDL-PEM interface for (a) NafionTM 117 and (b) NafionTM 111 PEMs.

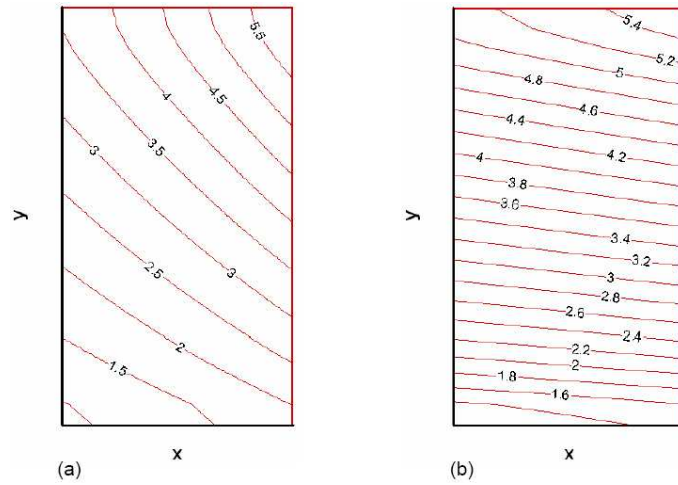


Figure 2.11: PEM water concentration profiles for (a) co-flow and (b) counter-flow cases.

regions (for high y values), where water concentration is uniformly high along the entire x -direction (or PEM width), which provide least resistance paths for proton transport. On the other hand, for thicker PEMs, water distribution is such that there are fewer, or no such regions of high proton conductivity along the entire PEM width.

Figure 2.12 shows a large difference in performances of NafionTM 117 and NafionTM 111 PEFCs. However, as shown in Fig. 2.12, counter-flow arrange-

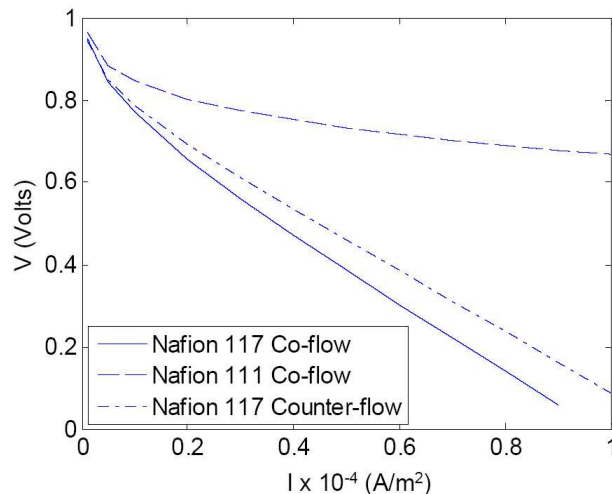


Figure 2.12: I-V characteristic curves for NafionTM 117 and NafionTM 111 PEFCs.

ment still leads to a better performance than the co-flow arrangement due to increased PEM conductivity via internal water recirculation. The co- and counter-flow (although not illustrated here) arrangements for NafionTM 111 gave similar performance.

2.5 Summary

In this Chapter we introduce a generalized modeling and optimization framework for rigorous CFD models in PEFC systems, with focus on integration of multi-component, multi-physics systems. Our PEFC model accounts for major transport processes within the GCs and the MEA, whereas CL is described phenomenologically. The resulting system of PDAEs is solved using a complete discretization approach in IPOPT solver. We perform parameter estimation for estimating CL fitting parameters and PEM water diffusion coefficient, and further employ this framework to perform water management

parametric studies. Specifically, we examine the effects of flow arrangements, inlet humidity, and PEM thickness on the water transport and distribution mechanisms within entire cell as well as on overall performance. The proposed methodology leads to fast and efficient solution of large-scale NLPs in a few CPU seconds and a few iterations.

Notation

a	=	Activity
A	=	Area, m^2
$\mathbf{B}[\cdot]$	=	Vector of boundary conditions
C	=	Molar concentration, mol/m^3
$diag$	=	diagonal matrix operator
D_i	=	Diffusion coefficient for species i , m^2/s
F	=	Faraday's constant, C/mol
$\mathbf{g}[\cdot]$	=	Vector of PDEs
$\mathbf{h}[\cdot]$	=	Vector of algebraic equations
H_k	=	Hessian of the Lagrangian function
\mathbf{i}	=	Unit vector in x-direction
I	=	Current density, A/m^2
\mathbf{I}	=	Current density vector, A/m^2
k	=	Hydraulic permeability, m^2
K	=	GDL permeability, m^2
L	=	Length, m
M_i	=	Molecular weight of species i , kg/mol
N	=	Number of data sets
\mathbf{N}	=	Flux, $\text{mol}/m^2 \cdot s$
p	=	Pressure, N/m^2
\mathbf{p}	=	Vector of parameters
R	=	Gas constant, $J/\text{mol} \cdot K$

-
- S = Consumption/production rate, kg/s
 T = Temperature, K
 v_0 = Inlet velocity, m/s
 \mathbf{v} = Velocity vector, m/s
 V = Voltage, Volt
 \mathbf{V} = Covariance matrix
 \mathbf{w} = Vector of algebraic variables
 X = set of independent variables
 \mathbf{z} = Vector of differential variables
 $\dot{\mathbf{z}}$ = Vector of derivative of differential variables

Greek symbols

- α = $[H_2O]/[H^+]$ transported
 $\beta_i (i = 1, 2)$ = Catalyst layer fitting parameters, Volt
 ϵ = GDL porosity
 η = Overpotential loss, Volt
 ζ = PEM water transport coefficient, dimensionless
 λ = $[H_2O]/[SO_3^- H^+]$ in PEM
 Λ = Lagrange multiplier
 μ = Viscosity, kg/m·s
 $\hat{\mu}$ = Barrier parameter
 ν = Kinematic viscosity, m^2/s
 ρ = Density, kg/m³

σ = PEM conductivity, S-m⁻¹

Σ_k = Barrier term

ξ = Stoichiometric ratio

Subscripts and superscripts

a = Anode

avg = Average

c = Cathode

ch = Channel

diff = Diffusion

eff = Effective value

elec = Electro-osmotic drag

gc = Gas channel

gdl = Gas diffusion layer

hyd = hydraulic permeation

I = Input

L = Lower bound

m = PEM

M = Measured

O = Output

OC = Open circuit

ohm = Ohmic

sat = Saturation value

T = Matrix transpose operator

Tot = Total

U = Upper bound

w = Water

0 = Value at the inlet conditions

Table 2.3: Parameter definitions and values

Symbol	Description	Value
A_{ch}	Cell inlet area(m^2)	$L_{gc} \times width$
A_m	Through plane direction area (m^2)	$L \times width$
D_{H_2}	Hydrogen diffusion coefficient(m^2/s)	3.95×10^{-5}
$D_{H_2O,a}$	Anode water diffusion coefficient(m^2/s)	3.95×10^{-5}
$D_{H_2O,c}$	Cathode water diffusion coefficient(m^2/s)	6.8×10^{-6}
D_{O_2}	Oxygen diffusion coefficient(m^2/s)	5.6×10^{-6}
F	Faraday's constant (C/mol)	9.65×10^4
\mathbf{i}	Unit vector in x-direction	
k_m	PEM hydraulic permeability (m^2)	1.8×10^{-18}
K	GDL permeability(m^2)	1.76×10^{-11}
L	Length along GC (m)	7.36×10^{-2}
L_{gc}	GC width (m)	2.54×10^{-3}
L_{gdl}	GDL width (m)	2×10^{-4}
L_m	PEM thickness (m)	1.27×10^{-4}
M_{H_2}	Hydrogen molecular weight (kg/mol)	2×10^{-3}
M_{H_2O}	Water molecular weight (kg/mol)	1.8×10^{-2}
M_{O_2}	Oxygen molecular weight (kg/mol)	3.2×10^{-2}
M_m	PEM equivalent weight (kg/mol)	1.1
R	Gas constant ($J/mol \cdot K$)	8.314
T	Cell temperature (K)	353.15
ϵ	GDL porosity	0.4
ν_a^{eff}	Anode gas kinematic viscosity (m^2/s)	2.44×10^{-5}
ν_c^{eff}	Cathode gas kinematic viscosity (m^2/s)	4.1×10^{-6}
μ_m	PEM viscosity ($kg/m \cdot s$)	2.14×10^{-3}
ρ_a	Anode gas density (kg/m^3)	$C_{H_2,0}M_{H_2} + C_{H_2,0,a}M_{H_2,0}$
ρ_c	Cathode gas density (kg/m^3)	$C_{O_2,0}M_{O_2} + C_{H_2,0,c}M_{H_2,0}$ $+C_{N_2,0}M_{N_2}$
ρ_m	PEM density (kg/m^3)	2×10^3
ξ_a	Anode stoichiometric coefficient	1.2
ξ_c	Cathode stoichiometric coefficient	2.6

Chapter 3

Optimization of Polymer

Electrolyte Fuel Cell Cathodes

3.1 Introduction

Out of the several performance losses within a polymer electrolyte fuel cell (PEFC), maximum overpotential losses take place within the cathode catalyst layer (CL) [Wang, 2004]. These losses occur due to sluggish oxygen reduction reaction (ORR) kinetics and sub-optimal operation. For ORR to proceed efficiently, the reactants (oxygen, protons, and electrons) need high mass transfer rates through the CL and need to meet together for reaction to occur. The CL comprises three phases, (*i*) the void space for oxygen/water transport, (*ii*) the electrolyte phase for proton transport, and (*iii*) the electro-catalyst phase for electron transport. These transport phenomena compete among each other depending on the composition and distribution of the three phases. With a

plethora of parameters to be optimized, systematic modeling and optimization studies provide guidelines in selecting the composition and distribution of CL materials (or phases) that maximize the output current density and minimize the consumption of the expensive platinum (Pt) catalyst.

There have been limited attempts to optimize the CL parameters mathematically, in spite of numerous modeling efforts. Using a simplified 1D CL model, Song et al. [2005] determined optimal Pt and electrolyte distributions along the CL width by maximizing the current density at a specified cell voltage. In their calculations, the optimal distributions increase along the CL width from gas diffusion layer (GDL) to the PEM interfaces. Rao and Rengaswamy [2006] presented a single agglomerate particle model and maximized the current density and minimized the Pt content for several voltage values. Their approach, although among the first of its kind, does not couple CL to any adjacent layers. Furthermore, their methodology for optimization is not suitable to deal with large-scale optimization problems. Recently, Secanell et al. [2007] have presented benchmark study on the optimization of entire CL using a gradient based optimization framework based on adaptive mesh refinement and capable of performing multi-variable optimization. They employed a detailed agglomerate model into their optimization framework to determine the optimal Pt content, mass ratio of Pt to carbon (Pt/C), void fraction in the GDL, and optimal characteristics of individual agglomerates that maximize cell current density for a specified voltage. Their study, according to the best of our knowledge, is the first systematic multi-variable optimization study

of CL dealing with a sophisticated agglomerate model. The model is linked to adjacent GDL, and can be integrated with entire system. However, their approach based on single-domain (combined GDL and CL) formulation appears to have numerical difficulties due to redundancy in the governing equation for the electrolyte phase potential, and may need more efficient algorithm for large-scale simulations.

In this Chapter, we introduce a modified double-domain (and can be easily generalizable for 2^N CL + GDL domains) form based on the agglomerate CL-GDL model reported in Secanell et al. [2007] We discretize the governing equations using a finite difference method and implement the discretized equations in an equation oriented modeling environment AMPL ‘A Mathematical Programming Language’ [Fourer et al., 1992], which are solved using a state-of-the-art general purpose interior point optimization solver (IPOPT) [Wächter and Biegler, 2006]. We have verified both the simulation and optimization results obtained by Secanell et al. [2007] and further performed Pt minimization. We then have determined, via current density maximization, the optimal distribution of Pt and other CL characteristic parameters along the width of the CL using IPOPT. This note illustrates the suitability of our formulation in dealing with large-scale optimization problems arising in the integration of detailed CL model with the remainder of PEFC system [Jain et al., 2008a].

3.2 Physical modeling of PEFC cathode and its surroundings

In the agglomerate model, shown schematically in Fig. 3.1, the CL is considered as a packed bed of spherical agglomerate particles with void spaces between the particles. Each agglomerate comprises numerous support carbon

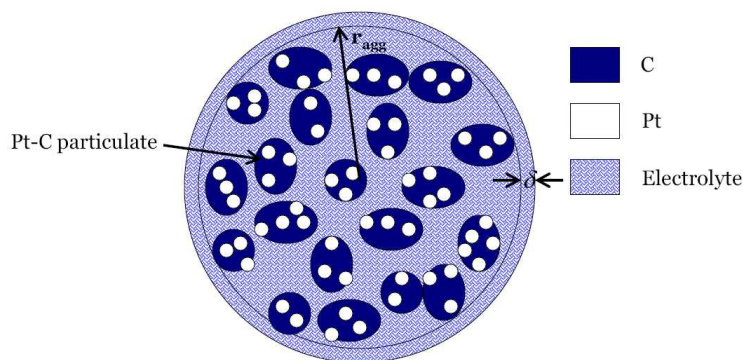


Figure 3.1: A schematic of an agglomerate particle. r_{agg} is the inner cluster radius, and δ is the thickness of the electrolyte film encapsulating the inner cluster. Minute Pt particles are sprinkled over each of the carbon particle forming $Pt-C$ particulate.

particles with tiny Pt particles distributed on their surface. These carbon particles are interwoven in electrolyte fibers to form a spherical cluster, which is encapsulated by a thin layer of electrolyte.

A 2D schematic of the combined CL and GDL system is sketched in Fig. 3.2. The oxygen and water molecules enter through the GDL, and diffuse through the pores of the GDL before reaching the CL. Within the CL, the molecules diffuse through the void spaces in between the agglomerates and arrive at the agglomerate surface. The oxygen and water molecules then dissolve in

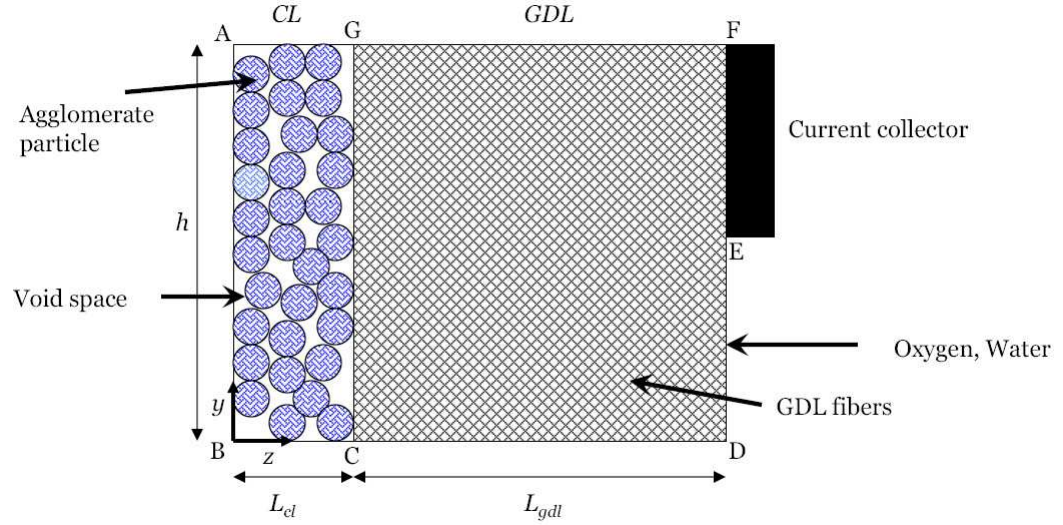


Figure 3.2: A schematic of the 2D modeling domains. L_{cl} and L_{gdl} represent the width of the CL and the GDL regions.

the thin electrolyte film, diffuse through it, and finally diffuse into the inner cluster, where the oxygen molecules react with protons and electrons at the interface of electro-catalyst and the electrolyte, and form product water. The product water and water from the inlet determine the proton conductivity of the electrolyte material within the CL [Springer et al., 1991].

The primary physical model used in our simulation/optimization includes (i) Oxygen transport in GDL pores, (ii) Electron transport through GDL fibers, (iii) Oxygen transport in CL void spaces, (iv) Oxygen dissolution into thin agglomerate film, (v) Oxygen diffusion through the film (vi), Oxygen diffusion in the electrolyte and reaction within the inner cluster, (vii) Proton transport in the electrolyte phase, and (viii) Electron transport through $Pt-C$ particles within CL.

The following is a condensed and reformulated presentation of the agglom-

erate model for CL and adjacent layers, used by the previous investigators [Se-canell et al., 2007]. The governing equations for water and oxygen transport within the GDL and CL regions are described by the following Poisson type equations:

$$\nabla \cdot \left(C_{tot} D_{H_2O}^{eff} (\epsilon_v^{gdl/cl}) \nabla x_{H_2O} \right) + \frac{(2\alpha + 1)}{2F} j = 0, \text{ and} \quad (3.1)$$

$$\nabla \cdot \left(C_{tot} D_{O_2}^{eff} (\epsilon_v^{gdl/cl}) \nabla x_{O_2} \right) - \frac{1}{4F} j = 0, \quad (3.2)$$

with parameters listed in the nomenclature section. Others including Bruggeman's relations, used for calculating effective transport coefficients as a function of effective volume fractions of different phases (ϵ^{eff}), are found in other references [Nam and Kaviany, 2003]. Here Eq. (3.1), descriptive for water transport, is presented for completeness of the CL and adjacent layers. However, it was not used in actual simulation. The electron charge transport equation within CL and GDL is given by

$$\nabla \cdot \left(\sigma_s^{eff} (\epsilon_s^{gdl/cl}) \nabla \phi_s \right) + j = 0. \quad (3.3)$$

The governing equation for the proton charge transport within the CL is expressed as

$$\nabla \cdot \left(\sigma_m^{eff} (\epsilon_m^{cl}) \nabla \phi_m \right) - j = 0. \quad (3.4)$$

The volumetric current density j is

$$j = \frac{j^T(\mathcal{L}(3\xi_L)/\xi_L)}{1 + \frac{9(1-\epsilon_v^{cl})(1-\epsilon_{agg})\epsilon_{agg}^{1.5}}{\epsilon_s^{cl}\epsilon_v^{cl}} \frac{\kappa_{agg}}{1+\kappa_{agg}} \xi_L \mathcal{L}(3\xi_L)}, \quad (3.5)$$

with,

$$\xi_L = \frac{1}{3} \sqrt{\frac{H_{O_2,m}}{4(1-\epsilon_v^{cl})FP_{tot}\epsilon_{agg}^{1.5} \frac{D_{O_2,N}}{r_{agg}^2}}} \sqrt{\frac{j^T}{x_{O_2}}}. \quad (3.6)$$

Here, \mathcal{L} is the Langevin function used frequently in magnetics, κ_{agg} is the ratio between agglomerate film thickness δ and the inner cluster radius r_{agg} (Fig. 3.1), and j^T is volumetric current density of the standard Tafel type,¹

$$j^T = A_o \frac{m_{Pt}}{L} i_o^{ref} \left(\frac{P_{tot} x_{O_2}}{C_{O_2}^{ref} H_{O_2,m}} \right) \exp \left(\frac{\alpha F}{RT} (\phi_m - \phi_s) \right). \quad (3.7)$$

Here m_{Pt} is the mass of Pt per unit area. It is noted that j is related to $(j^T/x_{O_2})^{1/2}$ via ξ_L . The catalyst surface area per unit mass of the catalyst particle, A_o , is given by [Marr and Li, 1999]

$$A_o \times 10^{-6} = 2.2779(Pt/C)^3 - 1.5857(Pt/C)^2 - 2.0153(Pt/C) + 1.5850. \quad (3.8)$$

The relationship among phase volume fractions within the GDL and CL regions is given below. The subscripts v , m , and s denote the void, electrolyte,

and other solid phases, respectively.

$$\epsilon_v^{gd} + \epsilon_s^{gd} = 1, \text{ and} \quad (3.9)$$

$$\epsilon_v^{cl} + \epsilon_m^{cl} + \epsilon_s^{cl} = 1. \quad (3.10)$$

Here, the solid volume fraction within the CL, ϵ_s^{cl} , and the electrolyte volume fraction, ϵ_m^{cl} , are expressed as [Marr and Li, 1999]

$$\epsilon_s^{cl} = \left(\frac{1}{\rho_{Pt}} + \frac{1 - Pt/C}{\rho_C Pt/C} \right) \frac{m_{Pt}}{L_{cl}}, \text{ and} \quad (3.11)$$

$$\epsilon_m^{cl} = \frac{\epsilon_s^{cl}}{1 - \epsilon_{agg}} [\epsilon_{agg} + (1 + \kappa_{agg})^3 - 1]. \quad (3.12)$$

3.3 Numerical procedure

The simultaneous partial differential equations (PDEs), expressed in Eqs. (3.2) - (3.4), are solved using the following mixed boundary conditions. We have indicated the boundary points A through G in Fig. 3.2.

- Boundary AB ($z = 0, y \in [0, h]$): $\partial x_{O_2}/\partial z = 0$, $\phi_m = \Delta V$, and $\partial \phi_s/\partial z = 0$.
- Boundaries BD and AF ($z \in [0, (L_{cl} + L_{gd})]$, $y = 0$ and $y = h$): $\partial x_{O_2}/\partial y = 0$, $\partial \phi_m/\partial y = 0$, and $\partial \phi_s/\partial y = 0$.

- Boundary DE ($z = (L_{cl} + L_{gdl}), y \in [0, h/2]$): $x_{O_2} = x_{O_2}^0$, and $\partial\phi_s/\partial z = 0$.
- Boundary EF ($z = (L_{cl} + L_{gdl}), y \in [h/2, h]$): $\partial x_{O_2}/\partial z = 0$, and $\phi_s = 0$.

In addition, we impose the interfacial condition between CL and GDL in our double-domain formulation as opposed to the model reported by Secanell et al. [2007].

- Interface CG between CL and GDL: $D_{O_2}^{eff,cl} (\partial x_{O_2}/\partial z)_{z=L_{cl}^-} = D_{O_2}^{eff,gdl} (\partial x_{O_2}/\partial z)_{z=L_{cl}^+}$, $\partial\phi_m/\partial z = 0$, and $\sigma_s^{eff,cl} (\partial\phi_s/\partial z)_{z=L_{cl}^-} = \sigma_s^{eff,gdl} (\partial\phi_s/\partial z)_{z=L_{cl}^+}$.

The resulting algebraic equations, discretized using a finite difference scheme, together with Eqs. (3.5) - (3.12) can be formulated as a generalized nonlinear program (NLP) of the following form,

$$\begin{aligned}
 & \min f(x) \\
 \text{s.t.} \quad & c(x) = 0 \\
 & x_L \leq x \leq x_U
 \end{aligned} \tag{3.13}$$

where x represents all of the discretized variables. The NLP is implemented in AMPL environment and linked to IPOPT. The algorithm for IPOPT is based on a barrier approach in which the variable bounds (lower bound x_L and upper bound x_U) are treated via a logarithmic barrier parameter ($\hat{\mu}$) to the

objective function, which casts the problem (3.13) into the following form,

$$\begin{aligned} \min f(x) - \hat{\mu} \sum_{i=1}^n \left[\ln(x^{(i)} - x_L^{(i)}) + \ln(x_U^{(i)} - x^{(i)}) \right] \\ \text{s.t.} \quad c(x) = 0, \end{aligned} \tag{3.14}$$

with $\hat{\mu} > 0$. Here, $x^{(i)}$ denotes the i^{th} component of the vector x . Under mild conditions the solution of problem (3.14), $x_*(\hat{\mu})$, converges to a local solution of the original problem (3.13) as $\hat{\mu} \rightarrow 0$. IPOPT is based on a primal-dual approach and applies a Newton's method to the optimality conditions of problem (3.14). The global convergence is promoted by a novel filter line search strategy; detailed analysis shows both global and rapid local convergence properties. IPOPT solver, with object oriented form, is ideal for constrained optimization problems dealing with large-scale partial differential algebraic equations. Details on IPOPT are found in Wächter and Biegler [2006] and the following website: <https://projects.coin-or.org/Ipopt>.

3.4 Results and discussion

We separately investigate minimization of Pt and maximization of cell current density.

3.4.1 Pt minimization

We formulated the optimization problem for minimizing Pt content for specified voltage and current density values as,

$$\begin{aligned} & \min m_{Pt} \\ & \text{s.t. Governing equations (3.2) – (3.12)}. \end{aligned} \quad (3.15)$$

The decision variables in problem (3.15) were Pt/C , ϵ_{agg} and ϵ_v^{gdl} . Problem (3.15) was solved using IPOPT solver. As shown in Fig. 3.3(a), we found that the minimum amount of Pt required increases with the current density. The curve shifts upwards as the voltage of operation increases. This may

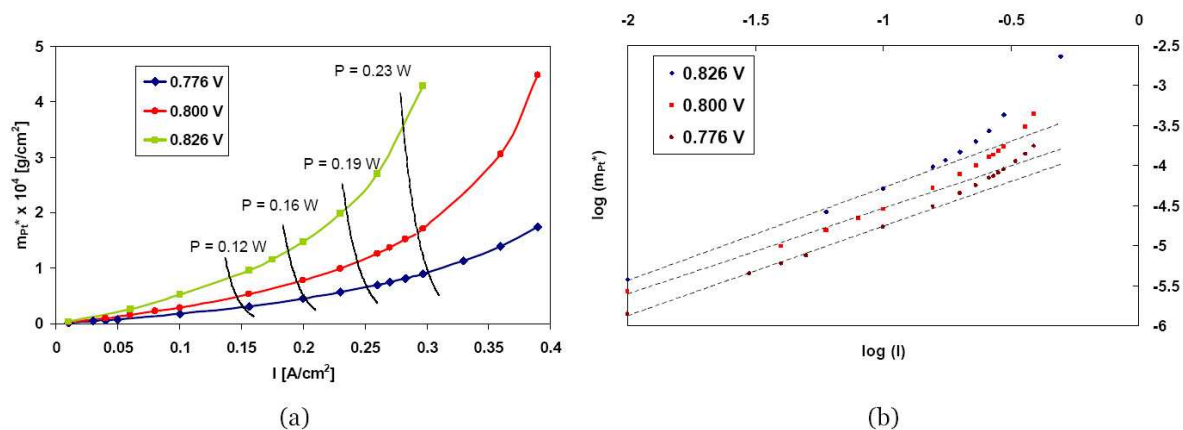


Figure 3.3: (a) Pt minimization results at various current densities and voltages, and (b) fitted curves to logarithmic plots of m_{Pt}^* vs. I at different voltages.

be explained from the fact that for a specified Pt amount current density decreases as cell voltage increases; therefore to generate the same current density at a higher voltage more Pt would be required. The constant power density

(P) curves are also shown in the figure. This family of curves provide the minimum amounts of Pt required for different current densities at a particular power density. Alternately, they provide information for the maximum current density obtainable from the fuel cell at a specified amount of Pt and given P .

In order to examine a relationship between m_{Pt}^* and I , we plot m_{Pt}^* vs. I at three different voltages. (Fig. 3.3b). The the following power law relation holds for low to medium current densities:

$$m_{Pt}^* = M(V)I^\beta. \quad (3.16)$$

The value of $\beta = 1.1$ remains nearly constant for different voltages, whereas $M(V)$ varies exponentially with V . The departure from linearity in Fig. 3.3(b) is most pronounced at higher voltages.

3.4.2 Maximization of Current Density

We formulated the problem for current density maximization as follows:

$$\begin{aligned} & \max I \\ & \text{s.t. Governing equations (3.2) – (3.12)}. \end{aligned} \quad (3.17)$$

Excellent agreement between Secanell et al. [2007] and our results was obtained, which verifies our reformulated double domain CL-GDL approach, as well as the numerical procedure reported here. As an illustration, the base

and optimized cases' $I - V$ curves are shown in Fig. 3.4, which is essentially identical to Fig. 11 in Secanell et al. [2007] Table 3.1 illustrates the base and optimized design values. We further extended our analysis to obtain the opti-

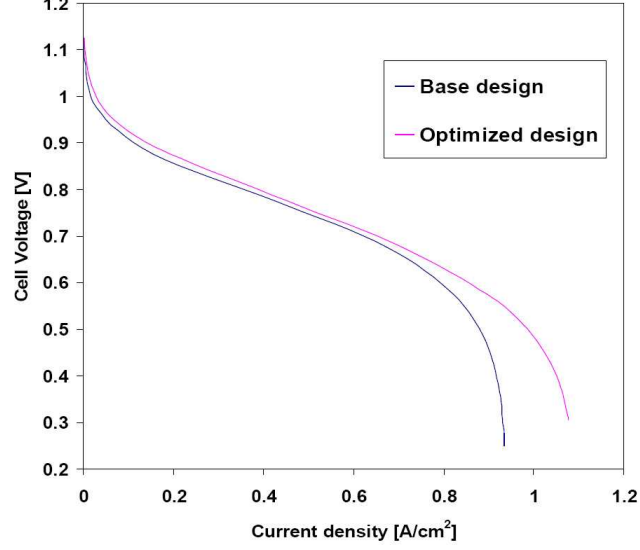


Figure 3.4: $I - V$ characteristics curve for base and optimized designs for verification with Secanell et al. [2007]

Table 3.1: Parameter values for base and optimized designs

Cases	$I^*(A/cm^2)$	$m_{Pt}(g/cm^2)$	Pt/C	ϵ_{agg}	ϵ_v^{gdl}
Base design	0.1556	0.0004	0.280	0.5	0.5
Optimized design (Ref. 4)	0.1936	0.0011321	0.467	0.3406	0.7257
Optimized design (Our results)	0.1917	0.0011264	0.467	0.3428	0.7377

mal Pt distribution along the CL width, *i.e.*, we introduced non-homogeneity. For this, we formulated a multi-zone optimization problem within the CL, where the number of vertically sliced zones within the CL equals 2^N ($N = 0, 1, 2$ etc.). Notice that $N = 3$ leads to 8 sets of the PDE's that made up the original problem. Each zone has a unique set of algebraic variable val-

ues $(\epsilon_v^{gdl}, \epsilon_s^{gdl}, \epsilon_v^{cl}, \epsilon_m^{cl}, \epsilon_s^{cl}, Pt/C, m_{Pt}, \epsilon_{agg}, A_0)$, which provides optimal Pt distribution as well as other algebraic variables. Each zone is linked to the adjacent zone through the continuity of concentration/potential fluxes, across the interface. Here, we illustrate the case of zones with equal width. Table 3.2

Table 3.2: Optimization for 2^N zones with total Pt mass constrained to 0.0001 g/cm^2 . $Pt/C = 0.280$, $\epsilon_{agg} = 0.5$, and $\epsilon_v^{gdl} = 0.5$.

N	$I^*(A/cm^2)$	$m_{Pt} \times 10^4 (g/cm^2)$ distribution from PEM-CL to CL-GDL interfaces
0	0.0331	1
1	0.0432	0.942 / 0.058
2	0.0467	0.840 / 0.099 / 0.036 / 0.025
3	0.0473	0.588 / 0.234 / 0.078 / 0.037 / 0.022 / 0.016 / 0.013 / 0.012

illustrates the optimal current density and Pt distribution values using the 2^N multi-zone scheme with equal width. In order to examine the effect of catalyst distribution the total Pt mass was fixed to 0.0001 g/cm^2 . Figure 3.5(a) shows the optimal catalyst distribution along the normalized CL width from PEM-CL to CL-GDL interface. Figure 3.5(b) demonstrates the fitted cata-

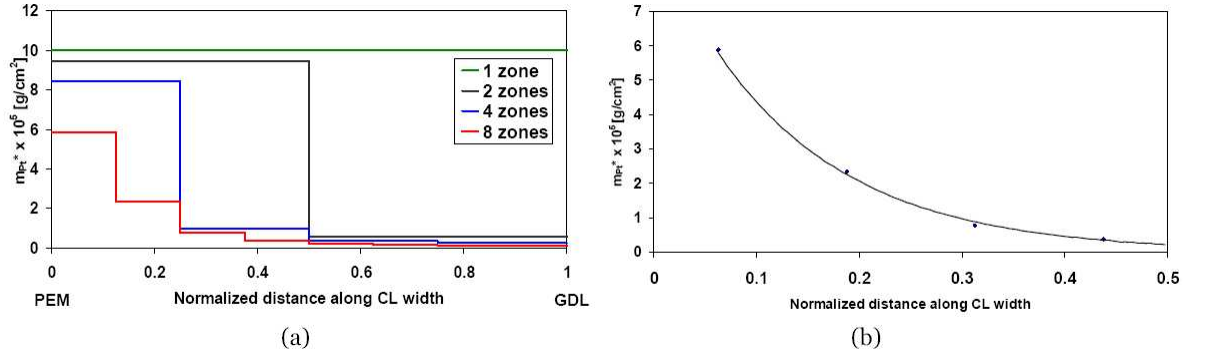


Figure 3.5: Optimal catalyst distribution (a) histogram and (b) fitted curve across normalized CL width at voltage of 0.876 V.

lyst mass distribution curve as a function of normalized CL width. The dots

shown in Fig. 3.5(b) are mid-points of the histogram steps in Fig. 3.5(a). The curve suggests an exponential decay rate from PEM-CL interface. Detailed analysis shows that this decay constant depends strongly on current density. The results from our preliminary analysis indicate that maximum cell current density is obtained when Pt is loaded mostly near the PEM-CL interface.

3.5 Generalization to three dimensional system

In this Chapter, we enhanced the phenomenological CL description presented in Chapter 2 to a state-of-the-art continuum CL description, and examined the two-dimensional GDL-CL system shown in Fig. 3.2. However, in an operating fuel cell, the phenomena within this GDL-CL system is dependent on the surrounding sub-components, the GC and the PEM, via the two-dimensional concentration (x_{O_2}) and electrolyte phase potential (ϕ_m) boundaries (referred as $x_{O_2}^B$ and ϕ_m^B , where superscript B refers to boundary) as shown in Fig. 3.6. Hence, before integrating this enhanced CL description with entire PEFC assembly, we examined the role of these boundaries, especially along the third (x) dimension, by extending our existing two-dimensional GDL-CL framework to three-dimensional system.

For this purpose, we generalized the field variables x_{O_2} , ϕ_m , ϕ_s , j , j^T , and ξ_L , as well as field equations (Eqs. 3.2-3.7) from two to three dimensions.

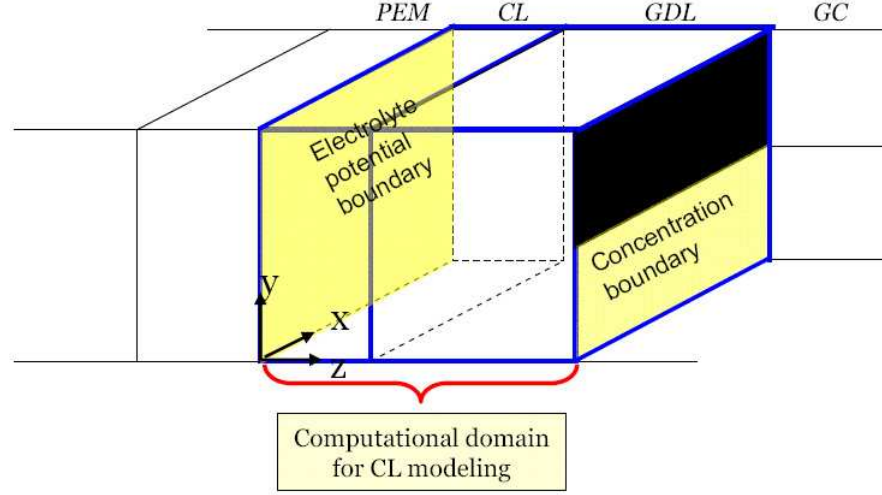


Figure 3.6: A 3-D schematic of CL-GDL system with surrounding sub-components.

Additional no flux boundaries at $y - z$ and $x - z$ faces (Fig. 3.6) for state variables x_{O_2} , ϕ_s , and ϕ_m were imposed. This generalization poses significant computational challenges, *e.g.*, a ten-fold increase in problem size (from 5 000 to 50 000 variables) from two to three dimensional system led to a 48 times increase in computational times (from 25 seconds to 20 minutes) approximately in IPOPT solver.

We first impose uniform boundaries $x_{O_2}^B$ and ϕ_m^B , along the $y - x$ planes (Fig. 3.7), setting $x_{O_2}(L_{cl} + L_{gdl}, y, x) = \langle x_{O_2} \rangle = 0.1773$ and $\phi_m(0, y, x) = \langle \phi_m \rangle = 0.5Volt$, where $\langle \rangle$ denotes the average value along the $y - x$ plane. In order to examine the sensitivity along the x direction, we examined the volumetric current density (j) profiles on the $x = W/4$ (referred as first quadrant) and $x = 3W/4$ (third quadrant) planes (Figs. 3.8a & b), where W is the width of the system along the x direction. As expected due to symmetry along x direction, the first and third quadrant profiles are identical. We

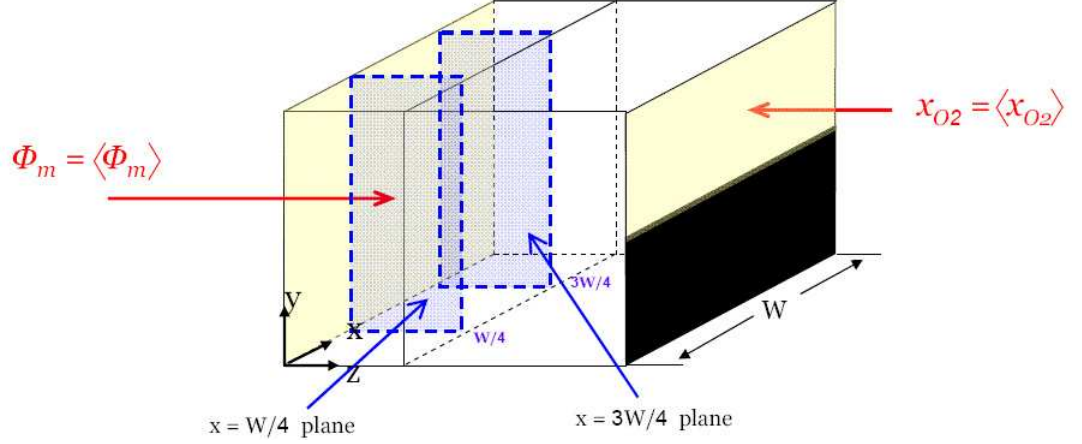


Figure 3.7: A 3-D schematic of CL-GDL system with uniform boundaries $x_{O_2}^B$ and ϕ_m^B .

further, compared these profiles for a three-dimensional system to previously examined two-dimensional volumetric current density profiles (Fig. 3.8c). We observe that Fig. 3.8(c) is in good agreement with both Figs. 3.8(a & b), which indicates that this three-dimensional system is equivalent to two-dimensional system when there exist uniform boundaries $x_{O_2}^B$ and ϕ_m^B from the GC and the PEM regions.

However, during a realistic PEFC operation, due to fuel & oxidant inlets and outlets along the x direction in the GC, the boundaries $x_{O_2}^B$ and ϕ_m^B are expected to be non-uniform. To illustrate the essence of asymmetric boundaries along x direction, we imposed a step change on $x_{O_2}^B$ as $x_{O_2}(L_{cl} + L_{gdl}, y, x) = (1 + \alpha)\langle x_{O_2} \rangle$ for $x \in [0, W/2]$, and $x_{O_2}(L_{cl} + L_{gdl}, y, x) = (1 - \alpha)\langle x_{O_2} \rangle$ for $x \in [W/2, W]$, where α is the ‘broken symmetry’ parameter, indicating the degree of non-uniformity in boundary along x direction. It is noted that $\alpha = 0$ recovers back the case with totally uniform boundaries. Figures 3.9 (a)&(b) illustrate the j profiles in the first and third quadrant planes for a non-uniform

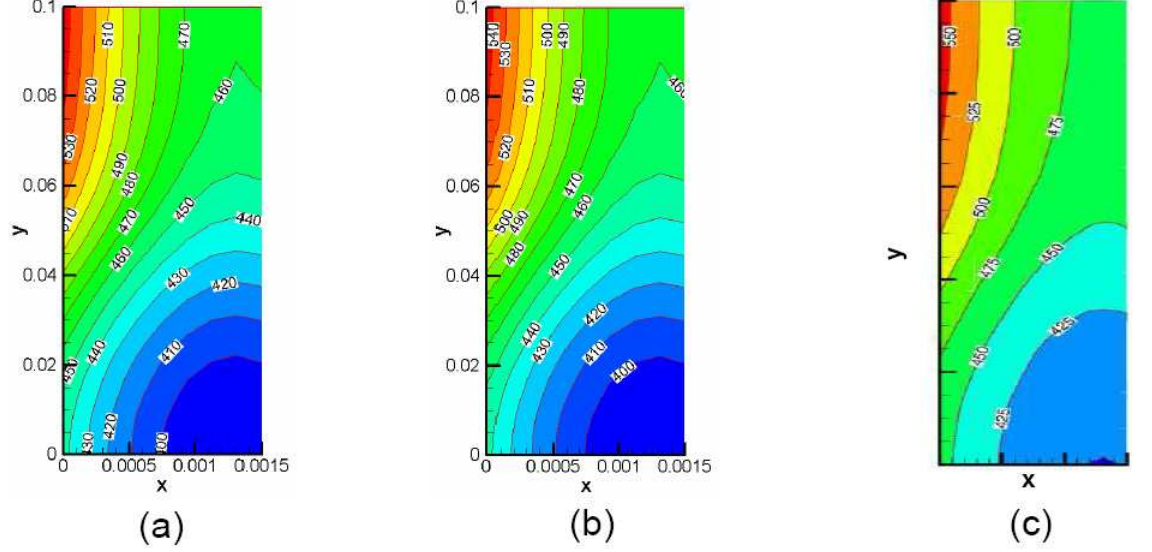


Figure 3.8: Volumetric current density profiles within (a) first & (b) third quadrant planes, and (c) 2-D case.

$x_{O_2}^B$ case, with $\alpha = 0.5$. It is observed, that j profiles significantly differ within the two planes, and j in first quadrant plane is almost twice as compared to the third quadrant plane. We also compared these profiles with the averaged volumetric current density along x direction ($\bar{j} = 1/W \int_0^W j dx$, Fig. 3.9 c). It is observed that \bar{j} significantly differs from the first and third quadrant volumetric current densities, however, is in qualitative agreement with Figs. 3.8 (a-c), indicating that asymmetry in $x_{O_2}^B$ may be proportionally translated within inner regions.

We further imposed asymmetric boundary ϕ_m^B along x direction, as $\phi_m(0, y, x) = (1 + \alpha)\langle\phi_m\rangle$ for $x \in [0, W/2]$, and $\phi_m(0, y, x) = (1 - \alpha)\langle\phi_m\rangle$ for $x \in [W/2, W]$. As observed from Figs. 3.10 (a)&(b), which illustrate the j profiles for a non-uniform ϕ_m^B case, with $\alpha = 0.5$, j in the first quadrant plane is an order of magnitude higher as compared to the third quadrant plane. Furthermore, \bar{j}

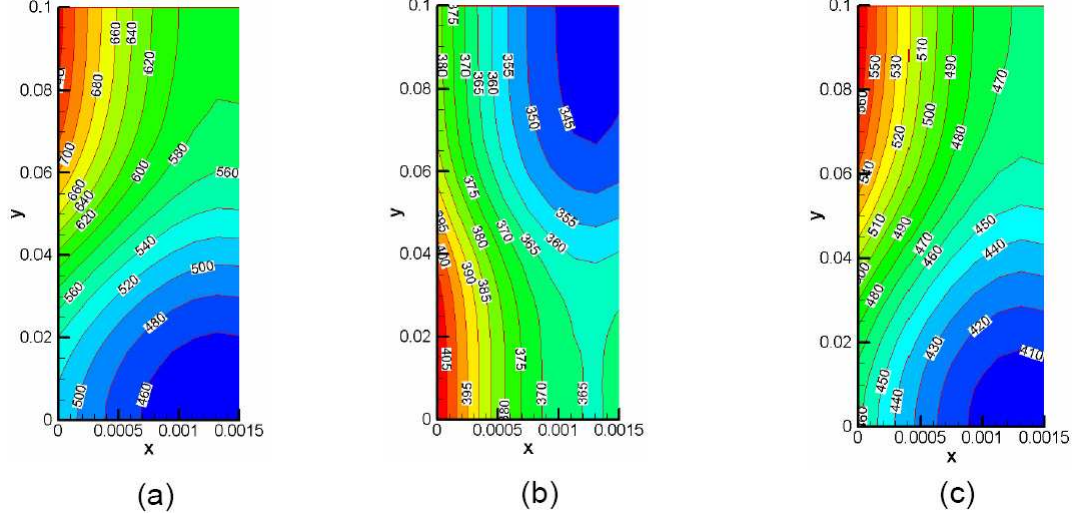


Figure 3.9: Volumetric current density profiles within (a) first & (b) third quadrant planes, and (c) \bar{j} with non-uniform boundary $x_{O_2}^B$.

(Fig. 3.10 c) significantly differs from j within first and third quadrant planes. On comparison of Fig. 3.10 (c) with Figs. 3.8 (a-c) we observe, \bar{j} significantly differs from two-dimensional profiles, as well as three-dimensional profiles with uniform $x_{O_2}^B$ and ϕ_m^B boundaries, indicating that asymmetry in ϕ_m^B is disproportionately translated within inner regions.

We systematically tuned the broken symmetry parameter α , and examined its effect on the overall cell current density I . As shown in Fig. 3.11, an asymmetry in $x_{O_2}^B$ leads to a small 3% change in I as α varies from 0 to 0.5. However, asymmetry in ϕ_m^B leads to a significant 18% change in I , indicating the significance for three dimensional generalization. Table 3.3 shows the optimization results for three dimensional system with $dV = 0.5\text{Volt}$, and $\alpha = 0.5$. It is observed that both base and optimized results for the uniform boundary case are identical to our two dimensional results. However, as non-uniformity in boundaries $x_{O_2}^B$ and ϕ_m^B is imposed, these results significantly

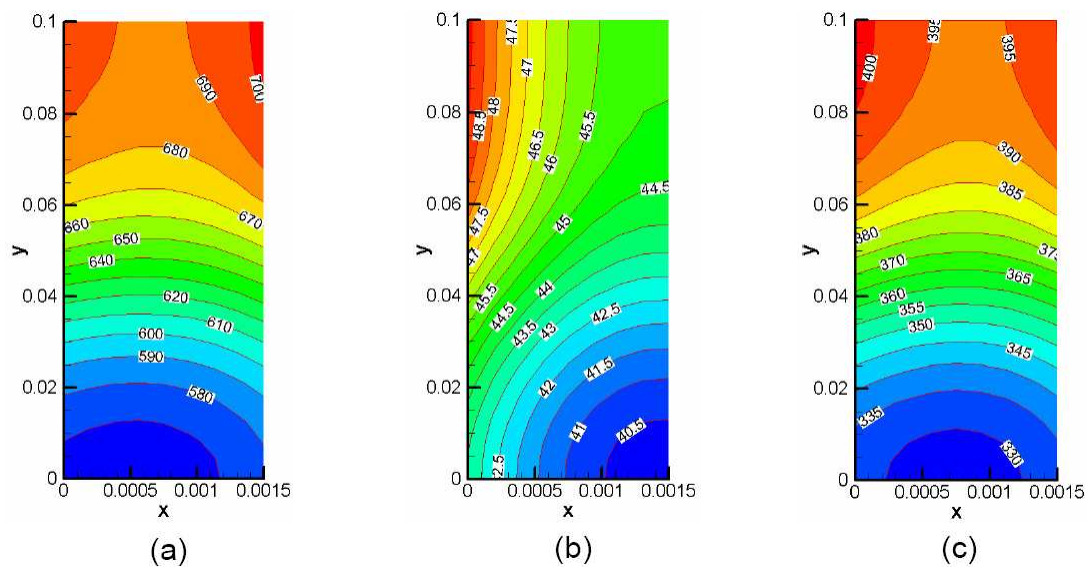


Figure 3.10: Volumetric current density profiles within (a) first & (b) third quadrant planes, and (c) \bar{j} with non-uniform boundary ϕ_m^B .

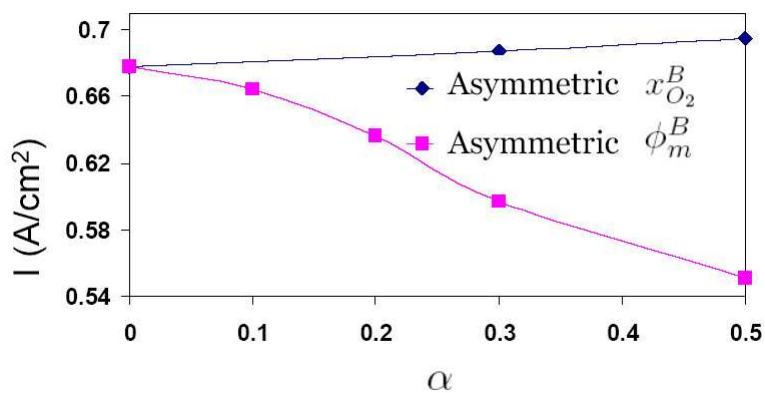


Figure 3.11: Variation in I with broken symmetry parameter α .

differ from the two dimensional case.

3.6 Summary

In this Chapter, we adopt an agglomerate CL model and reformulate into a condensed form, for the optimization of PEFC cathodes. This model accounts for major transport processes within GDL and CL, as well as electrochemical

Table 3.3: Optimization results for uniform and non-uniform boundary cases.

Case	$I^*(A/cm^2)$	$m_{Pt}^*(mg/cm^2)$	$(Pt/C)^*$	ϵ_{agg}^*	ϵ_v^{gdl*}
Uniform boundary base	0.678	0.400	0.280	0.500	0.50
Uniform boundary optimized	0.921	0.534	0.467	0.634	0.78
Asymmetric $x_{O_2}^B$	1.080	1.250	0.968	0.900	0.77
Asymmetric ϕ_m^B	1.170	1.250	0.980	0.846	0.90

reaction phenomena within individual agglomerates. The governing equations are solved using a full discretization approach in IPOPT optimization solver. We performed Pt minimization for a specified cell performance; the relationship between optimal Pt mass and current density obeys a power law at low to medium current densities of operation. In addition, we introduce a double domain approach for CL and GDL for I maximization, and verify our results with those of Secanell et al. [2007], and further extend our methodology to obtain optimal Pt distribution along CL width, by solving multi-zone partial differential equation-constrained optimization problem. Finally, we extend our GDL-CL model to three dimensions where we systematically tune the oxygen concentration and electrolyte phase potential boundaries to mimic the surrounding sub-component effect, and examine the role of third dimension.

Notation

A_o = Catalyst surface area per unit catalyst particle mass, cm^2g^{-1}

C = Concentration, $mol\ m^{-3}$

D_i = Diffusion coefficient of species i , cm^2s^{-1}

F = Faraday's constant, C/mol

h = Height, cm

H = Henry's constant, dimensionless

i_o = Exchange current density, $A\ cm^{-2}$

I = Current density, $A\ cm^{-2}$

j = Volumetric current density, $A\ cm^{-3}$

L = Width, cm

\mathcal{L} = Langevin function

m = Mass per unit area, $g\ cm^{-2}$

Pt/C = Platinum to carbon ratio (in mass)

r = Radius, cm

R = Gas constant, J/mol·K

T = Temperature, K

V = Voltage, V

x_i = Mole fraction of species i

Greek symbols

- α = $[H_2O]/[H^+]$ transported from anode to cathode
- δ = Electrolyte film thickness over agglomerate, *cm*
- ϵ = Volume fraction
- κ = Ratio of agglomerate film thickness and inner cluster radius
- $\hat{\mu}$ = Barrier parameter
- ϕ = Phase potential, *V*
- ρ = Density, kg/m^3
- σ = Conductivity, S-m^{-1}
- ξ_L = Thiele modulus

Subscripts and superscripts

- agg = Agglomerate
- C = Carbon
- eff = Effective value
- gc = Gas channel
- gdl = Gas diffusion layer
- L = Lower bound
- m = Electrolyte phase
- Pt = Platinum
- ref = Reference value
- s = Solid phase
- tot = Total

T = Tafel

U = Upper bound

v = Void phase

* = Optimal value

0 = Value at the inlet conditions

Chapter 4

Sensitivity of PEFC Models with Cathode Layer Micro - Structures

4.1 Introduction

As discussed in Jain et al. [2008b] sluggish oxidation reduction reaction in cathode catalyst layer (CL) is the major source of performance losses in an operating PEFC. These losses originate from poor reaction and transport rates of various reacting species (oxygen, proton, and electron), which in turn depend on the composition, structure/morphology, and catalytic material within the CL. Systematic modeling and optimization studies for examining the effect of composition, structure, and different catalyst materials on PEFC performance are required to reduce the tremendous number of expensive experimental trial and error cases, for providing design criteria for high performance CL.

A CL comprises of three phases, (*i*) the void space for oxygen/water transport, (*ii*) the electrolyte phase for proton transport, and (*iii*) the electro-

catalyst/solid phase for electron transport. These transport phenomena compete among each other depending on the composition of the three phases & the CL morphology, and the electrochemical reaction occurs at the intersection of these phases, termed as the triple phase boundary (TPB). The state-of-the-art macroscopic CL model in literature, the spherical agglomerate model [Sun et al., 2005], is commonly employed to examine the effect of void, electrolyte, and solid phase compositions on PEFC performance, as well as for optimization [Secanell et al., 2007]. However, such a description does not account for the structural effects on transport and reaction processes. Wang and co-workers [Mukherjee and Wang, 2006, 2007, Wang et al., 2006a,b, 2007a], via direct numerical simulation techniques, have incorporated mesoscopic pore-scale description of species and charge transport for randomized or ordered CL structures. Their detailed analysis however, is unsuitable for rigorous optimization studies.

In our study, we introduce the structural information through non-homogeneity (mesoscopic) within the CL agglomerate model (macroscopic), by examining shapes of agglomerate particles (Fig. 4.1) such as plate-like, cylindrical, and spherical as well as spherical shell on the PEFC performance. The plate-like, cylindrical, and spherical agglomerate models correspond with 1-D (uniformity along $y - z$ plane), 2-D (uniformity along z -axis), and 3-D CL models. We expect both the intra-particle (within an agglomerate) as well as inter-particle (between the agglomerates) transport processes to substantially differ due to this dimensionality factor.

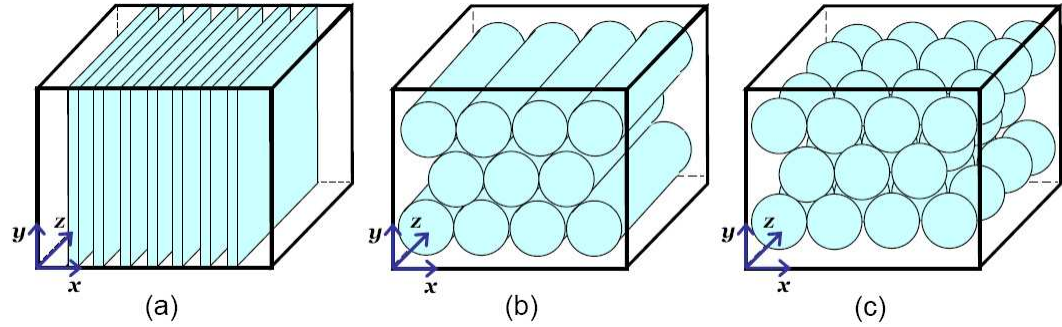


Figure 4.1: CL structures with (a) plate-like (1-D), (b) cylindrical (2-D), and (c) spherical (3-D) agglomerates.

In addition, we examine the effect of agglomerate sizes by generating self-similar CL structures, with fixed CL composition but different number and size of agglomerates (Fig. 4.2).

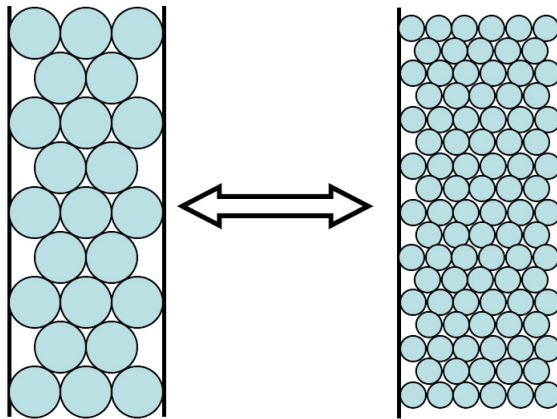


Figure 4.2: Self-similar CL structures with different-sized agglomerates.

This analysis is further extended to examine polydisperse systems, *i.e.*, systems with mixture of various particle sizes. Furthermore, we relax the commonly employed assumption, in both microscopic and macroscopic CL descriptions, of uniformly available TPBs for electrochemical reaction. We introduce the single and multi-zone spherical shell agglomerates with non-uniform reaction rates for this purpose.

Our goal, through sensitivity studies of simulation and optimization results for different CL morphologies, is to construct a basis for realistic CL structures, described through macroscopic models. Furthermore, we extend the prediction capabilities of the agglomerate CL model, and also examine criteria for improved CL performance via structural information.

4.2 Effect of agglomerate shapes

Here, we examine the shape effect of agglomerate particles on PEFC performance. We specifically examine two distinct features, *i.e.*, agglomerate effectiveness factors (resulting from intra-particle transport and electrochemical reaction) as well as effective transport properties (resulting from inter-particle transport), separately. The inter-particle transport, especially important to overall systems study, is briefly investigated here and is examined further in Chapter 5.

4.2.1 Effectiveness factors

The effectiveness factor (η) for a porous catalyst particle represents the ratio of reactant consumption rates, when intra-particle diffusion limitation exists, to when there were no diffusion limitation and entire catalyst active area is available for reaction. The effectiveness factors for rectangular (plate-like), cylindrical, and spherical porous catalyst particles, which correspond to 1-, 2-, and 3-D CL models respectively, are [Aris, 1957]

$$\eta^{(d)}(\xi_L^{(d)}) = \frac{\mathcal{L}^{(d)}(\xi_L^{(d)} d)}{\xi_L^{(d)}} \quad (4.1)$$

where d is the shape parameter and $d = 1, 2,$ and 3 for plates, cylinders and spheres, respectively. Here, the functions $\mathcal{L}^{(1)}(x) = \tanh x$, $\mathcal{L}^{(2)}(x) = I_1(x)/I_0(x)$, and $\mathcal{L}^{(3)}(x) = \coth x - 1/x$, where $I_0(x)$ and $I_1(x)$ denote the modified Bessel functions of zeroth and first order, respectively. $\xi_L^{(d)}$ is the Thiele's modulus given by

$$\xi_L^{(d)} = \left(\frac{v}{s}\right)^{(d)} \sqrt{\frac{k_c}{D_m^{eff}}} \text{ for } d = 1, 2, 3 \quad (4.2)$$

where $(v/s)^{(d)}$ is the inverse of specific area of a plate-like, cylindrical and spherical particle. In typical agglomerate CL models, D_m^{eff} is the effective diffusion coefficient of oxygen in the electrolyte phase, and k_c is the electrochemical reaction rate constant which is related to the electrolyte (m) and solid (s) phase potentials (ϕ) [Secanell et al., 2007], as well as the standard Tafel current density, j^T [Jain et al., 2008b] through

$$k_c = A_o \frac{m_{Pt}}{L_{cl}} \frac{i_o^{ref}}{4F(1 - \epsilon_v^{cl})C_{O_2}^{ref}} \exp\left(\frac{\gamma F}{RT}(\phi_m - \phi_s)\right) = j^T \left(\frac{H_{O_2,m}}{4F(1 - \epsilon_v^{cl})P_{tot}x_{O_2}}\right) \quad (4.3)$$

It is noted that for agglomerate CL models, the volumetric current density of generation, j , is modified from j^T via $\xi_L^{(d)}$ and functions $\mathcal{L}^{(d)}$, to include intra-particle (within agglomerate) transport phenomena. The parameters cited here can be found in Jain et al. [2008b]. $\xi_L^{(d)}$ is recast into the following form,

$$\xi_L^{(d)} = \left(\frac{v}{s}\right)^{(d)} \sqrt{\frac{H_{O_2,m}}{4(1 - \epsilon_v^{cl})FP_{tot}D_m^{eff}}} \sqrt{\frac{j^T}{x_{O_2}}} \quad (4.4)$$

In this study, we employ Eqs. (4.3)&(4.4), along with the model equations presented in Jain et al. [2008b] to examine the effect of different agglomerate shapes on fuel cell performance by calculating effectiveness factors.

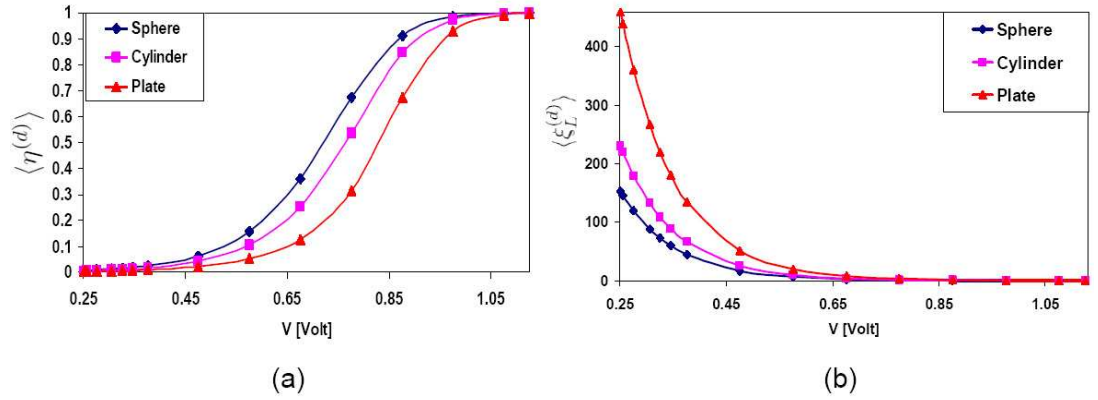


Figure 4.3: (a) $\langle \eta^{(d)} \rangle$, and (b) $\langle \xi_L^{(d)} \rangle$ curves for spherical, cylindrical, and plate-like shaped agglomerate particles.

As shown in Fig. 4.3(a), the space averaged effectiveness factor, $\langle \eta^{(d)} \rangle$ (where, $\langle X \rangle = \frac{1}{A} \iint X dA$ for any observable quantity X), exhibits an S-curve behavior with cell voltage of operation. At low voltage (V (Volt) < 0.4), which corresponds to high current density as shown in Fig. 4.4, the averaged Thiele's modulus, $\langle \xi_L^{(d)} \rangle$ (Fig. 4.3b), is very large as the reaction rate becomes much faster than the intra-particle mass transfer rate, and a very low $\langle \eta^{(d)} \rangle$ is obtained. At medium voltage values ($0.4 < V$ (Volt) < 1), corresponding to medium current density values, $\langle \eta^{(d)} \rangle$ increases and there is a significantly different response for the three different shape structures. The sphere pos-

sesses the lowest $\langle \xi_L^{(d)} \rangle$ value or the lowest diffusion limitations compared to the cylinder or the plate structures, keeping the other operating conditions same, and exhibits the best performance. At high voltages (V (Volt) > 1.0), $\langle \xi_L^{(d)} \rangle$ is low, and $\langle \eta^{(d)} \rangle$ approaches to 1.0 for all three different shapes. This intra-particle transport resistance effect for different shaped structures on the overall I-V characteristic curves is shown in Fig. 4.4.

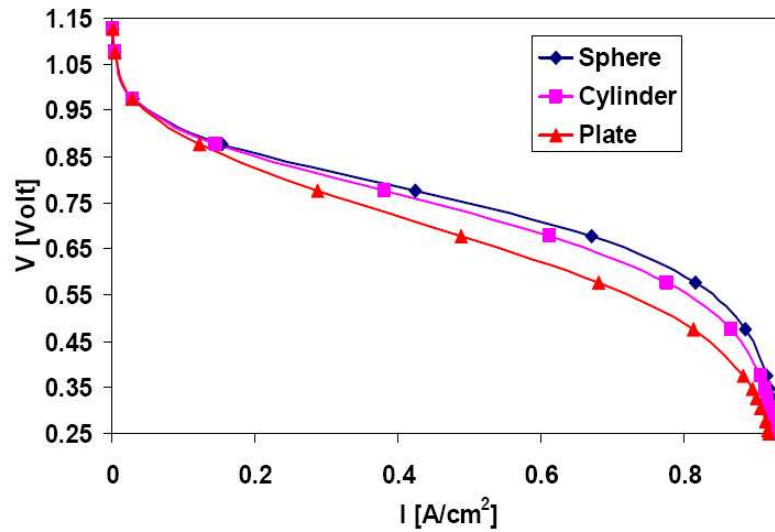


Figure 4.4: I-V characteristics curves for spherical, cylindrical, and plate-like agglomerate particle shapes.

The cathode CL is a region comprising competing transport phenomena amongst various reacting species (proton, electron, and oxygen) which depend on the corresponding phases (electrolyte, solid, and void (v)) holding these species. In addition, a higher Pt content (part of solid phase) enhances the electrochemical reaction rate. Due to coupled interplay between these phenomena affecting the overall PEFC performance, systematic optimization studies have recently gained special attention by Song et al. [2005], Mukherjee and

Wang [2006], Secanell et al. [2007], Jain et al. [2008b].

We examined the sensitivity on the optimization results via different shape effectiveness factors. Table 4.1 compares the ‘base’ (simulation results) and ‘optimized’ (results for maximized I , I^* *w.r.t.* four degrees of freedom: total Pt loading m_{Pt} , Pt to carbon ratio Pt/C , volume fraction of electrolyte in an agglomerate ϵ_{agg} , and gas diffusion layer (GDL) void volume fraction ϵ_v^{gdl}) cases. The ‘% E’ column represents the percentage of current density enhancement from the base to the optimal cases. The current density is enhanced most for the sphere case, and least for the plate case. However, it is interesting to note that the location of the optimal point $(m_{Pt}^*, (Pt/C)^*, \epsilon_{agg}^*, \epsilon_v^{gdl*})$ remains nearly the same for all three different cases.

Table 4.1: Optimization results for spherical, cylindrical, and plate-like agglomerate particle shapes.

		$I(A/cm^2)$	% E	$m_{Pt}^* (mg/cm^2)$	$(Pt/C)^*$	ϵ_{agg}^*	ϵ_v^{gdl*}
Sphere	Base	0.673	36.8	0.400	0.280	0.50	0.50
	Optimized	0.921		0.534	0.467	0.63	0.78
Cylinder	Base	0.612	33.7	0.400	0.280	0.50	0.50
	Optimized	0.818		0.515	0.467	0.65	0.79
Plate	Base	0.488	26.2	0.400	0.280	0.50	0.50
	Optimized	0.616		0.509	0.467	0.67	0.79

4.2.2 Transport properties

The effective transport properties, $\Gamma_p^{eff,(d)}$ ($d = 1, 2, 3$), within phase p ($p = v$ for void, m for electrolyte, and s for solid), are a function of the volume

fraction ϵ_p , of phase p , as

$$\Gamma_p^{eff,(d)} = \Gamma_{p,0} f^{(d)}(\epsilon_p) \text{ for } d = 1, 2, 3 \text{ and } p \in \{v, m, s\} \quad (4.5)$$

where, $\Gamma_{p,0}$ are the transport properties for $\epsilon_p = 1$. The purpose of this section is to demonstrate the sensitivity of PEFC performance to interparticle transport processes (species diffusion and charge conduction) via various effective transport models. As an example, out of many empirical correlations available, we choose the following functional forms $f^{(d)}(\epsilon_p)$ for long cylinders ($d = 2$) and spheres ($d = 3$).

$$f^{(2)}(\epsilon_p) = \frac{\epsilon_p}{(2 - \epsilon_p)} \text{ for } p \in \{v, m, s\} \quad (4.6)$$

$$f^{(3)}(\epsilon_p) = \epsilon_p^{1.5} \text{ for } p \in \{v, m, s\} \quad (4.7)$$

Equations (4.6) and (4.7) are Rayleigh's [Bird et al., 1960] and Bruggemann's [Secanell et al., 2007] relations, respectively. It is noted that results presented in Table 4.1 and Fig. 4.4 are based on Bruggemann's relation.

Figure 4.5 compares the $I - V$ simulation responses for the agglomerate CL model for the above two effective transport models. It is observed that, for very low current densities ($\ll 0.1 \text{ A/cm}^2$), these two models generate similar cell voltages. For intermediate current densities (between 0.1 to 0.5 A/cm^2), the ordinates are separated by nearly a constant value of 0.04 A/cm^2 . At high current densities ($> 0.5 \text{ A/cm}^2$), where the external mass transport resistances

become dominant, Bruggemann’s model predicts significantly larger voltages over the Rayleigh’s model.

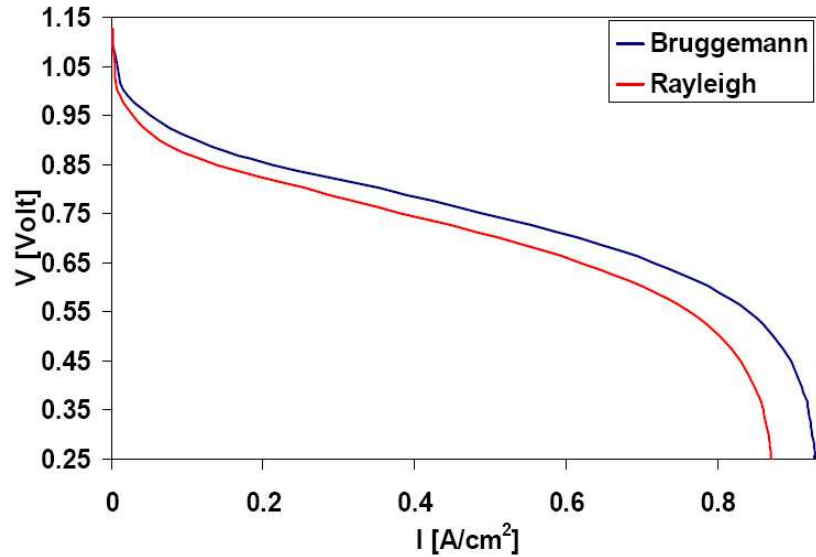


Figure 4.5: $I - V$ curves for different transport models.

Table 4.2 shows the optimization results for these cases. The sphere (Bruggemann) results here correspond with results in Table 4.1. We again observe a significant difference in degree of enhancement in current density between the base and optimized values of I between the sphere (Bruggemann) and cylinder (Rayleigh) models. Unlike the results in Table 4.1, the location of the optimal point also differs for the sphere and cylinder shape structures. A decrease in the value of m_{Pt}^* (which enhances electrochemical reaction rate) from base to the optimized case for the cylinder model may seem counter-intuitive, however, it is noted that a decrease in Pt content also enhances the H^+ and O_2 transport processes via increase in electrolyte and void phase hold-ups.

Table 4.2: Optimization results for two different transport models.

		$I^*(A/cm^2)$	$m_{Pt}^* (mg/cm^2)$	Pt/C^*	ϵ_{agg}^*	ϵ_v^{gdl*}
Sphere	Base	0.673	0.400	0.280	0.50	0.50
(Bruggemann)	Optimized	0.921	0.534	0.467	0.63	0.78
Cylinder	Base	0.570	0.400	0.280	0.50	0.50
(Rayleigh)	Optimized	0.694	0.327	0.302	0.58	0.82

4.3 Effect of agglomerate size

We examine the agglomerate size effect via generating ‘self-similar’ CL structures, by varying number of particles, $n = n_0 2^m$, ($m = 0, 1, 2, \dots; n_0 = 1.696 \times 10^{11}$). The particle size (r_{agg}) and the PEM film thickness (δ) surrounding the agglomerate particle is adjusted so as to keep the constant ratio of $\kappa_{agg} = \delta/r_{agg}$ which equals to 0.08. All the other physical parameters of the system are fixed: amounts of Pt, carbon, and PEM materials via phase volume fractions ($\epsilon_s^{cl} = 0.355$, $\epsilon_m^{cl} = 0.540$, and $\epsilon_v^{cl} = 0.105$), $m_{Pt} = 0.0004g/cm^2$, and $Pt/C = 0.28$, , as well as the GDL parameters via $\epsilon_s^{gdl} = 0.5$ and $\epsilon_v^{cl} = 0.5$.

A decrease in particle size leads to increase in overall oxygen consumption rate within the agglomerate due to several reasons. As observed from Figs. 4.6(a)&(b), Thiele’s modulus decreases with particle size (Eq. (4.2)) and the effectiveness improves significantly. The effective reaction rate, which is the product of reaction rate without intra-agglomerate mass transfer limitations and agglomerate effectiveness, $\langle \eta \rangle \langle j^T \rangle$ (we assumed $\langle \eta j^T \rangle \sim \langle \eta \rangle \langle j^T \rangle$) enhances as particle size decreases. Furthermore, as specific surface area of

agglomerate increases the oxygen dissolution rate into the PEM film encapsulating the agglomerate enhances. Also, reduction in δ enhances the film diffusion.

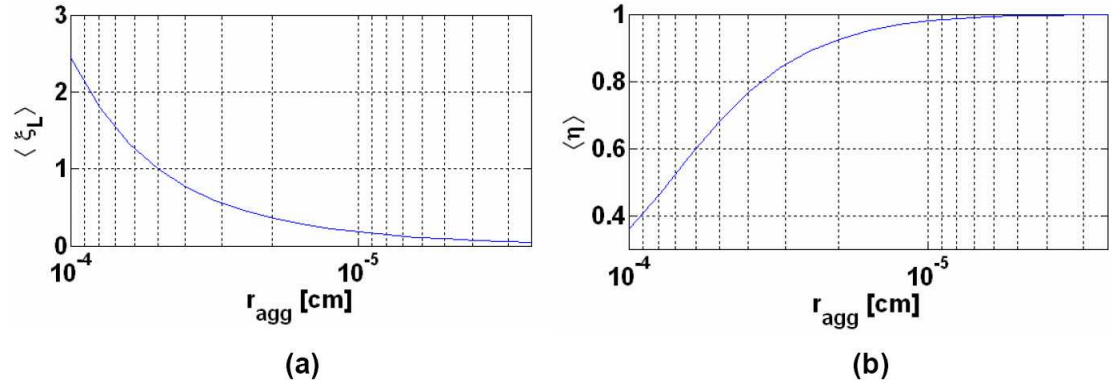


Figure 4.6: (a) Space averaged Thiele's modulus and (b) effectiveness factor for different agglomerate sizes

However, a higher oxygen consumption rate leads to a decrease in reactant driving force. Also, at higher current densities, the inter-phase charge transfer

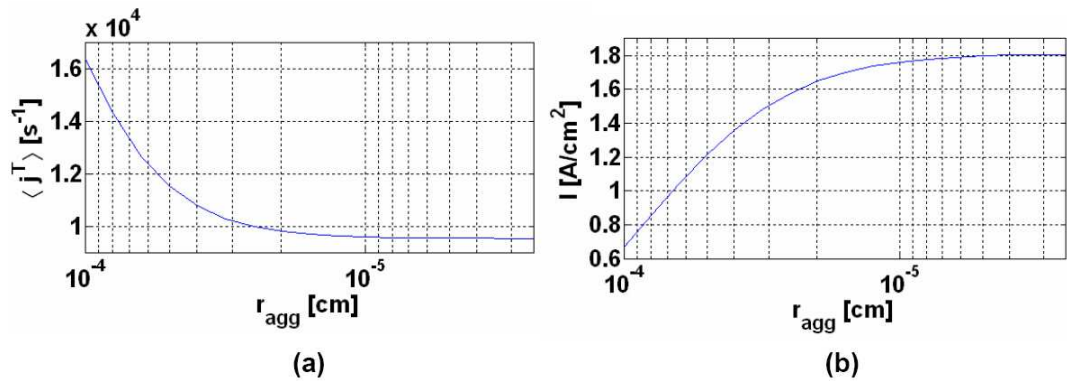


Figure 4.7: (a) Space averaged Tafel current density and (b) cell output current density

driving force ($\phi_m - \phi_s$) decreases leading to decrease in electrochemical reaction rate, represented by Tafel current density (Fig. 4.7a). As $n \rightarrow \infty$, the

current density reaches an asymptotic value of 1.8 A/cm^2 , almost a three-fold enhancement from the base value of 0.67 A/cm^2 . A ten-fold reduction in the original particle size produces current density within 2.5% at this asymptotic value.

4.3.1 Polydispersity

Here we examine mixtures of various particle sizes (polydisperse systems) with given particle size distribution, which is more close to realistic scenarios.

The methodology employed here is based on finding a mean particle size describing the overall performance of the CL bed [Aris, 1957]. The CL bed is assumed to be homogenous, such that a sample from a random location within comprises of same volume fraction, v_i , occupied by the particles of i^{th} size, and $\sum_{i=1}^{NS} v_i = 1$, where NS is the number of available particle sizes.

To account for the polydispersity, $\xi_{L,i}$ for each particle size, $r_{agg,i}$, and the corresponding $\eta_i(\xi_{L,i})$ ($i = 1, \dots, NS$) are calculated from Eqs. (4.3) & (4.2). The overall bed effectiveness ($\bar{\eta}$) is:

$$\bar{\eta} = \sum_{i=1}^{NS} \eta_i(\xi_{L,i}) v_i \quad (4.8)$$

An equivalent Thiele's modulus corresponding to $\bar{\eta}$ is found via Eq. (4.3), and the equivalent particle size \bar{r}_{agg} via Eq. (4.2). This r_{agg} is then employed in the entire modeling equations [Jain et al., 2008b] for simulation and optimization.

To study the qualitative behavior of polydisperse systems we examined

a simple bi-modal particle size distribution; comprising 1 micron (termed as large) and 0.5 micron (small) particle sizes, with different blend ratios. The amounts of Pt, carbon, and PEM materials are again fixed via phase volume fractions, m_{Pt} , and Pt/C as described before. Figure 4.8 shows the I-V characteristics for a range of bed compositions between a bed with pure component of large and small particles. Here, f_s is the fraction of small sized particles in the bed.

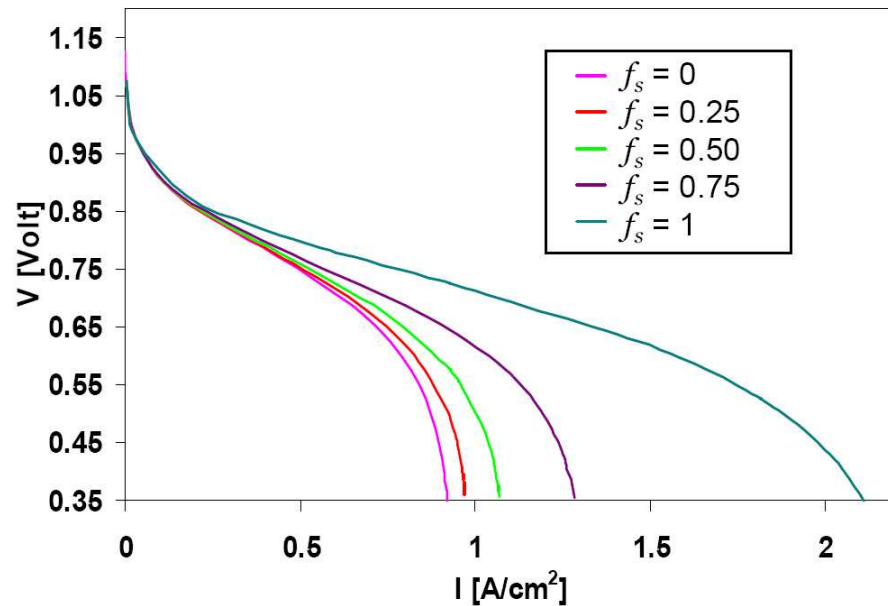


Figure 4.8: I-V characteristic curves for two component mixtures

The curves corresponding to $f_s = 0$ and $f_s = 1$ are consistent with Fig. 4.7(b). In I-V curves, various mixture compositions exhibit curves that lie in between two pure component systems, and performance improves as f_s increases.

The optimization results based on maximum current density are shown in Table 4.3, which illustrates the compensation amongst the competing mecha-

nisms of O_2 , H^+ , and e^- transports as well as electrochemical reaction. Similar

Table 4.3: Optimization results for mixture systems.

f_s	$I^*(A/cm^2)$	$m_{Pt}^* (mg/cm^2)$	$(Pt/C)^*$	ϵ_{agg}^*	ϵ_v^{gdl*}
0	0.921	0.534	0.467	0.630	0.78
0.25	0.945	0.546	0.467	0.628	0.79
0.50	0.985	0.564	0.467	0.620	0.79
0.75	1.076	0.598	0.467	0.605	0.80
1	1.467	0.655	0.467	0.595	0.80

to the I-V curves in Fig. 4.8, I^* increases as f_s increases. The optimal Pt amount increases (which reduces the electrolyte and void phase hold-ups) f_s increases. This may be explained by the fact that O_2 transport limitations are lowered via enhanced specific surface area, reduced δ , and improved accessibility to Pt catalyst within an agglomerate for smaller sized systems. Therefore, optimal location shifts towards improving electrochemical reaction rate via higher Pt amount. Further, the optimal electrolyte amount within individual agglomerate decreases as the Pt content increases.

Figure 4.9 illustrates the variation of current density for medium (0.676 V) to low (0.396 V) voltages of operation, as well as I^* at 0.676 V for various compositions of the system. Interestingly, I or I^* follows a third degree polynomial relationship with f_s for bi-modal particle size distribution systems. Although, our demonstration is for a simple bi-modal distribution, our methodology can be easily extended to general, continuous distributions.

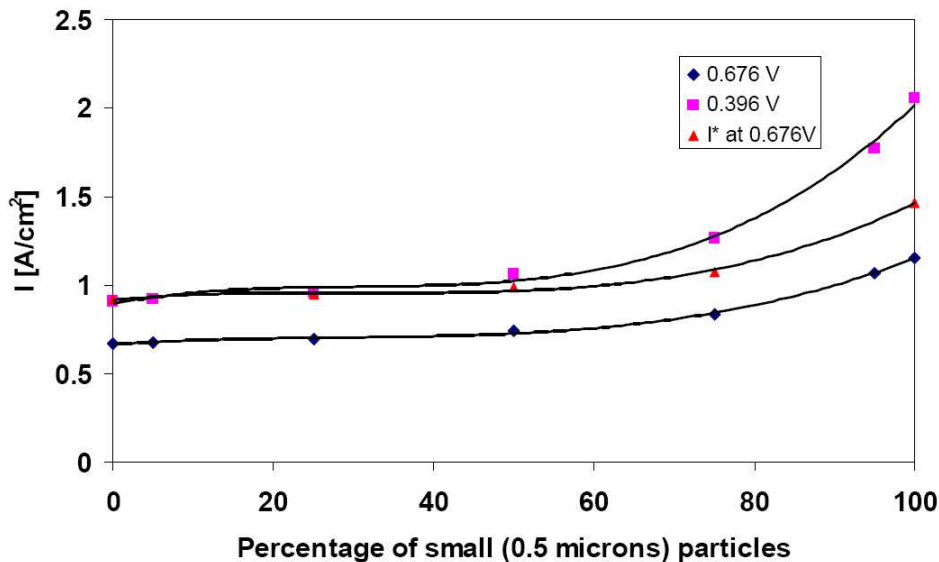


Figure 4.9: Current density for two component mixtures

4.4 Spherical shell agglomerate

In contrast to plate-like, cylindrical, and solid spherical shapes, we introduce the spherical shell agglomerate model. We focus on two design cases of agglomerate particles: Case I, where the catalyst material inside a solid sphere of radius $R_1 = r_{agg}$ is concentrated within the shell between the radii R_1 and R_2 (Fig. 4.10), and Case II, where solid spheres exist however, material within the outer shell and the inner sphere are different. We examine these shell models by deriving the agglomerate effectiveness factors. These models introduce extra flexibility of tuning diffusion and reaction inside an agglomerate sphere.

Case I

An expression for effectiveness factor for a hollow spherical shell was reported by Aris [1957], obtained by modifying effectiveness for a solid sphere, via

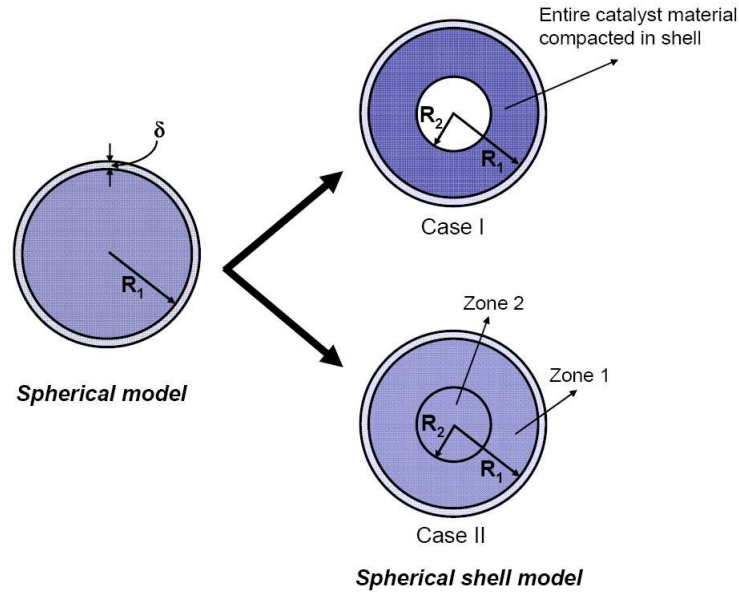


Figure 4.10: A schematic of Cases I & II spherical shell agglomerates.

empirical shape factor, v/s for a shell into the generalized Thiele's modulus equation (Eq. (4.2)). In our study, instead of heuristic argument by Aris [1957], we derive the effectiveness factor for a spherical shell from first principles. Figure 4.11 shows a two-zone spherical agglomerate with zone 1 ($R_2 < r < R_1$) concentration C_{A1} , and zone 2 ($r < R_2$) concentration C_{A2} for a species 'A'. A

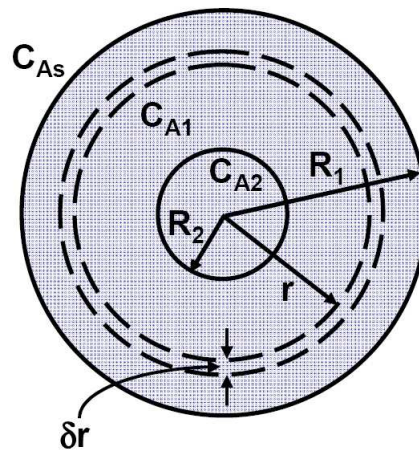


Figure 4.11: A schematic for derivation for effectiveness factor in Cases I & II.

differential mass balance for A with first order kinetics leads to the following

equations in zones 1 & 2:

$$D_i \frac{1}{r^2} \frac{d}{dr} \left(r^2 \frac{dC_{Ai}}{dr} \right) = (k_i a) C_{Ai} \text{ for } i = 1, 2 \quad (4.9)$$

where, a is the specific surface area available for reaction, and k_i & D_i denote the electrochemical reaction rate constants and diffusion coefficients for i^{th} zone ($i = 1, 2$), respectively. Now, for the case of hollow spherical shell since there is no catalyst material in zone 2, we set C_{A2} to bulk concentration C_{AS} . Also, substituting $C_{A1} = f/r$ [Bird et al., 1960], the general solution for C_{A1} in Eq. (4.9) can be easily obtained as

$$C_{A1} = \frac{C_{11}}{r} \cosh \lambda r + \frac{C_{21}}{r} \sinh \lambda r \quad (4.10)$$

where, $\lambda = \sqrt{k_1 a / D_1}$, and C_{11} & C_{21} are constants determined via the following boundary conditions (B.C.s):

$$C_{A1} = C_{AS} \text{ for } r = R_1 \quad (4.11)$$

$$k_0 \sigma (C_{A1} - C_{AS}) = \left(D \frac{dC_{A1}}{dr} \right)_{r=R_2} \quad (4.12)$$

where, σ is the volume per unit surface area, and k_0 the mass transfer coefficient. Equation (4.12) is a general Robin B.C., a combination of Dirichlet and Neumann B.C.s (covering both zero and non-zero flux cases), at radius R_2 . The ratio of mass transfer resistances inside of and at the surface, $k_0 / D\sigma$, becomes dimensionless and is defined as the Biot number (Bi). The effectiveness factor η , the ratio of molar flux at the surface $r = R_1$ to the molar rate

of conversion when no diffusion limitations exist, is given as:

$$\eta = \frac{4\pi R_1^2 (-D_1 dC_{A1}/dr)_{r=R_1}}{\frac{4}{3}\pi R_1^3 (-k_1 a C_{AS}) (1 - (R_2/R_1)^3)} \quad (4.13)$$

On substituting for $(dC_{A1}/dr)_{r=R_1}$, calculated from Eqs. (4.10)-(4.12), we obtained the following expression for shell effectiveness, η :

$$\eta = \frac{\eta_1}{\eta_2}$$

where

$$\begin{aligned} \eta_1 &= 3 \left[\left(\lambda^2 R_1 R_2 - Bi \left(\frac{R_2}{R_1} \right) - 1 \right) (\tanh(\lambda R_1) - \tanh(\lambda R_2)) \right. \\ &\quad \left. - \lambda R_1 \left(1 + (Bi - 1) \left(\frac{R_2}{R_1} \right) \right) (1 - \tanh(\lambda R_1) \tanh(\lambda R_2)) \right. \\ &\quad \left. + Bi \left(\frac{R_2}{R_1} \right)^2 (\lambda R_1 - 1) (\tanh(\lambda R_1) - 1) \right] \\ \eta_2 &= (\lambda R_1)^2 \left(1 - \left(\frac{R_2}{R_1} \right)^3 \right) \left[\lambda R_2 + \left(1 + Bi \left(\frac{R_2}{R_1} \right) \right) \tanh(\lambda R_1) \right. \\ &\quad \left. + \tanh(\lambda R_2) \left(1 + Bi \left(\frac{R_2}{R_1} \right) + \lambda R_2 \tanh(\lambda R_1) \right) \right] \end{aligned} \quad (4.14)$$

Using Eq. (4.14) we first examined η with shell thickness for a given outer radius, R_1 . Figure 4.12 shows the variation of ratio of shell effectiveness to a sphere with the ratio R_2/R_1 , for several different Bi . In these curves, Thiele's modulus for the shell was set to 1. As R_2 increases, the shell thickness decreases and its effectiveness improves over a sphere, as same amount of catalyst material is available for the reaction with the shell, and mass transport for the region $r < R_2$ is not required. In Fig. 4.12, the curve for $Bi = 0$, corresponding to a zero radial diffusive flux at $r = R_2$, shows a good agreement with the expression reported for a spherical shell in Aris [1957].

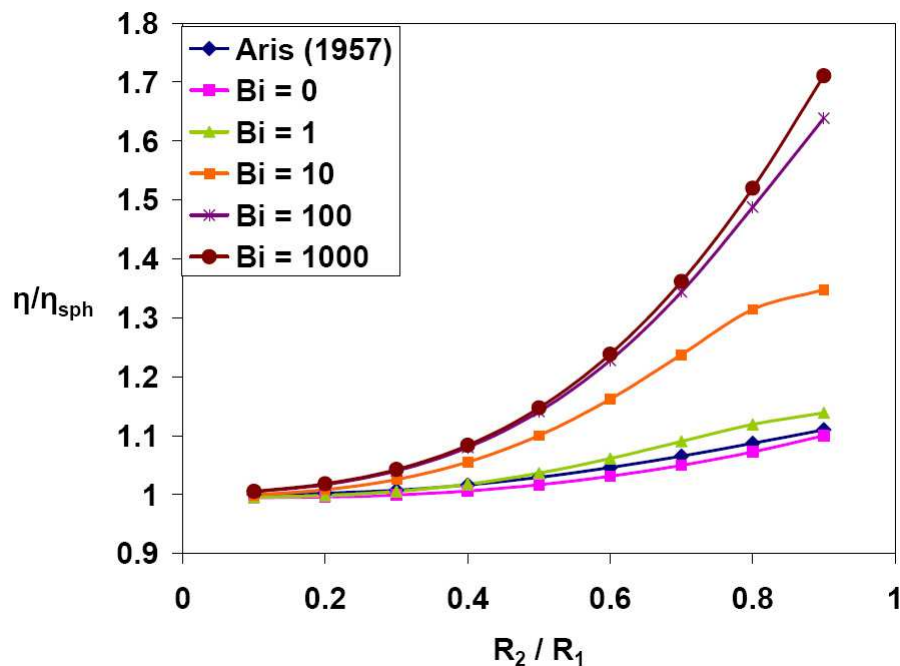


Figure 4.12: Effectiveness of spherical shell with its thickness for different Bi . η and η_{sph} denote the effectiveness for a shell and sphere, respectively.

To illustrate the essence, we examined the effectiveness for $Bi = 0$ case only, in our CL-GDL modeling with optimization framework [Jain et al., 2008b]. Figure 4.13 shows the I-V curves for the pseudo homogenous, sphere agglomerate, and spherical shell agglomerate models. The pseudo homogenous model refers to a CL description where all three electrolyte, solid, and void phases are assumed to be homogeneously present for electrochemical reaction, without the presence of agglomerates. The film dissolution, film diffusion, as well as agglomerate inner cluster diffusion resistance are absent. As shown in Fig. 4.13, three kinds of models predict same cell performance for $I < 0.2$ A/cm^2 , however for medium to lower values of I where mass transfer losses become significant in fuel cell operation, the predictions vary significantly. Due to absence of any agglomerate resistance, the pseudo homogenous model

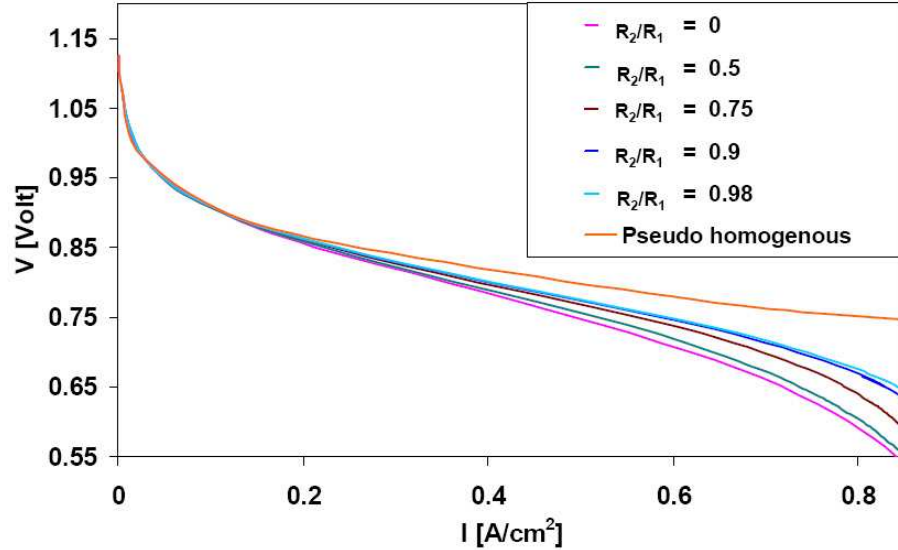


Figure 4.13: I-V characteristic curves for the pseudo homogenous, spherical shell agglomerate and sphere agglomerate models.

exhibits the highest performance, whereas the spherical shell model shows a departing behavior from the sphere model as the shell becomes thinner. For the limiting case of an extremely thin shell ($R_2/R_1 = 0.98$) we observe, the I-V curve lies approximately between the sphere agglomerate and pseudo homogenous model predictions. Hence, the spherical shell agglomerate model provides extra degrees of freedom, including shell thickness and Bi (although not fully examined), for predictions between the standard pseudo homogenous and spherical agglomerate CL models. It is also noted that Fig. 4.13 depends on the agglomerate particle size, which was discussed before.

In Table 4.4 we present the optimization results for maximization of I *w.r.t.* m_{Pt} , Pt/C , ϵ_{agg} , and ϵ_v^{gd} for spherical shells of various thicknesses. It is noted that the degree of departure from the sphere agglomerate model ($R_2/R_1 = 0$), in the values of optimal current density I^* becomes significantly larger the

base current density I as shell thickness decreases. Also, m_{Pt}^* increases and reaches its upper bound (1.250 mg/cm^2) as well as ϵ_{agg}^* decreases significantly as the shell thickness decreases.

Table 4.4: Optimization results for different shell thicknesses for Case I.

R_2/R_1	$I(A/cm^2)$	$I^*(A/cm^2)$	$m_{Pt}^* (mg/cm^2)$	Pt/C^*	ϵ_{agg}^*	ϵ_v^{gdl*}
0.00	0.154	0.192	1.126	0.467	0.343	0.740
0.50	0.158	0.200	1.162	0.467	0.321	0.740
0.75	0.162	0.216	1.246	0.467	0.271	0.737
0.90	0.165	0.226	1.250	0.454	0.229	0.835

Case II

Here, we examine the spherical agglomerate comprising of two zones, the inner sphere $r < R_2$, and the shell between radii R_1 & R_2 , where different rates of electrochemical reaction and intra-particle transport take place. The motivation for this study stems from the fact, that the probability of finding the electrolyte, solid, and void phases together (or TPB) may not be distributed uniformly, which requires additional parameters to incorporate the role of TPB in continuum level (meso-scale). To the best of our knowledge, none of the continuum-based agglomerate models in literature account for non-uniformity in the distribution of TPB. We capture, via a two-zone spherical agglomerate model, the essence of TPB non-uniformity within an agglomerate, by setting different reaction and/or transport rates in the two zones. To incorporate TPB non-uniformity accurately, it is desirable to extend our analysis to an N-zone case.

We derive the effectiveness factor for such a two-zone agglomerate, shown in Fig. 4.11. The governing species mass balance equations, Eq. (4.9), for the two-zone case, have the following solutions:

$$C_{Ai} = \frac{C_{1i}}{r} \cosh \lambda_i r + \frac{C_{2i}}{r} \sinh \lambda_i r \text{ for } i = 1, 2 \quad (4.15)$$

where, $\lambda_i = \sqrt{k_i a / D_i}$, C_{1i} and C_{2i} are constants determined via the following B.C.s:

Outermost boundary:

$$C_{A1} = C_{AS} \text{ for } r = R_1 \quad (4.16)$$

Zero concentration gradient at $r = 0$:

$$\left(\frac{dC_{A2}}{dr} \right)_{r=0} = 0 \quad (4.17)$$

Mass and flux continuity at interface R_2 becomes:

$$(C_{A1})_{r=R_2^+} = (C_{A2})_{r=R_2^-} \quad (4.18)$$

$$D_1 \left(\frac{dC_{A1}}{dr} \right)_{r=R_2^+} = D_2 \left(\frac{dC_{A2}}{dr} \right)_{r=R_2^-} \quad (4.19)$$

The effectiveness factor η , is modified from Eq. (4.13) via a factor of $(1 - (R_2/R_1)^3)$ as:

$$\eta = \frac{4\pi R_1^2 (-D_1 dC_{A1}/dr)_{r=R_1}}{\frac{4}{3}\pi R_1^3 (-k_1 a C_{AS})} \quad (4.20)$$

We implemented equations for constants C_{1i} and C_{2i} obtained from above B.C.s along with Eq. (4.20) in the simultaneous solution framework presented in Jain et al. [2008b] to obtain η . Figure 4.14 shows the ratio of two-zone spher-

ical agglomerate model to the spherical agglomerate model (η/η_{sph}) with varying ratio (R_2/R_1). The case $k_1/k_2 = 1$, with uniform reaction rate throughout

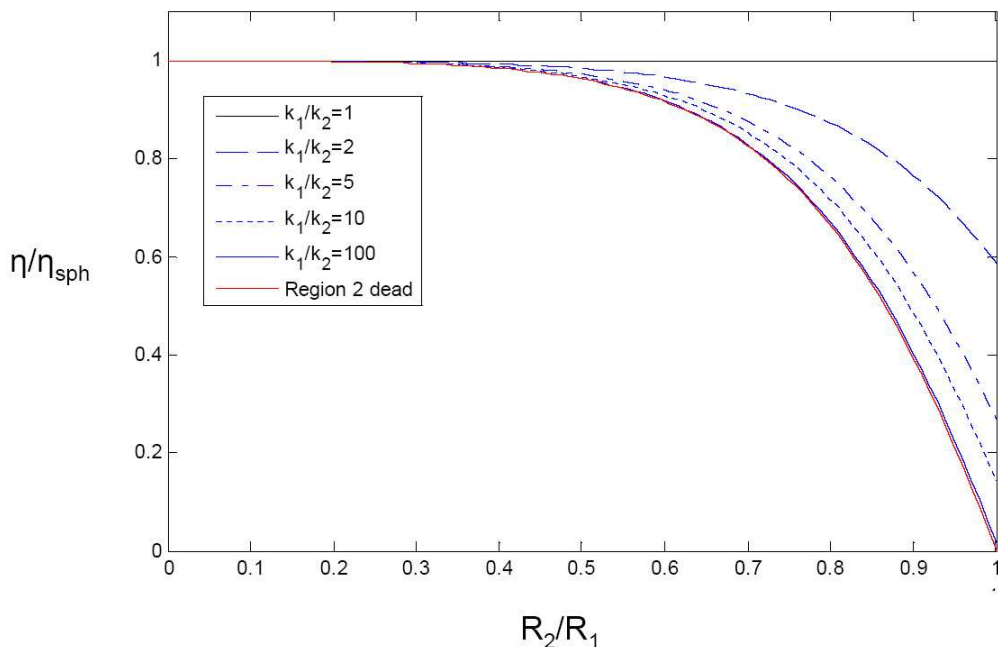


Figure 4.14: Effectiveness of two-zone agglomerate for varying thickness of zone 2.

the agglomerate corresponds to the case of single zone sphere discussed earlier. To introduce the non-uniformity in TPB distribution, we examined the effectiveness for reduced electrochemical reaction rates k_2 within zone 2. In Fig. 4.14, for $k_1/k_2 > 1$, the effectiveness factor decreases, as R_2 increases. The effectiveness factor for a two-zone agglomerate follows very closely with a spherical agglomerate effectiveness (less than 2% drop) for $R_2/R_1 < 0.3$, indicating that inside core of spherical agglomerate ($r < 0.3R_1$) remains unused in the electrochemical reaction. However, for higher R_2 values, the effectiveness drops sharply as k_2 is reduced, and the effectiveness for the case $k_1/k_2 = 100$ follows very closely with the case when the inner zone is dead or

has no electrochemical reaction taking place. However, effectiveness for a two-zone agglomerate reduces by less 20% *w.r.t.* sphere, even for a large fraction of zero-reaction or dead zone (*i.e.*, $R_2/R_1 = 0.7$), indicating that majority of electrochemical reaction occurs within a thin outer shell region.

Figure 4.15 shows the variation in current density for a voltage of 0.676 Volt with R_2/R_1 for different k_1/k_2 ratios. As expected, the performance decreases

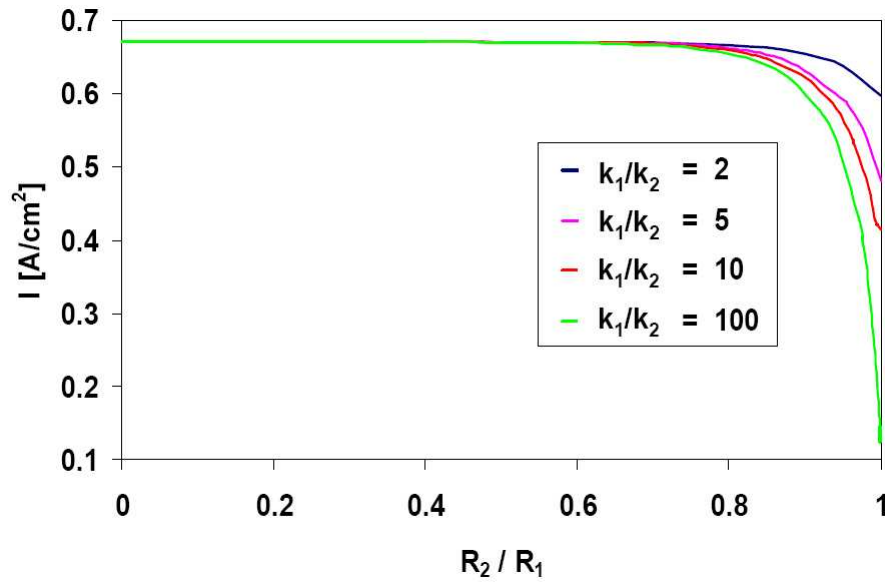


Figure 4.15: Current density for different k_1/k_2 ratios for two-zone agglomerate system

as k_2 reduces. However, it is interesting to note that a significant effect of reduction in k_2 to I begins to occur only when zone 2 radius $R_2 > 0.7R_1$.

Figure 4.16 illustrates the I-V characteristics for different R_2/R_1 , generated for a dead zone 2. The performance of the fuel cell decreases as the dead zone size increases. For high current densities however, it is observed that, the curves for different R_2/R_1 cases merge with the spherical agglomerate model case. This may be explained by the fact that for high current densities

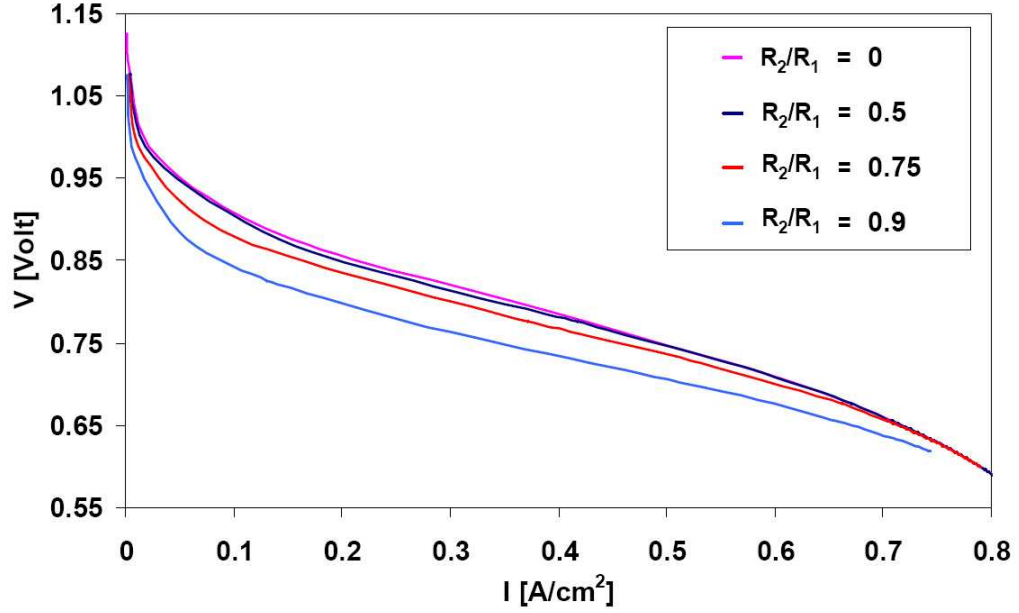


Figure 4.16: I-V characteristics curves with different zone 2 thicknesses

of operation, when reaction rate is very high, the reactant O_2 is consumed rapidly within a very small outer shell region and further penetration inside is not required.

Table 4.5 shows the optimization results for maximizing I , where I^* decreases rapidly as shell thickness decreases. Similar to Table 4.4, m_{Pt}^* increases and reaches the upper bound of 1.25 mg/cm^2 whereas ϵ_{agg}^* decreases significantly with shell thickness.

Table 4.5: Optimization results for different shell thicknesses for Case II.

R_2/R_1	$I(A/cm^2)$	$I^*(A/cm^2)$	$m_{Pt}^*(mg/cm^2)$	Pt/C^*	ϵ_{agg}^*	ϵ_v^{gdl*}
0.00	0.154	0.192	1.126	0.467	0.343	0.740
0.50	0.142	0.183	1.175	0.467	0.317	0.740
0.75	0.106	0.149	1.250	0.457	0.253	0.725
0.90	0.056	0.092	1.250	0.423	0.166	0.728

4.5 Summary

In this Chapter, we performed sensitivity studies of cell performance for different CL structures through macroscopic models, suitable for system optimization. We examine the shape effect of agglomerate particles including plate-like, cylindrical, and spherical as well as spherical shell on the PEFC performance. Both the intra- and inter-particle transport processes substantially differ due to this shape factor, as indicated by both simulation and optimization results. In addition, we examine the effect of agglomerate sizes by generating self-similar CL structures, with fixed CL composition but different number and size of agglomerates, and extend to mixture of particle sizes. Furthermore, via the 2-zone shell agglomerate model, we introduce non-homogeneity in TPB distribution. Through these model sensitivity studies for different CL morphologies, we formulate a basis for realistic CL structures, described through macroscopic models.

Notation

- a = Specific surface area available for reaction, cm^{-1}
 A_o = Catalyst surface area per unit catalyst particle mass, cm^2g^{-1}
 Bi = Biot number
 C = Concentration, mol/cm^3
 d = Shape parameter
 D = Diffusion coefficient, cm^2s^{-1}
 f_s = Fraction of small size particles
 F = Faraday's constant, C/mol
 H_{O_2} = Henry's constant, $Pa\ cm^3mol^{-1}$
 i_0^{ref} = Reference current density, A/cm^{-2}
 I = Current density, A/cm^{-2}
 j^T = Tafel current density, A/cm^{-3}
 k_o = Mass transfer coefficient, m/s
 k_c = Electrochemical reaction rate constant, s^{-1}
 L = Length, cm
 m = Mass per unit area, mg/cm^2
 n = Number of particles
 N = Number of available particle sizes
 P_{tot} = Total pressure, Pa
 Pt/C = Platinum to carbon ratio
 r = Radius of particle, cm
 R = Universal gas constant, $J/K - mol$

R_1 = Outer radius, cm

R_2 = Inner radius, cm

s = Surface area, cm^2

T = Temperature, K

v = Volume, cm^3

v_i = Volume fraction of i^{th} size

x = Mole fraction

Greek Symbols

δ = Electrolyte film thickness, cm

ϵ = Volume fraction

η = Effectiveness factor

γ = Butler-Volmer kinetics factor

Γ_p = Transport property for phase p

κ = ratio of electrolyte film thickness and agglomerate radius

ξ_L = Thiele's modulus

ϕ = Phase potential, $Volt$

σ = volume per unit surface area, cm

Subscripts and Superscripts

<i>agg</i>	=	Agglomerate
<i>A</i>	=	Subscript for species A
<i>cl</i>	=	Catalyst layer
<i>d</i>	=	Shape parameter
<i>eff</i>	=	Effective value
<i>gdl</i>	=	Gas diffusion layer
<i>i</i>	=	Particle size index
<i>m</i>	=	Electrolyte phase
<i>O₂</i>	=	Oxygen
<i>p</i>	=	Phase
<i>ref</i>	=	Reference value
<i>s</i>	=	Solid phase
<i>S</i>	=	External surface
<i>v</i>	=	Void phase
0	=	Initial/base value
1	=	Zone 1 within agglomerate
2	=	Zone 2 within agglomerate
*	=	Optimal value

Chapter 5

Multi-scale Modeling and System Integration

5.1 Introduction

The goal of this work has been to develop multi-scale models in an optimization framework for energy systems, with PEFC as a benchmark example. This not only involves formulation as well as optimization at each multi-scale hierarchy, but also integration of sub-component models comprising of coupled multi-physical and multi-scale phenomena.

From this multi-scale modeling and integration perspective specifically, in setting-up the theme for this Chapter, we briefly highlight our progress in Chapters 2 to 4, and this Chapter in the matrix presented in Fig. 5.1. Each row here represents the different sub-components at each multi-scale hierarchical level, and each column represents each PEFC sub-component system. In Chapter 2, we focused on integration of multi-component systems, with continuum based models in an efficient optimization framework. We incorpo-

	GC	GDL	CL	PEM
Phenomenological			Ch. 2	
Continuum	Ch. 2	Chs. 2,3,4	Ch. 3	Ch. 2
Mesoscopic	N.A.	Ch. 5	Ch. 4	Ch. 5
Atomistic/ molecular	N.A.	N.A.		

Figure 5.1: Our PEFC research milestone presented in this work.

rated rigorous computational fluid dynamics (CFD) descriptive for GC, GDL, and PEM sub-components, whereas CL was phenomenologically described as a thin interface. Although physically simplistic, introduction of CFD models in an integrated optimization framework was a key step towards holistic energy system models. In Chapter 3, we replaced the phenomenological description of CL with a continuum/mesoscopic description which is closer to realistic physical situation and provides control over actual physical parameters (*e.g.*, Pt loading). We also introduced non-homogeneity in Pt distribution. The CL was integrated with a continuum based GDL. In Chapter 4, we expanded our continuum CL description to include as much micro-structural information as possible within our existing optimization framework, *e.g.*, through introduction of polydisperse systems and non-uniform distribution of triple phase boundary within CL. The coupled intra- and inter-particle transport processes were separately examined for different CL structures. We also examined the relationship between self-similar CL structures via variation in particle number

and size, conserving the other physical properties.

In this chapter, we explore the mesoscopic/molecular level descriptions within the PEM as well as GDL, by gearing towards actual particle-level from field-level descriptions. Although complete multi-scale descriptions for each sub-component are yet to be examined, in practice “partial multi-scale” is desirable for system optimization, for which we propose a novel reduced order methodology (ROM) suitable for system integration.

5.2 Mesoscale methods for estimating effective transport in non-homogenous media

In this section, we examine mesoscopic descriptions for non-homogenous porous media structures with application to the PEFC membrane electrode assembly (MEA), especially within the GDL subcomponent. The key technological issues in PEFC technology stem from the performance inefficiencies within its MEA comprising of GDL, CL, and PEM, which are heterogeneous porous material sub-components, and through which heat & mass transport processes occur with or without electrochemical reaction. For overcoming the performance limitations within MEA, a detailed understanding of the transport processes is required. Especially, within a cathode GDL, liquid water transport results in flooding phenomena leading to a key performance limitation, called the mass transport overpotential, due to the blockage of pores hindering the oxygen transport to the active reaction sites in the CL [Wang, 2004]. The problem

boils down to designing the GDL structure which enables efficient removal of water as well as oxygen transport. Traditional non-homogeneous media theories [Maxwell, 1881, Bruggemann, 1935, Wang et al., 2006c] estimate the effective molecular transport coefficients (without fluid flow information) through averaged phase hold-up and/or tortuosity parameters, and therefore, are unable to account for the microscopic structural information within the media.

5.2.1 Lattice Boltzmann method

We introduce the lattice Boltzmann methods (LBMs) to incorporate mesoscopic structural information by estimating effective transport properties in a non-homogeneous medium. Unlike conventional CFD methods which discretize the macroscopic equations, LBM constructs simplified kinetic models incorporating the essential physics of microscopic processes so that the averaged properties describe the desired macroscopic properties. The advantages of LBM are clear physical pictures, geometric flexibility, an inherently transient nature, hybridization with other physical phenomena, and fully parallel algorithms, which makes LBM an attractive tool for multi-phase, multi-scale simulation for PEFC devices [Kim et al., 2005a,b].

Here, as an example of estimating effective transport properties, we employ an LBM heat transfer model [Wang et al., 2007b] for estimating effective thermal conductivity (K_{eff}) in porous media which is a non-homogenous composite of solid and fluid phases (Fig. 5.2).

The left (AB) and right (CD) end boundaries, separated by length L , are

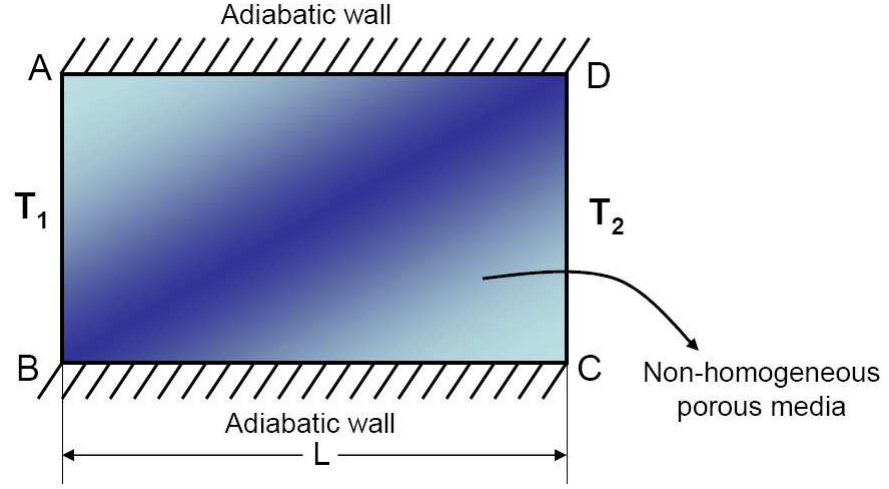


Figure 5.2: A schematic of non-homogeneous porous media

maintained at temperatures T_1 and T_2 , whereas the upper and lower boundaries (AD and BC) are adiabatic. The 2-dimensional LBM with Bhatnagar-Gross-Krook approximation can be written as [Chen and Doolen, 1998]:

$$f_\alpha(\mathbf{r} + \mathbf{e}_\alpha \delta t, t + \delta t) - f_\alpha(\mathbf{r}, t) = -\frac{1}{\tau} [f_\alpha(\mathbf{r}, t) - f_\alpha^{eq}(\mathbf{r}, t)] \text{ for } \alpha = 0, \dots, N-1 \quad (5.1)$$

where f_α is the evolution variable; \mathbf{r} is the position vector; t is the time; δt is the time step; N is the number of discrete particle velocities \mathbf{e}_α in each node, chosen as 9. Figure 5.3 shows the schematic of the discrete velocity vectors.

f_α^{eq} is the discrete equilibrium distribution function given as:

$$\begin{aligned} f_\alpha^{eq} &= 0 & \alpha &= 0 \\ &= T/6 & \alpha &= 1 - 4 \\ &= T/12 & \alpha &= 5 - 8 \end{aligned} \quad (5.2)$$

where, T is the system temperature. The N discrete velocities are given by:

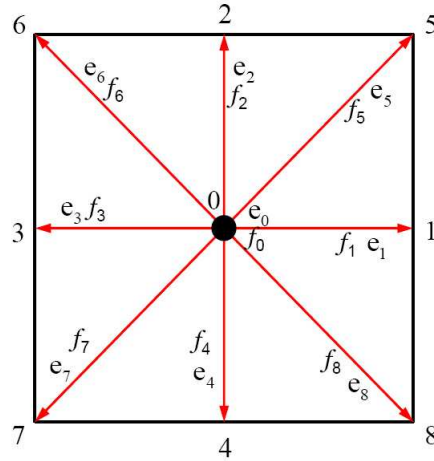


Figure 5.3: A schematic of discrete velocity vectors

$$\begin{aligned}
 \mathbf{e}_\alpha &= 0 & \alpha &= 0 \\
 &= (\cos\theta_\alpha \sin\theta_\alpha)c, & \theta_\alpha &= (\alpha - 1)\pi/2 & \alpha &= 1 - 4 \\
 &= \sqrt{2}(\cos\theta_\alpha \sin\theta_\alpha)c, & \theta_\alpha &= (\alpha - 5)\pi/2 + \pi/4 & \alpha &= 5 - 8 \quad (5.3)
 \end{aligned}$$

The relaxation time (τ) controlling the rate of approach to equilibrium for solid (s) and fluid (f) phases is given as:

$$\tau_s = 3K_s / (2(\rho C_p)_s c^2 \delta t) + 0.5 \quad (5.4)$$

$$\tau_f = 3K_f / (2(\rho C_p)_f c^2 \delta t) + 0.5 \quad (5.5)$$

where, K_s & K_f denote the solid and fluid phase thermal conductivities, respectively, $c = \delta x / \delta t$ is the lattice speed, with δx as the grid spacing, and $(\rho C_p)_s$ & $(\rho C_p)_f$ denote the solid and fluid phase heat capacities, respectively.

The heat flux (q) and T at any grid point location are given as:

$$q = \left(\sum_{\alpha} e_{\alpha} f_{\alpha} \right) (\tau - 0.5) / \tau \quad (5.6)$$

$$T = \sum_{\alpha} f_{\alpha} \quad (5.7)$$

For our simulations we employed the following boundary conditions as:

For isothermal boundaries:

$$f_\alpha - f_\alpha^{eq} = -(f_\beta - f_\beta^{eq}) \tag{5.8}$$

For adiabatic boundaries:

$$f_\alpha = f_\beta \tag{5.9}$$

where, α and β denote opposite directions in Fig. 5.3. The effective conductivity (K_{eff}) is calculated as:

$$K_{eff} = \frac{qL}{T_2 - T_1} \tag{5.10}$$

Preliminary results

We first validated our LBM for the cases where analytical solutions for K_{eff} exist, such as the series and parallel composites of pure solid and fluid phases. Table 5.1 compares analytical solution, numerical results presented by Wang et al. [2007b], and our simulation. Our results are in good agreement with the analytical solution and Wang et al. [2007b]. After validating, we applied

K_f/K_s	Parallel mode			Series mode		
	Analytical (W/mK)	Wang et al. (W/mK)	Present (W/mK)	Analytical (W/mK)	Wang et al. (W/mK)	Present (W/mK)
1/10	5.5	5.5	5.5	1.818	1.815	1.828
1/100	50.5	50.5	50.05	1.980	1.976	2.243

Table 5.1: Validation results for series and parallel composite non-homogenous media

our methodology on composite porous media structures which were generated

via the quartet structure generation method [Wang et al., 2007b], on a 2-dimensional mesh of 150 x 150 points. As shown in Fig. 5.4, we generated the series, parallel, diagonal, and random structured porous media, where the blue and red regions denote the solid and fluid phases, respectively. Table 5.2

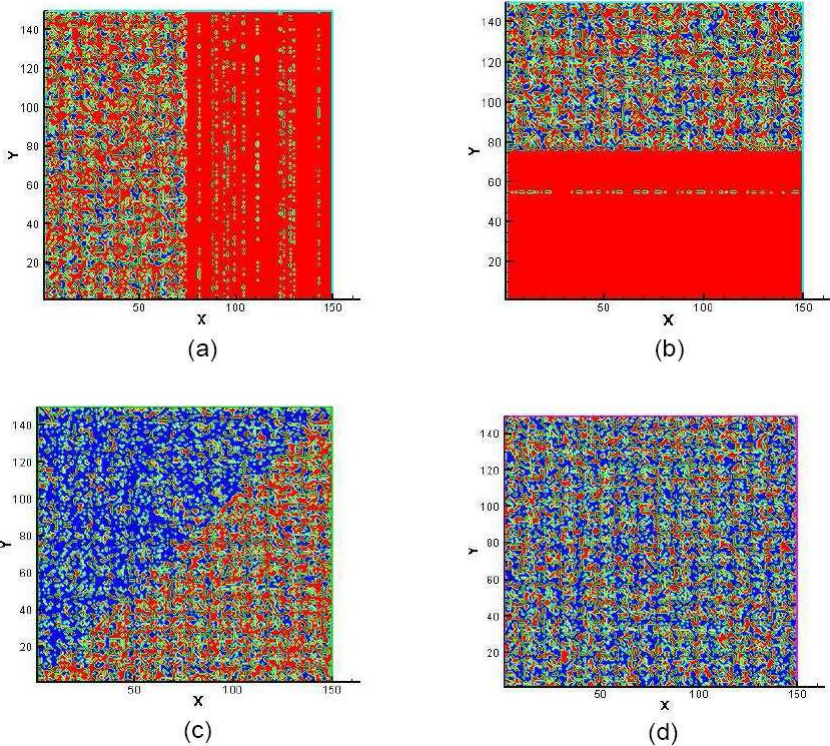


Figure 5.4: Porous structures for (a) series, (b) parallel, (c) diagonal, and (d) random configurations.

compares the results for effective conductivities of different overall porosities in different structural arrangements for $K_s/K_f = 100$. It is noted that conductivity of a series arrangement is lowest in both the porosity cases. Also, as the porosity decreases in the system, the effective conductivity in all the cases increases, where the amount of increase in series configuration is largest. While these results are preliminary, the essence of non-homogenous porous media description via a mesoscale theory is illustrated here; directions for future

Structural arrangement	Porosity	K_{eff}/K_f	K_{eff}/K_{rand}
Random	0.2	24.97	1
Series	0.2	16.66	0.66
Parallel	0.2	33.22	1.33
Diagonal	0.2	36.4	1.06
Random	0.5	12.76	1
Series	0.5	4.39	0.34
Parallel	0.5	16.96	1.329
Diagonal	0.5	18.086	1.417

Table 5.2: Effective conductivities for different porosities and structural arrangements. K_{rand} denotes effective conductivity for random structure.

work are presented in Chapter 6.

5.3 Molecular simulations for PEM

In this section, we examine mesoscopic/molecular descriptions for the PEM sub-component. A PEM is a semipermeable ionomer, designed to conduct protons, while being impermeable to reactants. The ‘ideal’ PEM characteristics include: (i) high proton conductivity at elevated temperatures, (ii) impermeability to fuel and other reactants, (iii) mechanical and chemical robustness, and (iv) reasonable cost. Among these, a key requirement is controlling PEM proton conductivity for attaining high PEFC performance. The PEM generally consists of polytetrafluoroethylene chains with hydrophilic perfluorosulfonate side groups (Fig. 5.5a). The water molecules within the system agglomerate in the vicinity of hydrophilic groups and form hydrophilic clusters. A network of these clusters forms passages for proton conduction within the PEM. Hence a detailed relationship between PEM structure, water uptake, and proton conduction is necessary for synthesis of novel PEMs, which overcome the

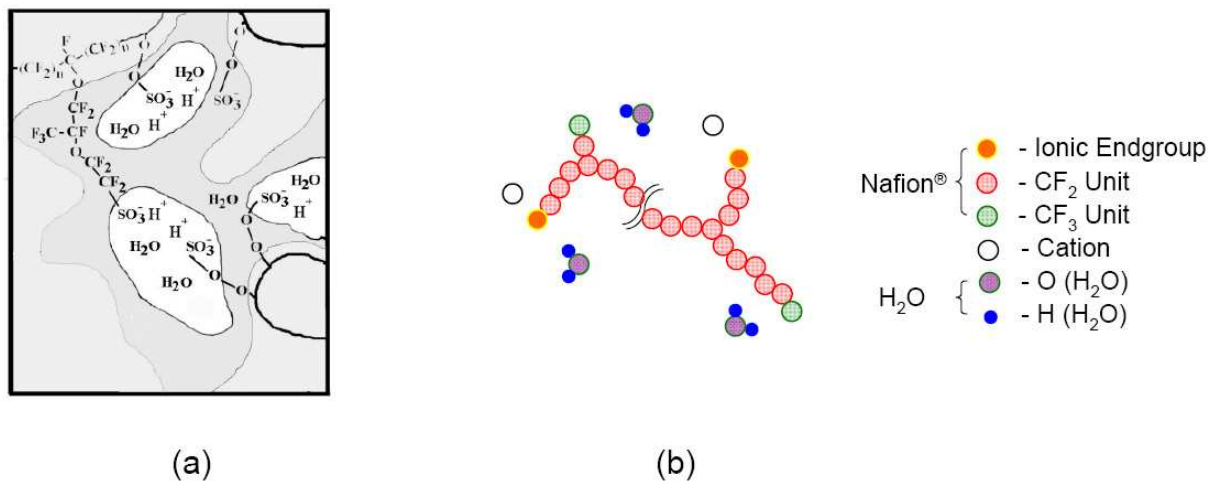


Figure 5.5: PEM (a) molecular structure, and (b) model used in our simulation.

limitations of state-of-the-art PEMs.

5.3.1 Molecular dynamics (MD) simulation

We develop a molecular model for the PEM system with the goal of establishing a relationship between PEM microstructure, water uptake and species (proton and water) transport processes. The molecular model of the PEM is shown in Fig. 5.5(b), comprising of polymeric chains, water molecules, and counterions. We use a coarse-grained, bead-spring model to represent a Nafion chain, consisting of a series of beads determining the backbone and branch chain lengths. A united atom approach, treating the CF_2 and CF_3 groups as one large bead with the mass of the combined individual atoms, is applied to reduce the computational cost.

The nonbonding interactions acting between all species were described using a combination of Lennard-Jones (LJ) potential and the Coulombic inter-

actions as:

$$U_{LJ}(r_{ij}) = 4\epsilon_{ij} \left[\left(\frac{\sigma_{ij}}{r_{ij}} \right)^{12} - \left(\frac{\sigma_{ij}}{r_{ij}} \right)^6 \right] + \frac{q_i q_j e^2}{4\pi\epsilon_0 r_{ij}} \quad (5.11)$$

where q_i is the charge of the i^{th} bead, ϵ_0 the permittivity in free space, r_{ij} is the distance between, and σ_{ij} & ϵ_{ij} are the LJ parameters between the i^{th} and j^{th} beads, respectively. The Coulombic interaction were used to account for interaction between the anionic endgroups of Nafion (SO_3^-) and counterions. The bonding interactions between adjacent beads in the Nafion chain were modeled via a finitely extensible nonlinear elastic (FENE) model as:

$$\begin{aligned} U_{FENE}(r_{ib}) &= \frac{1}{2} k R_0^2 \ln \left[1 - \left(\frac{r_{ib}}{R_0} \right)^2 \right] & r_{ib} \leq R_0 \\ &= \infty & \text{otherwise} \end{aligned} \quad (5.12)$$

where, r_{ib} is the inter-bead distance, k the spring constant, and R_0 the maximally extended bond length. In addition, the intra-molecular interactions within a water molecule model were accounted via the simple point charge (SPC) model [Krishnan et al., 2001], which accounts for intramolecular vibrations observed experimentally in water molecules [Walbran and Kornyshev, 2001]. The parameters cited in Eqs. (5.11) & (5.12) can be found in Jinnouchi and Okazaki [2003]. The counterions used in our simulation were sodium ions chosen for the feasibility of the MD simulation and verification with previous experimental data [Jinnouchi and Okazaki, 2003]. The simulation comprised of one polymer chain, 70 sodium ions, and water molecules corresponding to the water uptake in the unit cell. The periodic boundary conditions were applied

to mimic the bulk PEM behavior.

The MD simulation, via equations of motion, provides the trajectory of particles and allows for microscopic understanding of system dynamics. We apply the Langevin equation as the equation of motion for the i^{th} bead in the α_{th} Nafion molecule as:

$$m \frac{d^2 \mathbf{r}_{\alpha i}}{dt^2} = -\frac{\partial U}{\partial \mathbf{r}_{\alpha i}} - \zeta \cdot \frac{d\mathbf{r}_{\alpha i}}{dt} + \mathbf{f}_{\alpha i}(t) \quad \text{for } i = 1, \dots, N_m, \text{ and } \alpha = 1, \dots, N_p \quad (5.13)$$

where, $\mathbf{r}_{\alpha i}$ is the position vector at time t , N_m and N_p the number of beads per molecule and the number of Nafion molecules, respectively, m the bead mass, and U the total potential energy of the system. $\zeta = \Gamma \mathbf{I}$ is the frictional tensor, where \mathbf{I} is the unit tensor and $\Gamma = 0.5\tau^{-1}$ ($\tau = \sigma\sqrt{m/\epsilon}$) [Grest, 1996, Aoyagi et al., 2001]. $\mathbf{f}_{\alpha i}$ is Brownian random force generated from the fluctuation-dissipation theorem [Grest, 1996]. Unlike reversible Newton's mechanics, Eq. (5.13) is irreversible dynamic equation. The irreversibility is consequent from the coarse grained nature of Langevin equation.

We performed the MD simulations in NPT (constant particle number, pressure, and temperature) ensemble setting the pressure tensor P at 0.1 MPa, temperature T at 300 K, and varying the water uptake (λ , which is number of water molecules per SO_3^- group) in the electrolyte from 1.4 to 14.3 $[H_2O]/[SO_3^-]$. The Langevin equation of motion (Eq. (5.13)) was integrated with the time step, 0.5 or 1.0 fs. Since polymer structuralization requires large time scales, the initial configuration of the polymer membrane for MD

simulation was computed via the Metropolis Monte Carlo (MC) algorithm. The molecular configurations generated after 200,000 MC steps under NVT (constant particle number, volume, and temperature) ensemble were used to initialize the particle positions in MD simulations. The initial velocities were determined via Boltzmann statistics. The typical relaxation time for our MD simulations was 200 ps, as determined from the stable macroscopic properties such as the potential energy, after which physical properties of the system were deduced.

Preliminary results

Through MD simulations, we investigated the effect of water uptake λ , on PEM structure including hydrophilic/hydrophobic clustering, as well as the counterion transport mechanism. Figure 5.6 (a) illustrates variation of PEM system density with λ . The density decreases with increasing λ in both simu-

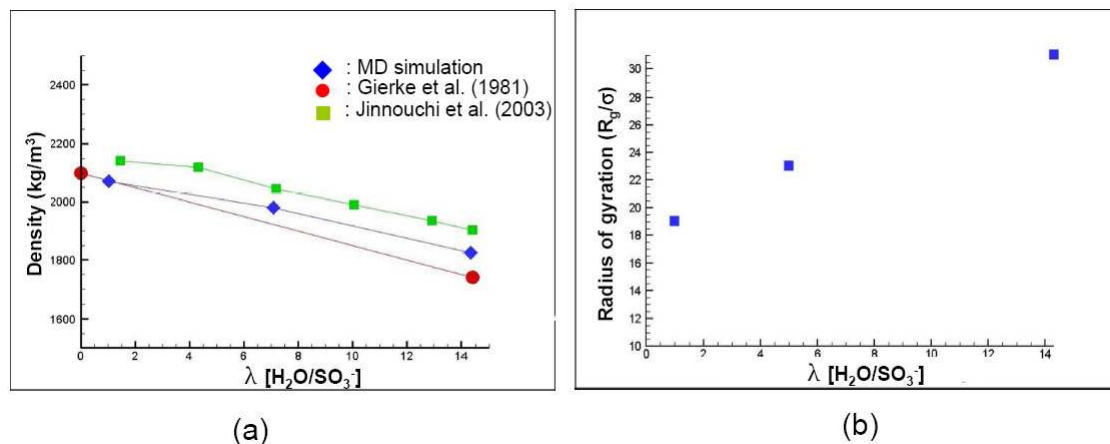


Figure 5.6: (a) PEM density and (b) radius of gyration for different water uptakes. $\sigma = 0.2 \text{ nm}$ is the reference length.

lations (our MD simulation and Jinnouchi and Okazaki [2003]) and experiment

(Gierke et al. [1981]), and predicted values are in qualitative agreement with experiment. Our simulation predicts, the commonly observed swelling phenomena of the PEM in a humidified atmosphere, which leads to a decrease in density. It is believed this swelling process leads to construction of pathways for water and counterion transport. The PEM swelling phenomena is also observed through Fig. 5.6 (b), which shows an increase in radius of gyration (R_g) with λ . This indicates that as area occupied by water molecules around the branch ends increases, PEM molecules tend to be geometrically stretched, leading to unfolding of the polymer.

We further confirmed the coherence of polar particles (water and counterions) in the PEM leading to cluster generation in our simulation, using pair correlation functions (PCFs, $g(r)$) between particles (Fig. 5.7). The PCFs

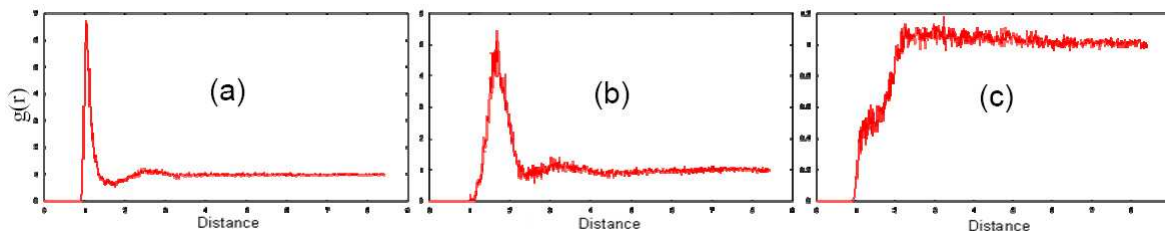


Figure 5.7: PCFs for (a) $\text{Na}^+\text{-H}_2\text{O}$, (b) $\text{Na}^+\text{-S}$, and (c) $\text{Na}^+\text{-CF}_2$

were calculated as the time average of the distance between particles, which is same as ensemble average due to ergodic hypothesis. A sharp peak in PCFs between polar particles indicates that almost all the counterions and the water molecules always exist within the cluster region. However, peaks between polar particles and nonpolar particles are not observed. We further examined the effect of λ on structuralization of hydrophilic clusters within the hydrophobic

PEM backbone. Figure 5.8 shows the two-dimensional snapshot of simulation cell for three values of λ , demonstrating that the high-water-density regions (hydrophilic clusters) increase with λ . The alignment of these clusters is dis-

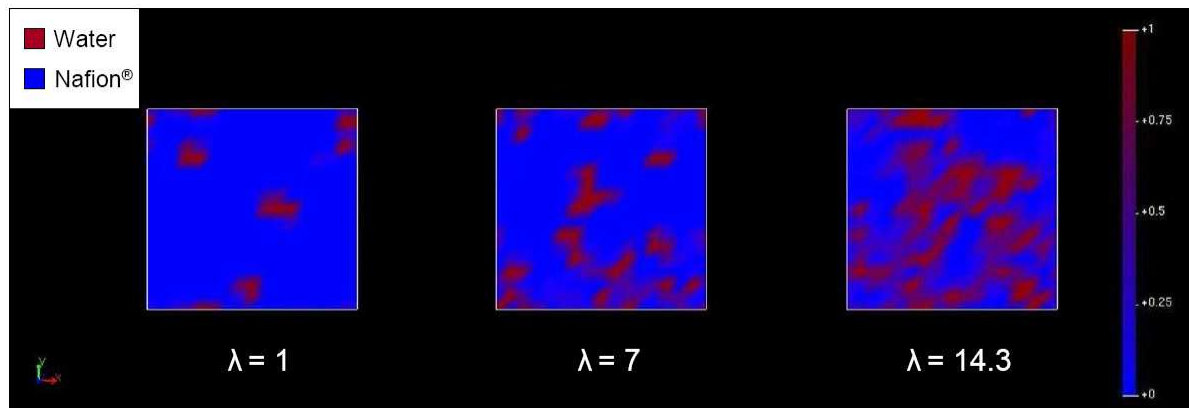


Figure 5.8: Water density distributions in a cross section of the simulation cell orderly, and as λ increases, these clusters cohere to form tortuous pathways.

In order to examine the transport processes of counterions with λ , we calculated the mean square displacement (MSD), which is proportional to the diffusion coefficient via Einstein's relation [Jinnouchi and Okazaki, 2003]. Figure 5.9 shows that the MSD increases, and counterion motion is enhanced as λ increases. This result in conjunction with the discussion before establishes a qualitative relationship between water uptake, water structure, and counterion motion. As discussed, an increase in λ leads to PEM swelling and expansion in hydrophilic clusters, which join together and form tortuous pathways. Also, the counterions and water molecules cohere together within this clustered region, as was observed through PCFs. Therefore, we can conclude that as water uptake increases, counterion motion is enhanced due to increase in number of clustered hydrophilic pathways. Moreover, this counterion motion takes place

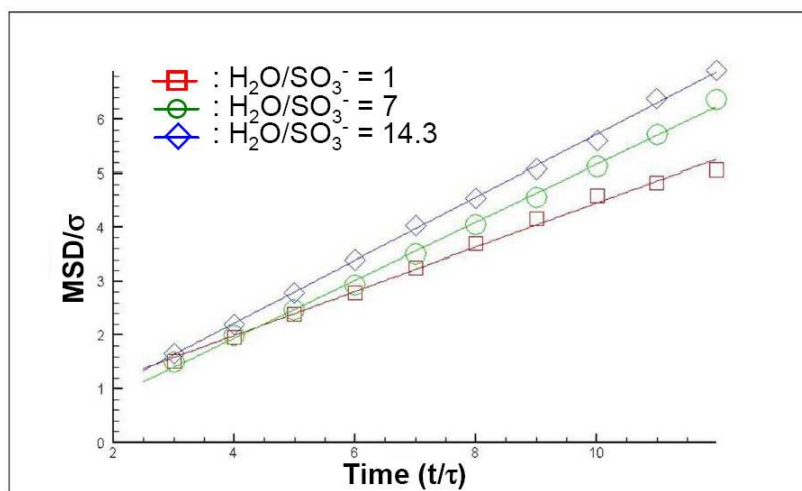


Figure 5.9: MSD of counterions

along with water molecules in a “vehicular” fashion. It is also noted that the cluster size and connection may strongly affect the transport properties in the electrolyte, and the low diffusivity in the electrolyte, as compared to ions in solution, is due to the tortuous shape of the clustered region.

5.4 System integration

As discussed before, achieving commercialization of PEFC devices requires several subcomponent- and system-level issues of cost, performance, and lifetime to be resolved. In an operating PEFC, multi-physical phenomena occur within each subcomponent at time and length scales different from its neighboring sub-components. There occur, fuel and oxidant flows represented via continuum theory within GCs, two phase gas liquid flow represented through meso-scale theories within GDLs, electrochemical reaction phenomena represented through *ab initio* methods to address catalytic issues within CLs, and proton & water transport processes represented via molecular-level theories

within PEM, In addition, these phenomena are represented through different kinds of mathematical structures including non-linear ordinary and partial differential equations as well as algebraic equations.

For addressing the PEFC technological issues at system-level, one attractive methodology will be to construct a ‘holistic’ integrated PEFC model in an efficient optimization framework, comprising of subcomponent descriptions at these different time and length scales. In Chapters 2-4, we stretched our integrated continuum modeling framework extensively to include mesoscopic information. However, for actual particle level descriptions introduced in this Chapter, novel strategies are required for integration.

In this dissertation, we introduce a novel reduced order model (ROM) framework for integrating systems of different time and length scale phenomena. Figure 5.10 illustrates the essence of our ROM framework, where we desire to integrate phenomena within two systems A and B. Integration here loosely

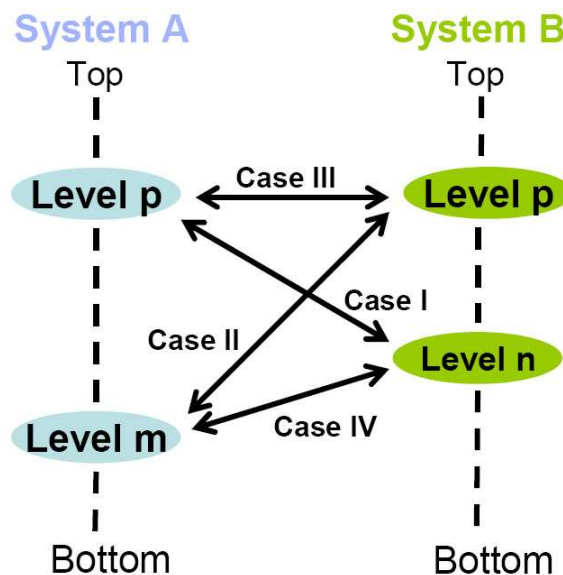


Figure 5.10: Schematic of the proposed ROM methodology.

means determining states within systems A and B, such that the continuity of states and fluxes at the interacting boundary of A and B are satisfied. The phenomena in either A or B can be represented through descriptions spanning from ‘top’ or the most coarse-grained to ‘bottom’ or the most fine-grained (Fig. 5.10). While the descriptions at the bottom-most level comprise of most detailed information, these may not be suitable for predicting overall system performance, especially for design. On the other hand, the descriptions at the top-most level, most suited to systems design, are least representative of system behavior and may be limited in accuracy as well as capabilities of controlling system performance via molecular tuning. In moving from bottom-to-top, the conventional scientific approach, termed as coarse graining process, involves information averaging which leads to loss in degrees of freedom in describing a system. One could more effectively define this ‘degree of coarse graining’ or loss in information in terms of increase in entropy of the system. Conversely, moving from top-to-bottom involves retrieving the detailed fine-grain information from the coarse-grained system, which may not be possible to achieve exactly. Both these approaches may be extremely time consuming, and an alternative ‘middle-out’ approach, which refers to starting from a ‘middle’ level and moving out towards ‘top’ or ‘bottom’ directions may be attractive.

We propose to integrate systems A and B described through phenomena at some arbitrary ‘ m ’ and ‘ n ’ levels ($m \neq n$) in the multi-scale hierarchy. Conventional approaches perform model integration for systems A and B described at the same ‘horizontal’ level descriptions (Case III in Fig. 5.10) however,

‘cross-linking’ strategies (Cases I, II, and IV) are not easily available.

One clever methodology for cross-linking is to project the ‘relevant’ three-dimensional system A information onto the two-dimensional interacting boundary, *i.e.*, developing a ROM for the interacting boundary from level m to a coarse-grained level p , which can be coupled to level n of system B (a level p to n linkage, denoted via $p \longleftrightarrow n$ (Case I in Fig. 5.10)) through available integration approaches. Alternatively, if $p \longleftrightarrow n$ linkage methodology is not available, we may project the system B information onto the interacting boundary, developing a ROM from level n , to level p , which may be linked to level m description of system A ($m \longleftrightarrow p$, Case II). If none of $p \longleftrightarrow n$ or $m \longleftrightarrow p$ linkage methodologies are available, ROMs for the interacting boundary may be constructed from both systems A & B and a $p \longleftrightarrow p$ linkage (Case III) may be made.

It is worth mentioning that a choice between Cases I-IV relies not only on the possibility of integration, but also on the desired computational expense and accuracy. For example, computational expense for Case I involves developing ROM from levels m to p and solving the resulting $p \longleftrightarrow n$ system. Similarly, expense for case III involves developing ROM from levels m to p & n to p , and solving the $p \longleftrightarrow p$ system. The latter method (Case III) may be less computationally expensive however, it possesses lower accuracy in the linking process.

Through linkage processes in Cases I-IV for given systems A & B, we finally aim to generalize linking rules at other multi-scale hierarchy levels where

linkage methodologies are unavailable.

In the following we propose an integrating strategy for systems A & B. We also present a test example for ROM development for the case where although integration method between A & B is available, using ROM may be attractive from the standpoint when integrated system optimization is computationally expensive.

5.4.1 Proposed ROM integration strategy

We first present our ROM integration strategy specific to Case I ($p \longleftrightarrow n$ linkage) in detail, through which integration for Cases II and III are demonstrated. Figure 5.11 shows the interacting systems A and B. The problem

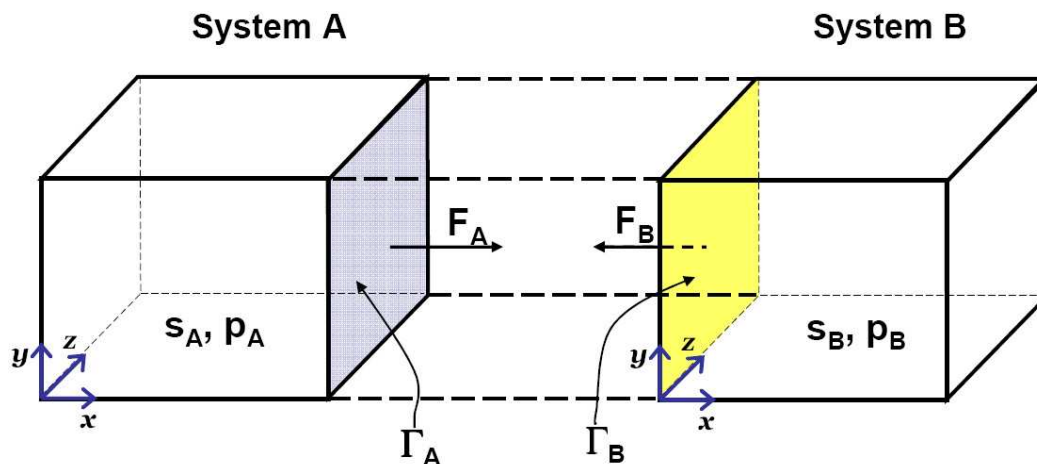


Figure 5.11: A schematic of two interacting systems A and B.

statement may be stated as follows:

Given: System A with description at level m via model \mathcal{M}_{Am} (where, \mathcal{M}_{Xy} denotes model for system X at level y), with interacting boundary Γ_A ; System B with description at level n via model \mathcal{M}_{Bn} , with interacting boundary Γ_B . $\mathbf{p}_A \in \mathcal{P}_A$ and $\mathbf{p}_B \in \mathcal{P}_B$ denote the vector of input & design parameters within

systems A and B, respectively, within domains \mathcal{P}_A and \mathcal{P}_B . The states within systems A & B, \mathbf{s}_A & \mathbf{s}_B can be determined by the solutions of \mathcal{M}_{Am} & \mathcal{M}_{Bn} once Γ_A & Γ_B and \mathbf{p}_A & \mathbf{p}_B are specified. It is desired to integrate systems A and B, which implies determining \mathbf{s}_A and \mathbf{s}_B satisfying:

Continuity: $\Gamma_A = \Gamma_B$, and

Flux continuity: $\mathbf{F}_A = -\mathbf{F}_B$.

Here, \mathbf{F}_A and \mathbf{F}_B denote an appropriate representation for the fluxes through boundaries Γ_A and Γ_B , respectively, which can be determined once \mathbf{s}_A & \mathbf{s}_B are known. In addition, it is desired to minimize the objective function $\phi(\mathbf{p}_A, \mathbf{p}_B, \mathbf{s}_B)$. This specific case where we ignore dependence of ϕ on \mathbf{s}_A , resembles our GDL-CL modeling case, where objective function is current density dependent on design parameters within both GDL and CL, and states within CL only.

Our proposed solution comprises of the following three steps:

1. **Boundary representation:** We first assume a functional representation for the boundary Γ_A , as $\Gamma_A = \mathbf{g}(y, z, \alpha)$, where $\alpha \in \mathcal{A}$ is the vector of adjustable parameters and y & z represent the co-ordinate axes. We assume that appropriate choices for \mathbf{g} and dimension of vector α are available such that \mathbf{g} spans all possible boundary profiles resulting from different parametric inputs \mathbf{p}_A and \mathbf{p}_B within \mathcal{P}_A and \mathcal{P}_B .
2. **ROM generation:** We sample values of α & \mathbf{p}_A , and generate snapshots for output flux \mathbf{F}_A for each sampled set, calculated from the solution of

\mathcal{M}_{Am} . Through these snapshots, we construct a ROM based on principal component analysis (PCA) [Lang et al., 2009] for \mathbf{F}_A at level p as $\mathcal{M}_{F_{Ap}}(\alpha, \mathbf{p}_A)$.

3. **Integrated system solution:** The system B model \mathcal{M}_{Bn} is solved via ROM $\mathcal{M}_{F_{Ap}}$ and $\mathbf{g}(y, z, \alpha)$ as inputs to the flux \mathbf{F}_B and boundary Γ_B , respectively, to obtain \mathbf{s}_B and α , for specified values of parameters \mathbf{p}_A and \mathbf{p}_B . This process is illustrated as Case I in Fig. 5.12.

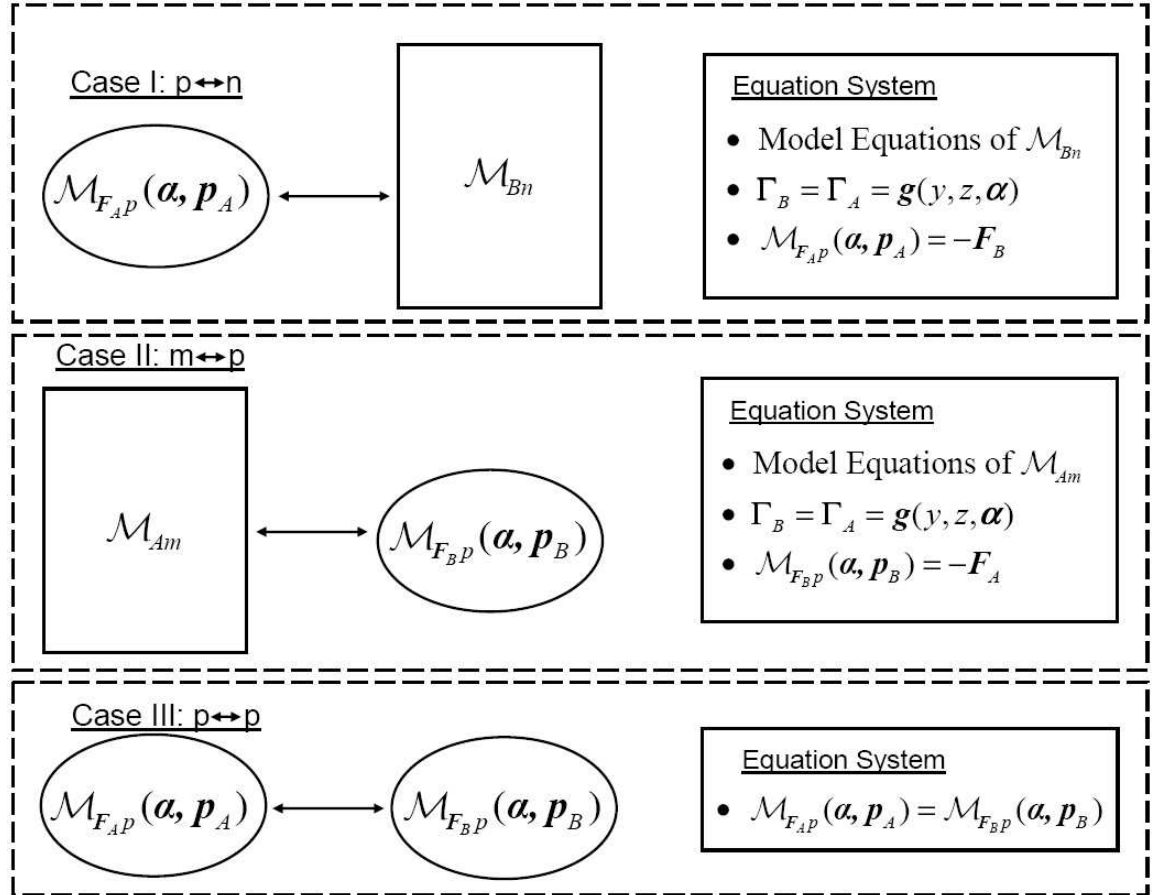


Figure 5.12: A schematic of linkages in Cases I, II, and III, and the resulting equation systems.

Remarks:

- Once α is obtained, \mathbf{s}_A can be obtained through solution of model \mathcal{M}_{Am} , through, $\Gamma_A = \mathbf{g}(y, z, \alpha)$.
- The optimization problem may be solved by minimizing $\phi(\mathbf{p}_A, \mathbf{p}_B, \mathbf{s}_B)$ satisfying equation system in Case I in Fig. 5.12.
- If a $p \longleftrightarrow n$ coupling is not available, integrated solution may be found through $m \longleftrightarrow p$ coupling (Case II in Fig. 5.12), in which a ROM $\mathcal{M}_{\mathbf{F}_B p}$ for \mathbf{F}_B is constructed and fed to \mathcal{M}_{Am} for obtaining \mathbf{s}_A and α . It is noted that optimization problem however, is not trivial in this case, as a direct linkage of objective function $\phi(\mathbf{p}_A, \mathbf{p}_B, \mathbf{s}_B)$ and states in system B is not present in the resulting equation system.
- If neither $p \longleftrightarrow n$, nor $m \longleftrightarrow p$ couplings are available, integrated solution may be found through $p \longleftrightarrow p$ coupling (Case III in Fig. 5.12), in which ROMs $\mathcal{M}_{\mathbf{F}_A p}$ & $\mathcal{M}_{\mathbf{F}_B p}$ for \mathbf{F}_A & \mathbf{F}_B , respectively, are constructed to obtain α . \mathbf{s}_A and \mathbf{s}_B are obtained once α is determined, through solutions of \mathcal{M}_{Am} and \mathcal{M}_{Bn} , respectively.

5.4.2 ROM methodology when integrated system solution is available

Before actual system integration, we performed a small case study for PCA based ROM strategy for our integrated GDL-CL system [Jain et al., 2008b].

Here, we explore this strategy to develop reduced representations for the interacting boundary to test the accuracy and computational times of the resulting optimization problem. This test example also forms a basis for strategies outlined for actual system integration.

Assuming systems A and B are described via models at same level l here as \mathcal{M}_{Al} and \mathcal{M}_{Bl} ; the procedure is outlined as the following two steps:

1. **ROM for boundary:** For sampled values of \mathbf{p}_A and \mathbf{p}_B , we generate multiple snapshots for the boundary Γ_A , calculated from the integrated solution of systems A and B. We construct ROM for Γ_A at level p as $\mathcal{M}_{\Gamma_{Ap}}(\mathbf{p}_A, \mathbf{p}_B)$.
2. **Optimization:** The optimization problem may be solved by minimizing $\phi(\mathbf{p}_A, \mathbf{p}_B, \mathbf{s}_B)$ *w.r.t.* model equations \mathcal{M}_{Bl} with boundary Γ_B set to $\mathcal{M}_{\Gamma_{Ap}}(\mathbf{p}_A, \mathbf{p}_B)$.

It is noted that flux continuity condition here was implicitly assumed, as the ROM $\mathcal{M}_{\Gamma_{Ap}}(\mathbf{p}_A, \mathbf{p}_B)$ was generated through snapshots of integrated system solutions.

We apply this methodology to the two-dimensional GDL-CL system reported in Jain et al. [2008b]. The details of ROM development have been thoroughly discussed in Lang et al. [2009], and only details specific to our system are presented here.

We first construct ROMs for the GDL-CL boundary, for state variables oxygen mole fraction $x_{O_2}^\beta(y)$ and solid phase potential $\phi_s^{cl,\beta}(y)$ (where super-

5.4.2 ROM methodology when integrated system solution is available

script β is used to denote the boundary values), as a function of set of decision variables \mathbf{p} comprising platinum loading ($m_{Pt}(mg/cm^2)$), platinum to carbon ratio (Pt/C), PEM volume fraction (ϵ_{agg}), and GDL void fraction (ϵ_v^{gdl}). Fifteen grid points along y direction were used. For generating snapshots, we uniformly sampled 5 data values each within the following ranges of decision variables: $m_{Pt} \in [0.2, 1.25]$, $Pt/C \in [0.2, 0.75]$, $\epsilon_{agg} \in [0.2, 0.8]$, and $\epsilon_v^{gdl} \in [0.7, 0.9]$. The data sets violating physical constraints represented via algebraic equations in the model were discarded leaving 395 feasible data sets. For determining the principal components (PCs), we performed singular value decomposition of the resulting snapshot matrix. Via two PCs each for $x_{O_2}^\beta(y)$ and $\phi_s^{cl,\beta}(y)$, entire snapshot matrices could be represented within 99.9% accuracy. The reduced data set was re-mapped via a kriging method [Lophaven et al., 2002] to obtain ROMs $\bar{x}_{O_2}^\beta(y, \mathbf{p})$ and $\bar{\phi}_s^{cl,\beta}(y, \mathbf{p})$.

We then solved the optimization problem for maximizing current density I , with only CL region modeling equations, with boundaries from GDL side as $\bar{x}_{O_2}^\beta(y, \mathbf{p})$ and $\bar{\phi}_s^{cl,\beta}(y, \mathbf{p})$. Table 5.3 shows the results for optimization for a full GDL-CL system and the proposed ROM-CL systems. Excellent agreement is

Table 5.3: Optimization results comparing proposed ROM and full GDL-CL model.

	$I^*(A/cm^2)$	$m_{Pt}^*(mg/cm^2)$	$(Pt/C)^*$	ϵ_{agg}^*	ϵ_v^{gdl*}	CPU (s)
Full-model	0.912	0.534	0.467	0.635	0.794	106
Proposed ROM	0.968	0.527	0.467	0.639	0.784	10

found between the optimal values of decision variables, where as the optimal current densities are within 5% error. This error may further be reduced through other sampling methods such as Latin hypercube sampling [Lophaven et al., 2002], or via larger number of sampling points. Furthermore, the CPU time taken for the optimization problem reduces by an order of magnitude, indicating the promising nature of the proposed ROM methodology.

5.5 Summary

In this Chapter, we introduced particle level descriptions within the GDL and PEM sub-components, *i.e.*, one level detailed descriptions in the multi-scale hierarchy. We introduced an LBM for predicting effective transport within non-homogenous porous media, which was verified for the cases where analytical solution exists, and extended for various porous media configurations. We further investigated the PEM structure, water uptake, and counterion transport relationships via MD simulations on the PEM. Finally, we proposed a novel multi-scale integration strategy based on reduced order methods.

Notation

\mathcal{A}	=	Domain of α
c	=	Lattice speed, m/s
e	=	Electronic charge, C
\mathbf{e}_α	=	Discrete velocity vector, m/s
f	=	Evolution variable
$f_{\alpha i}$	=	Brownian force term, N
\mathbf{F}_i	=	Flux from system i
\mathbf{g}	=	Functional representation for boundary
$g(r)$	=	Radial distribution function
k	=	Spring constant, J/m^2
K	=	Thermal conductivity, $W/m - K$
L	=	Length, m
m	=	Bead mass, kg
\mathcal{M}_{Xy}	=	Model for system X at level y
N	=	Number of discrete particle velocities
\mathbf{p}_i	=	Input or decision variables of system i
\mathcal{P}_i	=	Domain of \mathbf{p}_i
q_i	=	Charge on i^{th} bead, C
q	=	Heat flux, J/m^2
\mathbf{r}	=	Position vector, m
r_{ib}	=	Inter-bead distance, m
R_o	=	Maximally extended bond length, m

R_g = Radius of gyration, m

\mathbf{s}_i = State variables of system i

t = Time, s

T = Temperature, K

U = Potential energy, J/C

x_{O_2} = Oxygen mole fraction

Greek Symbols

α = Vector of adjustable parameters in \mathbf{g}

δx = Grid spacing, m

δt = time step, s

ζ = Friction tensor, kg/s

Γ_i = Interacting boundary of system i

λ = Number of water molecules per SO_3^- group

ϕ = Objective function

ϕ_s^{cl} = Solid phase potential in catalyst layer, *Volt*

ρC_p = Heat capacity, $J/m^3 - K$

$\sigma_{ij}, \epsilon_{ij}$ = Lennard-Jones potential parameters

τ = Relaxation time, s

Subscripts and Superscripts

A, B = Subscripts for systems A and B

α = Discrete particle velocity direction

β = Superscript for boundary values

cl = Catalyst layer

eq = Equilibrium value

f = Fluid

m, n, p = Subscripts for multi-scale hierarchical levels

$rand$ = Random configuration

s = Solid

Chapter 6

Conclusions

In this Chapter, we first present conclusions of the thesis and highlight our specific contributions Chapter-wise, and present recommendations for future work.

6.1 Thesis conclusions and contributions

In **Chapter 2**, we propose a generalized modeling and optimization framework for rigorous computational fluid dynamics (CFD) models in PEFC systems. We develop a comprehensive multi-dimensional PEFC model that takes into account major transport processes in the gas channels (GCs) and the membrane electrode assembly. A detailed water transport equation, accounting for electro-osmotic drag, diffusion, and hydraulic permeation, is also incorporated into the model assuming single-phase flows. The resulting system of partial differential algebraic equations is fully discretized using a finite volume scheme leading to a large-scale non-linear system of equations which is linked to IPOPT [Wächter and Biegler, 2006] solver. Using this framework, parameter estimation is performed to estimate catalyst layer (CL) fitting pa-

rameters and polymer electrolyte membrane (PEM) water diffusion coefficient, thus illustrating the utility of parameter estimation as a tool complementary to modeling for the regions where system is modeled with a lumped parameter approach. We employ errors-in-variables-measured formulation to multiple I-V data point cases that yield parameter estimates such that model predictions are accurate for wide operation ranges. The proposed methodology leads to fast and efficient solution of large-scale non-linear programs in a few CPU seconds and a small number of iterations. The parameters from different data point cases are determined uniquely.

We further employ this framework to perform water management parametric studies to examine water transport mechanisms and distribution, especially within the PEM, and to examine the overall system performance. We observe that counter-flow arrangement leads to better performance than the co-flow arrangement, especially for the conditions of low inlet humidity and low pressure, due to an internal water recirculation mechanism which facilitates higher PEM hydration. Moreover, as inlet gas humidity increases, the overall water uptake in the system increases which improves the ionic conductivity of the PEM and enhances the overall system performance. Also, thin PEMs perform significantly better than thicker PEMs due to their smaller resistance path to proton transport, and due to a more uniform water distribution along the x-direction.

Specific contributions/accomplishments in this Chapter include:

- Construction of an integrated modeling and optimization framework for multi-physical, multi-component (including open channel, porous media, and membrane systems) energy systems.
- Incorporation of CFD models in an efficient optimization framework.
- Demonstration of optimization as a parameter estimation tool complementary to modeling, with focus on PEM water management in PEFCs.

In **Chapter 3**, we replace the phenomenological description of CL in Chapter 2 through a more realistic continuum/mesoscopic description, providing control over actual physical parameters. Specifically, we reformulate an agglomerate model of CL into a condensed form, for the optimization of PEFC cathodes. This model accounts for gas diffusion layer (GDL) species and charge transports. It also describes species and charge transports, as well as reaction phenomena within the CL and individual agglomerates. The governing equations are discretized using a finite difference method and resulting nonlinear program is linked to the IPOPT optimization solver.

We perform Pt minimization for a specified voltage for several current density values. The results indicate that the optimal Pt mass increases with both current density and voltage of operation. The relationship between optimal Pt mass and current density obeys a power law at low to medium current densities of operation.

We first verify our results for I maximization, with those of Secanell et al. [2007] and further extend our methodology for obtaining the optimal Pt distri-

bution along the CL width by systematically subdividing CL in 2^N zones, and solving the multi-zone PDE-constrained optimization problem. Our results indicate that significant improvement in current density can be obtained by placing higher amounts of Pt adjacent to the PEM-CL interface.

Specific contributions/accomplishments in this Chapter include:

- Construction of an integrated modeling and optimization framework for multi-physical (including charge & mass transport, and electrochemical reaction), multi-component energy systems.
- Obtaining of a novel relationship between minimum amount of Pt required and current density of operation.
- Introduction of non-homogeneity within CL agglomerate model in an optimization framework, to obtain Pt distribution.

In **Chapter 4**, we expanded our continuum CL description to include as much micro-structural information as possible within our existing optimization framework, with the goal of examining the sensitivity to cell performance for different CL micro-structures. We first examined the shape sensitivity of agglomerates by introducing spherical (3-D), cylindrical (2-D), and plate-like (1-D) agglomerates. The shape effect on intra-agglomerate transport processes was examined via effectiveness factors, and on inter-agglomerate transport processes through different effect transport models. We obtained significant differences in both simulation and optimization results, with sphere model predicting the highest performance.

We also examined the relationship between self-similar CL structures via systematic variation in particle number and size, conserving the other physical properties. We obtained up to 3 times enhancement in the current density for an order of magnitude lower agglomerate size. We further examined polydisperse systems, through effectiveness of mixture of particle sizes, for several particle mixtures. Interestingly, for bi-modal distributions, the optimal current density obeys a cubic relationship with fraction of small agglomerates in the mixture.

We further introduced a spherical shell agglomerate model where, we first verified the effectiveness expression with existing empirical result, and further derived a general effectiveness expression with Biot number as a parameter. We obtained the limiting performance for this shell model in between the spherical agglomerate model and the pseudo-homogenous model in literature, in which CL is described as a homogenous system without any agglomerates. Via this shell model, we also relaxed the commonly employed assumption, in both microscopic and macroscopic CL descriptions, of uniformly available triple phase boundaries for electrochemical reaction, through a 2 zone agglomerate where different zones possess different rates of reaction.

Specific contributions/accomplishments in this Chapter include:

- Introduction of micro-structural (mesoscopic) information within the state-of-the-art continuum description of CL, suitable for system optimization, through examination of several CL morphologies.

- Demonstration of large sensitivity in simulation and optimization results for different CL structures.
- Introduction of non-homogenous distribution of triple phase boundary within agglomerate CL model.

In **Chapter 5**, we geared from field descriptions to actual particle descriptions, moving one level down in the multi-scale hierarchy. We first introduced the lattice Boltzmann methods (LBMs) for estimating transport through non-homogenous porous media via effective thermal conductivity. We verified our LBM for series and parallel arrangements of pure solid and fluid phases with existing analytical solution, and further extended our methodology for composite porous media structures including series, parallel, diagonal and random arrangements, for different porosities. The series arrangement gave the lowest values for effective conductivity.

We also constructed a coarse-grained bead spring molecular model for PEM, for performing molecular dynamics simulations, with the goal of understanding the relationship between PEM structure, water uptake and counterion motion. Our preliminary results indicated that an increase in water uptake leads to swelling of PEM. Also, hydrophilic clusters around the PEM side-chain ends grow in size, which connect to form tortuous pathways for counterion transport along with other water molecules.

We further proposed a novel multi-scale system integration strategy for systems described via different time and length scale phenomena, based on re-

duced order models (ROMs). The methodology involves projecting the entire relevant information of one of the systems on to the interacting boundary, and constructing a ROM for the boundary information at such a coarse-grained level, where linkage methodology with the other system is available. We also presented a small test example for principal component analysis based ROM for integrated systems, which showed significant improvement in computational times.

A large breadth of topics were explored in this Chapter. Specific achievements which are promising for future research include:

- Construction of framework for predicting effective transport in non-homogenous porous media via mesoscopic theories.
- Successful qualitative prediction of PEM structure dynamics and counterion transport mechanism via molecular theories.
- Introduction of novel multi-scale system integration methodology based on reduced order methods.

6.2 Recommendations for future work

In this dissertation, we have proposed a generalized modeling and optimization framework for multi-scale, multi-phenomena energy systems, with focus on PEFCs. We believe the following recommendations will further improve our understanding in PEFC behavior, which at the same time, pose great challenges in both numerical and physical aspects.

6.2.1 Model sophistication (Continuum)

We have presented rigorous modeling and optimization strategies for integrated continuum descriptions, therefore, model sophistication to unravel PEFC behavior at continuum level is a natural leading step. Following enhancements to the continuum descriptions presented in Chapters 2-4 are recommended:

- **Two phase flows and thermal management:** At high current densities, due to excess water generation in the electrochemical reaction, partial pressure of water vapor may exceed the saturation pressure and water may condense in the cathode region. The liquid water formed adversely effects the performance by blocking the oxygen transport in GDL from GC to the reaction sites, and by blocking the active sites on the CLs. Efficient water removal, is therefore a key issue to PEFC performance. This issue is coupled with the thermal management issue, which refers to efficient heat removal strategies. Also, due to the sensitivity of PEM to temperature fluctuations, and strong dependence of water saturation pressure, transport and kinetic properties to temperature, heat transport becomes a crucial phenomena to consider. The processes that need to be described here are: Liquid water coverage of CL active sites, two-phase porous media flow, the droplet formation and removal at the GDL / GC interface, and two phase gas-liquid flow in the GC; as well as convective and conductive energy transports through GCs & GDLs and heat generation in CLs & PEM.

- **Transient behavior:** Analysis of transient response in PEFCs is critical to automotive applications. There are several sub-processes in PEFC which have different dynamic response times, such as the GDL gas transport (with time constant $\tau \sim 0.1 - 1s$), PEM hydration/dehydration process ($\tau \sim 10s$), and water accumulation and removal in CLs and GDLs. As an example, a step increase in current density causes voltage to drop gradually to a new steady state value, as the O_2 concentration in the CL, and PEM hydration levels gradually decrease and increase, respectively. Particularly the following questions need to be answered: (i) How different parameters affect the start-up times and characteristics of PEFC? (ii) How PEFC responds to sudden changes in operating parameters? and (iii) What may be the most important control parameters? One of the methods to address these would be introducing accumulation terms in the balance equations for all sub-components and examining the response of both system output and the different sub-processes *w.r.t.* the operation parameters. This would isolate the transient behavior of each subsystem, and would identify the specific critical processes which may require control action.

6.2.2 Multi-scale modeling and system integration

The multi-scale modeling and system optimization strategies presented in Chapter 5 are promising yet were preliminarily examined, and require significant future investigation.

- **PEM molecular modeling:** Several modifications may be made to the MD simulation framework presented for examining the effect of water uptake on PEM structure and proton motion. First, the sodium ion employed in the simulation needs to be replaced by an actual proton requiring modeling of additional interaction states (*e.g.*, Zundel, Eigen) which a proton possesses with surrounding water molecules. The SPC model used for water may be replaced by 4-point charge models such as the TIP4P, to determine their effect on water clustering behavior. Furthermore, different structures of PEM, *e.g.*, which possess different chain and branch lengths may be examined, which affect the water clustering and proton motion. Finally, the transport properties calculated in the MD simulation (diffusion coefficient and conductivity) can be fed to the continuum description of PEM presented in Chapter 2, providing a tool to manipulate the cell output performance via molecular tuning.
- **Effective transport in non-homogenous porous media:** In Chapter 5, we examined the standard geometrical structures of composite porous structures, *i.e.*, the series, parallel, diagonal, and random arrangements, however, effective transport properties may be also be correlated with generalized structures via radial distribution functions. Also, the two-dimensional analysis presented here needs to be generalized to three-dimensional systems closer to realistic scenarios. For application to a PEFC GDL, fluid flow model may be introduced in conjunction

with the effective transport model. Especially, our LBM formulation is attractive for describing multi-phase, multi-species (oxygen and water) transport phenomena within the cathode GDL.

- **System integration:** The ROM strategy introduced in Chapter 5 first needs to be benchmarked through integrated systems examples, *e.g.*, the GDL-CL system introduced in Chapter 3. The GDL and CL sub-systems here, were both described via continuum descriptions and integration methodologies for these are readily available; an application of ROM based integration acts as a validation to our proposed methodology. Specific to the methodology itself, followings may be examined:
 - Better sampling methods instead of uniform sampling, such as Latin hypercube sampling, for reducing the number of snapshots required for similar or better representation of the interacting boundary.
 - Exploring of other data reduction and mapping methods.

Also, examination of ROM based integration for all the cases I-IV presented in Fig. 5.10, may provide general integration rules for the levels where integration methodologies are not readily available. Furthermore, an examination of computational cost and accuracy obtained in each of the cases I-IV needs to be done. Once successfully tested on benchmark systems, this ROM strategy may be applied in integrating multi-scale sub-systems frequently found in energy systems.

Bibliography

- T. Aoyagi, J. Takimoto, and M. Doi. Molecular dynamics study of polymer melt confined between walls. *J. Chem. Phys.*, 115:552, 2001.
- R. Aris. On shape factors for irregular particles-i. the steady-state problem. diffusion and reaction. *Chem. Engng Sci.*, 6:262-268, 1957.
- P. Berg, K. Promislow, J. S. Pierre, and J. Stumper. Water management in pem fuel cells. *J Electrochem Soc*, 151:A341–A353, 2004.
- D. M. Bernardi and M. W. Verbrugge. Mathematical model of a gas diffusion electrode bonded to a polymer electrode. *AIChE J*, 37:1151–1163, 1991.
- R. B. Bird, W. E. Stewart, and E. N. Lightfoot. *Transport Phenomena*. 1960.
- D. A. G. Bruggemann. Calculation of the various physical constants of heterogeneous substances. i: Dielectric constants and conductivities of mixtures of isotropic substances. *Ann. Phys.*, 5:636–664, 1935.
- B. Carnes and N. Djilali. Systematic parameter estimation for pem fuel cell models. *J Power Sources*, 144:83–93, 2005.
- S. Chen and G. D. Doolen. Lattice boltzmann method for fluid flows. *Annu. Rev. Fluid Mech.*, 30:329, 1998.

- P. Costamagna and S. Srinivasan. Quantum jumps in the pemfc science and technology from the 1960s to the year 2000: Part i. fundamental scientific aspects. *J Power Sources*, 102:242–252, 2001.
- A. V. Fiacco and G. P. McCormick. *Nonlinear Programming Sequential Unconstrained Minimization Techniques*. Philadelphia: SIAM, 1990.
- R. Fourer, D. M. Gay, and B. W. Kernighan. *AMPL: A Modeling Language for Mathematical Programming*. Belmont, CA: Duxbury Press, 1992.
- T. F. Fuller and J. Newman. Water and thermal management in solid-polymer-electrolyte fuel cells. *J Electrochem Soc*, 140:1218–1225, 1993.
- T. D. Gierke, G. E. Munn, and F. C. Wilson. The swelling behaviour of perfluorinated ionomer membranes in ethanol/water mixtures. *J. Polym. Sci: Part A-2*, 19:1687, 1981.
- D. W. Green and R. H. Perry. *Perry's Chemical Engineers' Handbook*. New York, NY: McGraw-Hill, 2008.
- G. S. Grest. Grafted polymer brushes in polymeric matrices. *J. Chem. Phys.*, 105:5532, 1996.
- V. Gurau, H. Liu, and S. Kakac. Two-dimensional model for proton exchange membrane fuel cells. *AIChE J*, 44:2410–2422, 1998.
- W. He, J. S. Yi, and T. V. Nguyen. Two-phase flow model of the cathode of pem fuel cells using interdigitated flow fields. *AIChE J*, 46:2053–2064, 2004.

- W. H. J. Hogarth and J. B. Benziger. Operation of polymer electrolyte membrane fuel cells with dry feeds: Design and operating strategies. *J Power Sources*, 159:968–978, 2006.
- M. Hyun, S. Kim, D. Jung, B. Lee, D. Peck, T. Kim, and Y. Shul. Prediction of anode performances of direct methanol fuel cells with different flow-field design using computational simulation. *J Power Sources*, 157:875–885, 2006.
- P. Jain, L. T. Biegler, and M. S. Jhon. Parametric study and estimation in cfd-based pem fuel cell models. *AIChE J*, 2008a.
- P. Jain, L. T. Biegler, and M. S. Jhon. Optimization of polymer electrolyte fuel cell cathodes. *Electrochemical and Solid-State Letters*, 11:B193–B196, 2008b.
- R. Jinnouchi and K. Okazaki. Molecular dynamics study of transport phenomena in perfluorosulfonate ionomer membranes for polymer electrolyte fuel cells. *J. Elec. Soc.*, 150:E66, 2003.
- H. Ju, H. Meng, and C. Y. Wang. A single-phase, non-isothermal model for pem fuel cells. *Int J Heat Mass Tran*, 48:1303–1315, 2005.
- W.T. Kim, S.S. Ghai, Y. Zhou, I. Staroselsky, H.D. Chen, and M.S. Jhon. Magnetic recording: Systems, heads, channels, head-disk interference, modeling-head-disk interface modeling with the lattice boltzmann method. *IEEE Trans. Magn.*, 41:3016, 2005a.

- W.T. Kim, M.S. Jhon, Y. Zhou, I. Staroselsky, and H.D. Chen. Nanoscale air bearing modeling via lattice boltzmann method. *J. Appl. Phys.*, 97:304, 2005b.
- M. Krishnan, A. Verma, and S. Balasubramanian. Computer simulation study of water using a fluctuating charge model. *Proc. Indian Acad. Sci. (Chem. Sci.)*, 113:579, 2001.
- Y.-D. Lang, A. Malacina, L. T. Biegler, S. Munteanu, J. I. Madsen, and S. E. Zitney. Reduced order model based on principal component analysis for process simulation and optimization. *Energy Fuels*, 23:1695–1706, 2009.
- J. Larminie and A. Dicks. *Fuel Cell Systems Explained*. New York, NY: Wiley, 2002.
- S. K. Lophaven, H. B. Nielsen, and J. Sondergaard. Dace: A matlab kriging toolbox. Technical Report IMM-TR-2002-12, Informatics and Mathematical Modelling, Technical University of Denmark, DK-2800 Kgs. Lyngby Denmark, August 2002.
- C. Marr and X. Li. Composition and performance modelling of catalyst layer in a proton exchange membrane fuel cell. *J Power Sources*, 77:17–27, 1999.
- M. Matzopoulos. Advanced modeling accelerates fuel cell development. *FC Focus*, pages 44–47, 2007.
- J. C. Maxwell. A treatise on electricity and magnetism, 1881.

- M. M. Mench, C. Y. Wang, and S. T. Thynell. An introduction to fuel cells and related transport phenomena. *International journal of transport phenomena.*, page 3, 2001.
- P. A. P. Moran. Estimating structural and functional relationships. *J Multivar Anal*, 1:232–255, 1971.
- S. Motupally, A. J. Becker, and J. W. Weidner. Diffusion of water in nafion 115 membranes. *J Electrochem Soc*, 147:3171–3177, 2000.
- P. P. Mukherjee and C. Y. Wang. Stochastic microstructure reconstruction and direct numerical simulation of the pefc catalyst layer. *J. Electrochem. Soc.*, 153:A840–A849, 2006.
- P. P. Mukherjee and C. Y. Wang. Direct numerical simulation modeling of bi-layer cathode catalyst layers in polymer electrolyte fuel cells. *J. Electrochem. Soc.*, 154:B1121–B1131, 2007.
- H. Nam and M. Kaviany. Effective diffusivity and water-saturation distribution in single- and two-layer pemfc diffusion medium. *Int J Heat Mass Tran*, 46:4595–4611, 2003.
- T. V. Nguyen and R. E. White. A water and heat management model for proton-exchange-membrane fuel cells. *J Electrochem Soc*, 140:2178–2186, 1993.
- C. C. Pantelides. Process modeling technology: A critical review of recent developments. *Proc FOCAPD*, pages 69–82, 2004.

- S. V. Patankar. *Numerical Heat Transfer And Fluid Flow*. New York, NY: Hemisphere publishing corporation, 1980.
- R. M. Rao and R. Rengaswamy. Optimization study of an agglomerate model for platinum reduction and performance in pem fuel cell cathode. *Chem Eng Res Des.*, 84:952–964, 2006.
- M. Secanell, K. Karan, A. Suleman, and N. Djilali. Multi-variable optimization of pemfc cathodes using an agglomerate model. *Electrochim Acta.*, 52:6318–6337, 2007.
- D. Song, Q. Wang, Z. Liu, M. Eikerling, Z. Xie, T. Navessin, and S. Holdcroft. A method for optimizing distributions of nafion and pt in cathode catalyst layers of pem fuel cells. *Electrochim. Acta*, 50:3359, 2005.
- T. E. Springer, T. A. Zawodzinski, and S. Gottesfeld. Polymer electrolyte membrane fuel cell model. *J Electrochem Soc*, 136:2334–2342, 1991.
- G. E. Soares and K. A. Hoo. Parameter estimation of a proton-exchange membrane fuel cell using voltage-current data. *Chem Eng Sci*, 55:2237–2247, 2000.
- W. Sun, B. A. Peppley, and K. Karan. An improved two-dimensional agglomerate cathode model to study the influence of catalyst layer structural parameters. *Electrochimica Acta*, 50:3359–3374, 2005.
- G. Suresh, A. K. Pandey, and A. Goswami. Self-diffusion coefficients of water

- in nafion-117 membrane with multivalent counterions. *J Memb Sci*, 284:193–197, 2006.
- E. A. Ticianelli, C. R. Derouin, and S. Srinivasan. Localization of platinum in low catalyst loading electrodes to attain high power densities in spe fuel cell. *J Electroanal Chem*, 251:275–295, 1988.
- S. Um and C. Y. Wang. Computational study of water transport in proton exchange membrane fuel cells. *J Power Sources*, 156:211–223, 2006.
- S. Um and C.Y. Wang. Three-dimensional analysis of transport and electrochemical reactions in polymer electrolyte fuel cells. *J Power Sources*, 125:40–51, 2004.
- S. Um, C. Y. Wang, and K. S. Chen. Computational fluid dynamics modeling of proton exchange membrane fuel cells. *J Electrochem Soc*, 147:4485–4493, 2000.
- A. Wächter and L. T. Biegler. On the implementation of an interior-point filter line-search algorithm for large-scale nonlinear programming. *Math Program*, 106:25–57, 2006.
- S. Walbran and A. A. Kornyshev. Proton transport in polarizable water. *Journal of Chemical Physics*, 114:10039–10048, 2001.
- C. Y. Wang. Fundamental models for fuel cell engineering. *Chem Rev*, 104:4727–4766, 2004.

- G. Wang, P. P. Mukherjee, and C. Y. Wang. Direct numerical simulation (dns) modeling of pefc electrodes: Part i. regular microstructure. *Electrochimica Acta*, 51:3139–3150, 2006a.
- G. Wang, P. P. Mukherjee, and C. Y. Wang. Direct numerical simulation (dns) modeling of pefc electrodes: Part ii. random microstructure. *Electrochimica Acta*, 51:3151–3160, 2006b.
- G. Wang, P. P. Mukherjee, and C. Y. Wang. Optimization of polymer electrolyte fuel cell cathode catalyst layers via direct numerical simulation modeling. *Electrochimica Acta*, 52:6367–6377, 2007a.
- J. Wang, J. K. Carson, M. F. North, and D. J. Cleland. A new approach to modelling the effective thermal conductivity of heterogeneous materials. *International Journal of Heat and Mass Transfer*, 49:3075–3083, 2006c.
- M. Wang, J. Wang, N. Pan, and S. Chen. Mesoscopic predictions of the effective thermal conductivity for microscale random porous media. *PHYS. REV. E*, 75:036702, 2007b.
- Y. Wang and C. Y. Wang. A nonisothermal, two-phase model for polymer electrolyte fuel cells. *J Electrochem Soc*, 153:A1193–A1200, 2006.
- Z. H. Wang, C. Y. Wang, and K. S. Chen. Two-phase flow and transport in the air cathode of proton exchange membrane fuel cells. *J Power Sources*, 94:40–50, 2001.

C. R. Wilke. A viscosity equation for gas mixtures. *J Chem Phys*, 18:517–519, 1950.

J. S. Yi and T. V. Nguyen. An along-the-channel model for proton exchange membrane fuel cells. *J Electrochem Soc*, 145:1149–1159, 1998.

L. You and H. Liu. A two-phase flow and transport model for the cathode of pem fuel cells. *Int J Heat Mass Tran*, 45:2277–2287, 2002.